Master of Science Thesis

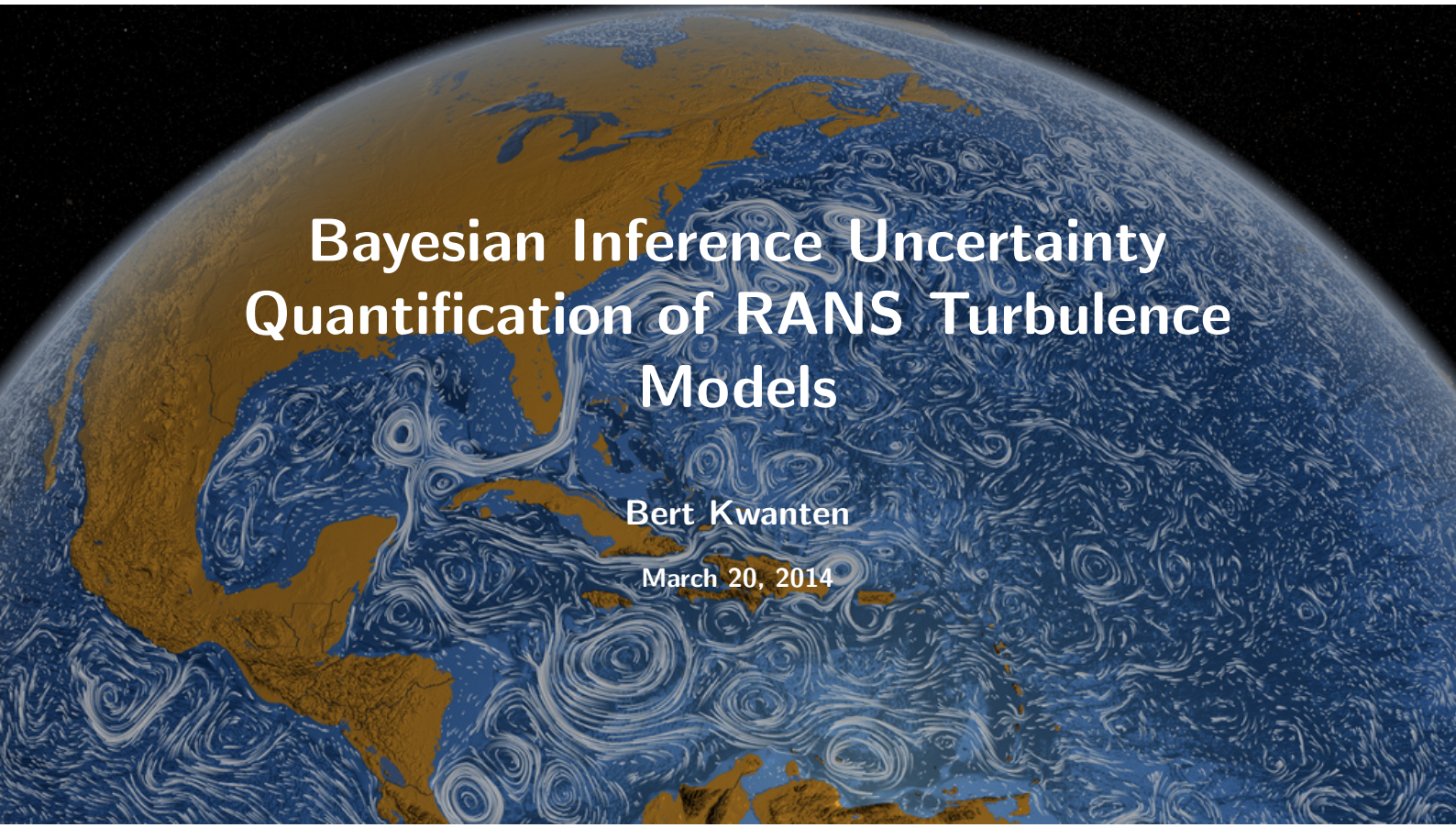

Bayesian Inference Uncertainty Quantification of RANS Turbulence Models

Bert Kwanten

March 20, 2014

Aerodynamics

Faculty of Aerospace Engineering

TU Delft

Delft University of Technology

Bayesian Inference Uncertainty Quantification of RANS Turbulence Models

Master of Science Thesis

For obtaining the degree of Master of Science in Aerospace Engineering
at Delft University of Technology

Bert Kwanten

March 20, 2014

Faculty of Aerospace Engineering · Delft University of Technology

Delft University of Technology

DELFT UNIVERSITY OF TECHNOLOGY
DEPARTMENT OF AERODYNAMICS

The undersigned hereby certify that they have read and recommend to the Faculty of Aerospace Engineering for acceptance the thesis entitled **"Bayesian Inference Uncertainty Quantification of RANS Turbulence Models"** by **Bert Kwanten** in fulfillment of the requirements for the degree of **Master of Science**.

Dated: March 20, 2014

Supervisors: _____

Preface

Except for thanking all people involved in the successful delivery of this thesis and obtaining my master of science degree in aerospace engineering, I would like to use this chapter to put down an idea related to the topic of this thesis.

I am currently working at IBM. A company which recently started up a new business unit around the Watson supercomputer. Watson is an artificially intelligent computer system capable of answering questions posed in natural language. In 2011, Watson competed on Jeopardy! against former winners Brad Rutter and Ken Jennings, and won! Watson had access to 200 million pages of structured and unstructured content consuming four terabytes of disk storage including the full text of Wikipedia, but was not connected to the Internet during the game. For each clue, Watson's three most probable responses were displayed on the television screen. An interesting fact about Watson is that at its core lies the same statistical technique as used in this thesis, i.e. Bayesian inference.

In this thesis, three RANS turbulence models and three flow cases have been investigated for which the experimental data was available. There are many more turbulence models available though, and the number of flow cases one can think of are basically infinite. Although there is no experimental data available for all of these, there is of course plenty more experimental data spread across the world.

Now imagine that, similar to what IBM is doing with Watson, one could gather all this experimental data and these available models from research institutions around the world. Consequently, a supercomputer could use all this information intelligently and come up with the most probable answer. It is a certainty that this approach would yield more accurate results than a single model currently in use can provide. While I admit it is a daunting task ☺, one might ask what is more probable in the near term: finding the solution of the Navier-Stokes equations or what I've just proposed.

I would like to say thank you to whoever is part or has been part of the great institutions where I received my higher education. Starting with Delft University of Technology, and more specifically the Aerospace engineering faculty, who's great teachers, facilities and network have brought me opportunities I wouldn't have gotten at other places. In a similar fashion, I also want to thank İstanbul Teknik Üniversitesi, Télécom ParisTech, The University of Texas at Austin and École Nationale Supérieure des Arts et Métiers ParisTech. Thank you also to all

the great friends I have made along the road.

Next I would like to thank Ir. Gigi van Rhee MBA, managing director of Stratelligence, for providing me my first professional experience; Lorant Czaran, former head of office of United Nations Office for Outer Space Affairs, for providing me the opportunity to work in a great international environment; and LL.M. Stan Pieters, managing director of Spinfin, for being a great mentor when it comes to entrepreneurship.

I am also grateful for the half year I spent at De Kleine Consultant, a strategy consultancy run by students and supported by AT Kearney. It was a tremendous amount of fun, with nice people and a great spirit.

To my first full-time employer, IBM, my mentors Pierre Valentin, Philipp Hansmann and Jim Hulders: thank you for believing in me! Working parallel at IBM and on my thesis was a challenge, but I could always count on you.

A big thank you also goes to my thesis supervisors Prof. Paola Cinnella and Dr. Richard Dwight for their constructive support, and for the interactions with Ir. Wouter Edeling and the other PhD. students who provided me useful insights into the thesis' topic.

Then the famous last but definitely not least... Thank you to my family. Thank you for your unconditional love, even when I was often far away from home.

Moeke, papa, ik had geen betere ouders kunnen wensen. Dichtbij of ver weg, weet dat ik altijd aan jullie denk. Zonder jullie was ik niets.

Bert Kwanten
Leuven, Belgium
March 9, 2014

Summary

Scientists and engineers use observations, mathematical and computational models to predict the behaviour of physical realities such as turbulent flows. However, as a consequence of observational errors, errors in the mathematical models and discretisation errors in the computational models, our knowledge about what happens in reality is imperfect.

The main purpose of the thesis is to investigate whether it is possible to quantify and to reduce the uncertainty of Reynolds-averaged Navier-Stokes (RANS) models - more specifically the Spalart-Allmaras, Smith's KL and the Launder-Sharma RANS turbulence models - using the Bayesian inference theorem. An underlying objective is to do determine the prior uncertainty by means of the analyst's knowledge of the used model, instead of merely guessing it, and the development of a methodical way to create and verify the correctness of a surrogate model for the RANS models.

Inherent to using RANS models is the closure problem resulting from applying the Reynolds-averaging technique to the Navier-Stokes equations. The model equations that are created (e.g. SA, KL and LS model) to mitigate the closure problem contain coefficients who's values are determined from calibration with experimental values. It is for some of these so-called closure coefficients that a prior uncertainty interval is determined.

A detailed study is performed on the prior uncertainty intervals for the closure coefficients. Some of the models' closure coefficients can be related to each other, effectively reducing the number of uncertainty parameters. For each model, we finally consider five uncertain parameters. In order to produce a reliable uncertainty interval for these closure coefficients, it is important to know the model inside out. The better knowledge you have about the model, the more reliable your prior uncertainty interval will be. In this thesis, the intervals have been determined by studying how the models are build up, and by comparing the values of the closure coefficients from different sources in literature.

Note that for each model, there are some coefficients they have in common. For example, the Von Kármán coefficient κ is present in each model, and coefficient C_μ occurs in both the KL and LS model. We have kept the interval the same for each of these coefficients across the three models. It is arguable that this is not necessarily the best approach as they don't directly correspond with a physical quantity. Therefore, as is concluded from the Bayesian calibration, their values can be different for each model.

The prior uncertainty interval that is determined for the uncertainty parameters needs to be propagated through the models in order to be able to apply Bayesian calibration. To enable this, surrogate models of the actual RANS turbulence models are created. We are able to create surrogate models for all RANS models and every use case.

Overall it can be concluded that there is room for improvement when creating these surrogate models. The sometimes large errors when compared to the actual simulation results should be eliminated as much as possible. It is not completely clear whether these large errors are the result of a combination of values for the uncertainty parameters that turn the model unstable. However, as these errors usually occur at the boundaries of the envelope, this is expected to be the main cause. In retrospect, when determining the interval of the prior uncertainty coefficients, it would be good to look at which combinations of closure coefficients yield a model for which convergence can be obtained. This would probably eliminate the large error at the boundaries of the surrogates.

After Bayesian calibration of the models, we observe that the prior uncertainty is significantly reduced. Hence, our thesis has been proven. Note that the best results are obtained at places where the density of the experimental data is highest. In addition, when the experimental uncertainty is lower, this also improves the uncertainty of the Bayesian calibrated simulation results. It is therefore very important to be in the possession of good experimental data in order to apply the technique successfully.

The Bayesian calibrated results also prove to be much more accurate than the deterministic results obtained using the default closure coefficients. The variance between the different model's results has also reduced.

Finally, when comparing the Bayesian calibrated closure coefficients for the different scenarios, we can conclude that they are both flow case as well as model dependent. Choosing a constant value for these parameters, as is regular practice when using RANS simulations, is therefore a rather inadequate approach.

Table of Contents

List of Figures

List of Tables

Chapter 1

Introduction

This chapter introduces the concept of uncertainty in predictive science. The first section will explain the so-called imperfect path to knowledge that scientists and engineers use to make predictions of the physical reality surrounding us. It also describes the different kind of uncertainties, i.e. epistemic and aleatoric uncertainty. Consequently, the second section describes the thesis's objective. Finally, the last section outlines the structure of this document.

1.1 Sources of Uncertainty in Predictive Science

Scientists and engineers use observations, mathematical and computational models to predict the behaviour of physical realities such as turbulent flows. However, as a consequence of observational errors, errors in the mathematical models and discretisation errors in the computational models, our knowledge about what happens in reality is imperfect. Figure 1.1 shows a schematic representation of this 'imperfect path to knowledge' as it was defined by Oden et al. [18].

The errors as depicted in Figure 1.1 are inherently present in any scientific prediction. Therefore, in order to make valuable predictions, these errors are managed by means of the *process of predictive science*, through which the errors are identified, quantified and, if possible, reduced. This process consists of four stages, and can be summarized as follows:

1. **Identifying Quantities of Interest:** It is of utmost importance to define the quantities of interest (QoI) in advance. A particular model might be perfectly capable of simulating certain features of a phenomenon, while totally incapable of modelling others.

2. **Verification:** Verification is the process of detecting and controlling the errors caused by the corruption of mathematical models through discretisation and errors arising from the implementation of the model in software (bugs).

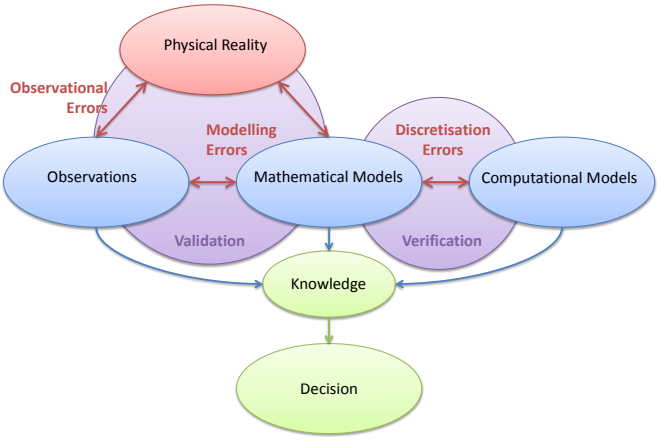

Figure 1.1: The imperfect path to knowledge

3. **Calibration:** Mathematical models usually contain adjustable parameters. The process of tuning these parameters in such a way that predictions and experimental observations come into closer agreement is called calibrating.

4. **Validation:** The validation process consists of carrying out carefully designed experiments in order to assess the legitimacy of the theoretical models in making predictions about the quantities of interest.

However, even when the process of predictive science is carefully applied, it is impossible to be completely certain that there are no errors present in a computational model. Therefore, next to errors, uncertainty is something which has to be dealt with. One kind of uncertainty is related to lack of knowledge, or so-called epistemic uncertainty [4][11][17][18].

> Epistemic uncertainty:
> A **potential** deficiency in any phase or activity of the modelling process that is **due to a lack of knowledge.**

This kind of uncertainty usually originates from imperfections in the mathematical models, or lack of knowledge about physical model parameters. In principal this uncertainty can be reduced when knowledge about physical reality increases. Therefore, epistemic uncertainty is said to be characteristic of the analyst, as it depends on the analyst's knowledge [11].

Imagine the hypothetical event in which there are no errors, nor epistemic uncertainties present in the computational model. In that case, the computational model would still have to cope with another kind of uncertainty. This kind of uncertainty is irreducible, and is related to the natural variability which is present in all physical realities. An example of natural variability is the uncertainty about initial and boundary conditions, e.g. the geometric description of a model. In literature this is referred to as aleatoric uncertainty [4][11][17][18].

Aleatoric uncertainty:
The **physical variation** present in the system being analysed or its environment.

Note however that the distinction between epistemic and aleatoric uncertainty is susceptible to interpretation and dependent on context. An example used by Oden et al. [18] is the throwing of a dice. In the context of a game, the outcome of throwing a dice is considered to be random and therefore the uncertainty about the outcome is called aleatoric (alea is actually Latin for dice). However, one could argue that it is possible to model the physical process behind throwing a dice, which would make the outcome deterministic. Therefore, the only uncertainty related to the outcome of throwing a dice would be epistemic, i.e. stemming from a lack of knowledge of the analyst.

This thesis focuses on reducing uncertainty by means of using Bayesian inference. From the definitions given above, it can be concluded that the part of the uncertainty which we are able to reduce is definitely of epistemic nature. However, whether the uncertainty which remains after applying Bayesian inference is epistemic or aleatoric is unknown.

1.2 Thesis Objectives

The main purpose of the thesis is to investigate whether it is possible to quantify and to reduce the uncertainty of RANS models using the Bayesian inference theorem. More specifically, we will investigate the Spalart-Allmaras, KL and Launder-Sharma RANS turbulence models.

An underlying objective is to do determine the prior uncertainty by means of the analyst's knowledge of the used model - instead of merely guessing, and the development of a methodical way of creating and verifying the correctness of a surrogate model for the investigated RANS models.

1.3 Thesis Outline

Chapter 2 introduces the mathematical framework we will use to calibrate uncertain parameters of the Reynolds-Averaged Navier-Stokes (RANS) Spalart-Allmaras (SA), KL and Launder-Sharma (LS) turbulence models. The framework consists of three parts, i.e. the Bayesian inference theorem, the probabilistic collocation method and the Markov Chain Monte Carlo method. First, we dive into the application of the Bayesian inference technique to the calibration of uncertain model parameters, as it is the backbone of the entire framework. Applying the Bayesian calibration technique to turbulence models is computationally expensive, because the stochastic nature of Bayesian calibration requires running the turbulence models several times over for different input parameters. Therefore, we make use of what one could call an efficient interpolation technique, i.e. the probabilistic collocation method. This method is introduced in Section 2.2, along with an application to the 1D Viscous Burgers Equation. Finally, Section 2.3 explains the Markov Chain Monte Carlo method,

which is used to obtain the posterior samples that finally result into the posterior (calibrated) distributions of the uncertain parameters.

The first step in the application of the Bayesian inference technique to the calibration of uncertain RANS model parameters, is to define an initial (prior) uncertainty interval for these parameters. Chapter 3 starts by explaining how the RANS equations are confronted with a so-called closure problem, resulting in the necessity of models containing closure coefficients who's values are uncertain. This is followed by an extensive discussion on the determination of prior uncertainty intervals for each of the considered model's uncertain parameters.

To be able to compare the uncertainty of the Spalart-Allmaras, Launder-Sharma's $k-\epsilon$ and Smith's $k-l$ turbulence model, we need to apply them to a couple of test cases. For this purpose, three turbulent flat plate flows have been selected. The main difference between them is that each are subject to a different pressure gradient, i.e.

- Wieghardt's zero pressure gradient case (zpg) [16];
- Ludwieg and Tillman's favourable pressure gradient case (fpg) [15];
- and Ludwieg and Tillman's adverse pressure gradient case (apg) [15].

These three test cases are discussed in Chapter 4.

The next step is to propagate the uncertain parameters that are determined in Chapter 3 through the SA, KL and LS model for the three different test cases. In order to do that, we use the probabilistic collocation method to create surrogate models. The creation of a total of nine (3 models $\times$ 3 test cases) is covered in Chapter 5.

Finally, Chapter 6 discusses the results of the Bayesian calibration for the SA and KL model. Unfortunately the Bayesian calibration for the Launder-Sharma model did not work. Why that is the case is unclear, as the process that was followed was exactly the same as for the two other models.

Chapter 2

Theory and Problem Definition

This thesis aims to investigate the reduction of the epistemic uncertainty, which was introduced in Chapter 1. The mathematical framework we will use consists of three parts, i.e. the Bayesian inference theorem, the probabilistic collocation method and the Markov Chain Monte Carlo method. First, we dive into the application of the Bayesian inference technique to the calibration of uncertain model parameters, as it is the backbone of the entire framework. Applying the Bayesian calibration technique to turbulence models is computationally expensive, because the stochastic nature of Bayesian calibration requires running the turbulence models several times over for different input parameters. Therefore, we make use of what one could call an efficient interpolation technique, i.e. the probabilistic collocation method. This method is introduced in Section 2.2, along with an application to the 1D Viscous Burgers Equation. Finally, Section 2.3 explains the Markov Chain Monte Carlo method, which is used to obtain the posterior samples that finally result into the posterior (calibrated) distributions of the uncertain parameters.

2.1 Theory of Bayesian Calibration

2.1.1 Computational and Experimental Uncertainty

The sources of uncertainty in any scientific prediction are introduced in Chapter 1, and modelled into the so-called *Imperfect path to knowledge*. It includes uncertainty resulting from faulty experimental observations and erroneous computational models. This section will describe these sources of uncertainty in more detail.

In the paper of Cheung et al. [2], the process of collecting data is defined by Figure 2.1. From this figure, it can be observed where the uncertainties within experimental observations originate from. A first error source is the experimental apparatus itself. Due to conversions in the experimental apparatus, the measured values $\boldsymbol{d}$ are not necessarily the same as the

actual values of the observables $\boldsymbol{d_{actual}}$. Another source of uncertainty are the conditions at which the experiment is executed. During an experiment, the input parameters $\boldsymbol{\theta}$ governing the investigated phenomenon are set to certain values given on a display of some sort. Unfortunately, it is impossible to know whether the input parameters are set to the exact value as given on the display. Most likely, they are not. Therefore, the exact value of the input parameters $\boldsymbol{\theta_{actual}}$ is unknown. In addition, it is sometimes even unknown what all the input parameters governing the observed phenomenon are. A second source of uncertainty is

Figure 2.1: The process of collecting data as defined by Cheung et al. [2]

the used computational model. A computational model uses algorithms to solve a discretised form of a mathematical model. In general, it consists of two parts:

- A vector θ of n parameters, which can be anything ranging from material properties, coefficients, constitutive parameters, boundary conditions, initial conditions, etc.;
- A set of governing equations $\mathbf{r}(\theta, \mathbf{u}(\theta)) = \mathbf{0}$, in which the solution $\mathbf{u}(\theta)$ represents the state variables or model state.

Next to these state equations, the computational model also includes functions which calculate model output data $\mathbf{y}(\theta, \mathbf{u})$, and predicts a vector of m quantities of interest $\mathbf{q}(\theta, \mathbf{u})$. The important distinction between $\mathbf{y}$ and $\mathbf{q}$ is that the former can be compared with experimental data during the calibration of the model, while the latter can not as these are predictions of a (currently) unmeasurable quantity. A schematic representation of a computational model is given by Figure 2.2. Finally, it should be noted that computational models can be either

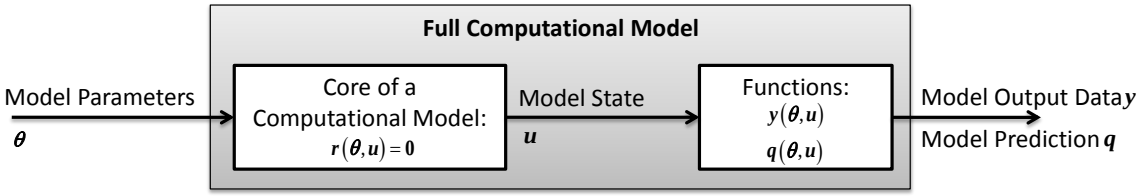

Figure 2.2: The representation of a computer model as defined by Cheung et al. [2].

deterministic or stochastic. Our interest goes out to the stochastic kind in which at least one of the parameters has been assigned a probability density function, representing its uncertainty.

2.1.2 Inverse Problems and the Bayesian Formula

A computational model can be used to solve two kinds of problems, i.e. forward and inverse. In the case of a forward problem the parameters θ are given and the state variables $\mathbf{u}$, model output data $\mathbf{y}$ and prediction/quantity of interest $\mathbf{q}$ need to be calculated. An inverse problem on the other hand, estimates the values of the parameters θ in such a way that the model's output data $\mathbf{y}$ fits the experimental data $\mathbf{d}$ as accurately as required/possible. This process is also called model calibration, and usually precedes the computation of quantities of interest $\mathbf{q}$. Both the inverse and forward problem are represented in Figure 2.3. In the previous section,

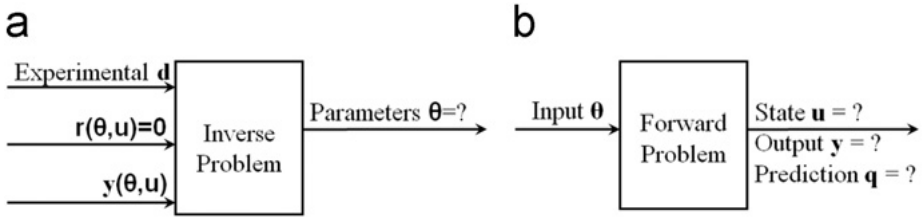

Figure 2.3: (a)generic inverse problem (b)generic forward problem [2].

a final note was made stating that we are interested in stochastic computer models. The stochastic representation of a forward problem is similar to the deterministic case. However, for the inverse problem, the Bayesian approach needs to be adopted. The solution of the statistical inverse problem is the posterior probability density function, given as

$$p_{posterior}(\theta|\mathbf{d}) = \frac{p_{likelihood}(\mathbf{d}|\mathbf{y},\mathbf{r},\theta)p_{prior}(\theta)}{p(\mathbf{d})}, \tag{2.1}$$

in which p_{prior} is the prior information about the parameters, these can be obtained from literature, experiments or previous simulations, among others. The likelihood $p_{likelihood}(\mathbf{d}|\mathbf{y},\mathbf{r},\theta)$ is the probability of observing the data $\mathbf{d}$, given the model and parameters θ. The information on the data $p_{\mathbf{d}}$ is only used to normalize the solution and sometimes omitted. The Bayesian formula is one of the fundamental concepts used in quantifying uncertainty. A schematic representation of a statistical inverse and forward problem is given by Figure 2.4.

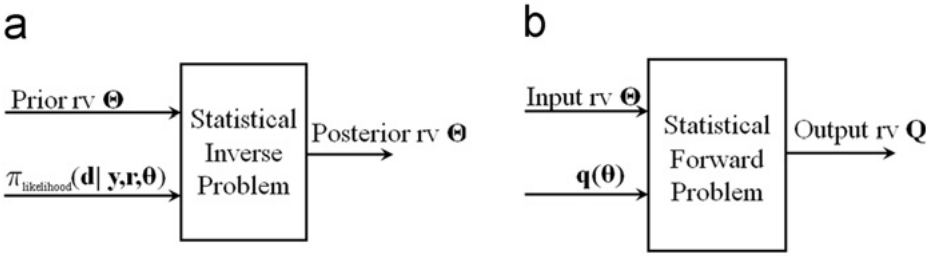

Figure 2.4: (a)statistical inverse problem (b)statistical forward problem [2].

2.1.3 Stochastic Model Classes

In the Bayesian framework, a key concept is that of a stochastic system model class, consisting of a chosen set of probabilistic input-output models for a system and a chosen prior probability density function. A probabilistic input-output model is created by incorporating stochastic models into the considered simulation model. Mathematically it can be described as follows:

$$\begin{aligned}&\mathbf{r}(\theta, \mathbf{u}, \xi) = \mathbf{0},\\ &\mathbf{y} = \mathbf{y}(\theta, \mathbf{u}, \epsilon),\\ &\mathbf{d} = \mathbf{d}(\theta, \mathbf{d}_{actual}, \zeta),\end{aligned} \tag{2.2}$$

in which the model state $\mathbf{u}$ is the solution of the stochastic equation $\mathbf{r}(\theta, \mathbf{u}, \xi) = \mathbf{0}$; $\mathbf{y}$ is the stochastic model output; $\mathbf{d}$ is a random vector or random field obtained from the measured/observed data D; and $\mathbf{d}_{actual}$, which is some subset of $\mathbf{y}$, is the actual quantity corresponding to $\mathbf{d}$. The additional variables ξ, ϵ and ζ are random vectors or random fields with a joint probability density function $p(\xi, \epsilon, \zeta|\theta_s, M_j)$, in which θ_s is a subset of the uncertain parameter vector θ of the stochastic system model class M_j. The prior probability density function represents the initial relative plausibility of each model based on expert knowledge or other sources such as literature and previous experiments, etc.

To make the Bayesian formula explicitly dependent on the model class M_j, it can be rewritten as follows:

$$p(\theta|D, M_j) = \frac{p(D|\theta, M_j)p(\theta|M_j)}{p(D|M_j)} = \frac{p(D|\theta, M_j)p(\theta|M_j)}{\int p(D|\theta, M_j)p(\theta|M_j)d\theta}, \tag{2.3}$$

in which the model class M_j is dependent on the parameters $\theta_j \in \Theta \subset \mathbb{R}^n$. The denominator of equation (2.3) is called the evidence for M_j given D[1]. More specifically, it expresses the probability of measuring/observing the data D for a model M_j; $p(\theta|M_j)$ is the prior probability density function of the model θ within M_j; and $p(D|\theta, M_j)$ is the likelihood function, expressing the probability of observing D given the predictive model θ within M_j:

$$p(D|\theta, M_j) = \int p(D|\mathbf{w}, \theta, M_j)p(\mathbf{w}|\theta, M_j)d\mathbf{w}, \tag{2.4}$$

in which $\mathbf{w}$ represents all the unobserved model outputs, model states, modelling and measurement errors, boundary conditions and initial conditions[2]. The probability density function $p(D|\mathbf{w}, \theta, M_j)$ is given by

$$p(D|\mathbf{w}, \theta, M_j) = \int p(D|\tilde{\mathbf{d}}, \mathbf{w}, \theta, M_j)p(\tilde{\mathbf{d}}|\mathbf{w}, \theta, M_j)\, d\tilde{\mathbf{d}}, \tag{2.5}$$

where $\tilde{\mathbf{d}}$ are the exact values of the measured quantities.

Now that the Bayesian formula (2.1) is rewritten into its explicit form (2.3), consider the set of candidate competing model classes $M = \{M_1, M_2, ..., M_{N_M}\}$. Each model within this set is different from each other because of parametric, structural or other uncertainties. Now, for each of these models, the posterior probability density function, evidence, relative plausibility

and predictions can be determined. The relative plausibility is defined by the posterior probability $P(M_j|D, M)$, which can be found by applying Bayes' theorem to the prior probability $P(M_j|M)$:

$$P(M_j|D, M) = \frac{p(D|M_j)P(M_j|M)}{\sum_{k=1}^{N_M} p(D|M_k)P(M_k|M)} \tag{2.6}$$

Without a priori information, $P(M_j|M)$ is often taken as uniform. The evidence of each model class determines the corresponding posterior probability, and can be found using the Theorem of Total Probability [1]:

$$p(D|M_j) = \int p(D|\theta, M_j)p(\theta|M_j)d\theta, \tag{2.7}$$

as was already indicated in equation (2.3). The posterior predictive probability distribution of the unobservable quantities of interest $\mathbf{q}$ for model class M_j is given by

$$p(\mathbf{q}|D, M_j) = \int p(\mathbf{q}|\theta, D, M_j)p(\theta|D, M_j)d\theta, \tag{2.8}$$

where the predictive probability density function of each model M_j is weighted by its posterior probability. Next to an individual prediction for each model class, also an overall prediction can be obtained based on the prediction of all model classes described as

$$p(\mathbf{q}|D, M) = \sum_{j=1}^{N_M} p(\mathbf{q}|D, M_j)P(M_j|D, M), \tag{2.9}$$

in which the robust posterior predictive probability density function for each model class M_j is weighted by its posterior probability $P(M_j|D, M)$. It is important to note that multi-dimensional integrals, such as (2.8) cannot be evaluated analytically. Hence, methods are developed to provide the samples $\theta^{(k)}$, which are needed to approximate the posterior probability density function $p(\theta|D, M_j)$ by means of the following equation:

$$p(\mathbf{q}|D, M_j) \approx \frac{1}{K} \sum_{k=1}^{K} p(\mathbf{q}|\theta^k, D, M_j) \tag{2.10}$$

The sampling method used in this thesis is the Probabilistic Collocation Method, which is described in Section 2.2.

Experimental Uncertainty

A probabilistic model of the observation process, which is shown in Figure 2.1, is mathematically represented by

$$d_i = \tilde{d}_i + e_i, \tag{2.11}$$

in which d_i and e_i are the i-th components of random vectors $\mathbf{d} \in \mathbb{R}^N$ and $\mathbf{e} \in \mathbb{R}^N$ respectively. The quantities in vector $\tilde{\mathbf{d}}$ represent the true values corresponding to the quantities in vector $\mathbf{d}$, while the components of vector $\mathbf{e}$ are independent, Gaussian random variables, with mean

zero and prescribed standard deviations: $\sim \mathcal{N}(0, \lambda_i)$. In the example of Cheung et al.[2], standard deviations are set to 2% and 5% of the observed value for the velocity and shear stress measurements respectively.

Given the previous assumptions, the probability density function $p(\mathbf{d}|\tilde{\mathbf{d}}, M_j)$ can be written as

$$p(\mathbf{d}|\tilde{\mathbf{d}}, M_j) = \frac{1}{\sqrt{(2\pi)^N \det K_e}} \exp\left[-\frac{1}{2}(\mathbf{d}-\tilde{\mathbf{d}})^T K_e^{-1}(\mathbf{d}-\tilde{\mathbf{d}})\right], \tag{2.12}$$

in which K_e is a diagonal matrix with the i-th diagonal entry equal to the variance of e_i.

Model Inadequacy

Next to uncertainty in the experimental data, we also have to deal with uncertainties related to the computational model. As there are many stochastic models which can be used to deal with this model inadequacy, a set of candidate model classes is defined. The model classes are constructed based on stochastic equation

$$\tilde{d}_i = \eta_i y_i(\theta_p), \tag{2.13}$$

in which $y(\theta_p)$ denotes the model output quantities from the RANS-SA model corresponding to the quantities in $\tilde{\mathbf{d}}$; and η_i is the i-th component of a random vector $\boldsymbol{\eta}$ which corrects for the mismatch between $y(\theta_p)$ and $\tilde{\mathbf{d}}$. The multiplicative form is chosen such that the no-slip boundary condition is satisfied, i.e. $u = 0$ at the wall. Once the probability density function for $\boldsymbol{\eta}$ is known, (2.13) is completely defined.

Cheung et al.[2] consider three model classes which are only different in the way they model $\boldsymbol{\eta}$:

1. **No Uncertainty:** $\boldsymbol{\eta} = \mathbf{1}$, in which $\mathbf{1}$ is a vector of ones;
2. **Independent Gaussian uncertainty:** $\eta_i \sim \mathcal{N}(1, \sigma^2)$ for $i = 1, ..., N$, in which σ is an additional uncertain parameter and $p(\tilde{\mathbf{d}}|\theta) \sim \mathcal{N}(\mathbf{y}(\theta_p), K_{mi})$;
3. **Correlated Gaussian uncertainty:** $\boldsymbol{\eta} \sim \mathcal{N}(\mathbf{1}, K_{mc})$, in which $\mathbf{1}$ is the mean vector and K_m the covariance matrix determined from a Gaussian random field model of the velocity field.

It is important to note that $\boldsymbol{\eta}$ may depend on additional uncertainty parameters θ_u, which are included in the total parameter vector $\theta^T = [\theta_p^T, \theta_u^T]$. The probability density function of $\tilde{\mathbf{d}}$ conditioned on θ^T, $p(\tilde{\mathbf{d}}|\theta)$, can now be computed.

The Calibration Problem

From equation (2.5) and the models found in the previous two subsections, the likelihood function $p(\hat{d}|\theta, M_j)$ is found to be a Gaussian probability density function given by (2.14):

$$p(\hat{d}|\theta, M_j) = \frac{1}{\sqrt{(2\pi)^N \det K}} \exp\left[-\frac{1}{2}(\hat{d}-\mathbf{y})^T K^{-1}(\hat{d}-\mathbf{y})\right], \tag{2.14}$$

in which $\hat{d}$ is the vector in which measured data D is stored. This vector can be interpreted as a realization of the random vector $\mathbf{d} \in \mathbb{R}^N$. Equation (2.14) is different for the three model classes, as the covariance matrix K is different for all three of them. More specifically:

1. M_1: $K = K_e$;
2. M_2: $K = K_e + K_{mi}$;
3. M_3: $K = K_e + K_{mc}$.

In this thesis, we only use the model class of the first kind.

2.2 The Probabilistic Collocation Method

Several techniques have been developed in order to run the uncertainty of input parameters through a simulation code. These methods usually require a number of deterministic computations of the code, which makes them computationally expensive. Therefore, continuous effort is made to find efficient propagation techniques, requiring an ever smaller number of deterministic solves. Furthermore, non-intrusive techniques are preferred, as they can be coupled to any commercial solver without having to adapt the solver itself. One such relative efficient and non-intrusive technique is the Probabilistic Collocation method developed by Loeven et al. [12]. This technique is based on the intrusive Galerkin Polynomial Chaos method [8][9][25], which is covered to some detail in Appendix A. In Section 2.2.1 the theory of the probabilistic collocation method is explained. Section 2.2.2 shows the application of the Probabilist Collocation method to the 1D viscous Burgers equation.

2.2.1 The Probabilistic Collocation Method Explained

In order to explain the Probabilistic Collocation method, we rewrite Equation (2.2) into a general stochastic differential equation:

$$\mathcal{L}\left(\mathbf{x}, t, \theta; u(\mathbf{x}, t, \theta)\right) = S\left(\mathbf{x}, t, \theta\right), \tag{2.15}$$

in which $\mathcal{L}$ is a differential operator, S a source term and u the solution depending on space, time and a random event θ. Similar to the Galerkin Polynomial Chaos method, also the Probabilistic Collocation method decomposes the solution u into a deterministic and a stochastic part,

$$u\left(\mathbf{x}, t, \theta\right) \approx \sum_{i=1}^{N_p} u_i(\mathbf{x}, t) L_i\left(\xi(\theta)\right) \tag{2.16}$$

in which the coefficients u_i are the deterministic solutions at the so-called collocation points θ_i, with L_i the corresponding Lagrange interpolating polynomial chaos. These polynomial

chaoses are a function of the random variable $\xi(\theta)$, whose standard parametric domain corresponds to $[-1, 1]$, $[0, \infty)$ or $(-\infty, \infty)$ depending on the chosen probability density function. Each ξ_i is determined in such a way that the uncertain parameters a become a linear function of $\xi(\theta)$:

$$a(\theta) = \frac{a(\theta_1)\xi(\theta_0) - a(\theta_0)\xi(\theta_1)}{\xi(\theta_0) - \xi(\theta_1)} + \frac{a(\theta_0) - a(\theta_1)}{\xi(\theta_0) - \ xi(\theta_1)}\xi(\theta) = \tilde{a}_0 + \tilde{a}_1\xi(\theta). \tag{2.17}$$

Finally, the Lagrange interpolating polynomial chaoses are polynomials of the order $N_P - 1$, which pass through the N_P collocation points. They are computed using

$$L_i(\xi(\theta)) = \prod_{\substack{j=1 \\ j \neq i}}^{N_P} \frac{\xi(\theta) - \xi(\theta_j)}{\xi(\theta_i) - \xi(\theta_j)}, \tag{2.18}$$

with $L_i(\xi(\theta)) = \delta_{ij}$, the Kronecker delta[1]. The N_P collocation points are specifically selected sample points, such that they correspond to the Gauss quadrature points used to integrate the solution $u(\mathbf{x}, t, \theta)$ in the θ-domain, which is necessary to obtain the mean and variance of the solution. The method used by Loeven et al. [13] to determine the Gaussian quadrature rules, is the Golub-Welsch algorithm [10]. This algorithm needs the recurrence coefficients of polynomials which are orthogonal to the weighting function of the integration as an input. In order to obtain the exponential convergence for arbitrary probability distributions, the polynomials have to be orthogonal with respect to the probability density function of ξ, hence $w(\xi) = f_\xi(\xi)$. When multiple uncertain parameters are considered, the process is done for each ξ_j, $j = 1, ..., d$ separately. The number of collocation points in that case become $N_P = (p + 1)^d$, for which p is the polynomial chaos' order and d is the number of uncertain parameters.

The orthogonal polynomials discussed, can be constructed using the three-term recurrence relation, i.e.

$$\begin{aligned} \Psi_{i+1}(\xi) &= (\xi - \alpha_i)\Psi_i(\xi) - \beta_i\Psi_{i-1} && i = 2, 3, ..., N_P, \\ \Psi_0(\xi) &= 0, \Psi_1(\xi) = 1, \end{aligned} \tag{2.19}$$

where α_i and β_i are the recurrence coefficients determined by the weighting function $w(\xi)$ and $\{\Psi_i(\xi)\}_{i=1}^{N_P}$ is a set of (monic) orthogonal polynomials with $\Psi_i(\xi) = \xi^i + \mathcal{O}(\xi^{i-1}), i = 1, 2, ..., N_P$. The recurrence coefficients are given by Darboux's formulae [7]:

$$\alpha_i = \frac{(\xi\Psi_i, \Psi_i)}{(\Psi_i, \Psi_i)} \qquad i = 1, 2, ..., N_P, \tag{2.20}$$

$$\beta_i = \frac{(\Psi_i, \Psi_i)}{(\Psi_{i-1}, \Psi_{i-1})} \qquad i = 1, 2, ..., N_P, \tag{2.21}$$

in which $(\cdot, \cdot)$ represents an inner product, which is defined by equation (A.6). The first coefficient β_1 is given by (Ψ_1, Ψ_1). The different recurrence coefficients are computed using

[1]The Kronecker delta is 1 if the variables are equal, and 0 otherwise: $\delta_{ij} = 0$ if $i \neq j$ and $\delta_{ij} = 1$ if $i = j$.

the discretised Stieltjes procedure [6]. This procedure discretises the weighting function $w(\xi)$ by

$$w_N(\xi) = \sum_{j=1}^{N} w_j \delta(\xi - \xi_j) \qquad w_j > 0, \tag{2.22}$$

where δ is the Dirac delta function. The Stieltjes procedure starts by calculating the coefficient α_1 and β_1 using equations 2.20 and 2.21. Consequently, $\Psi_2(\xi)$ is computed by the recurrence relation 2.19. This process is repeated for $i = 2, 3, ..., N_P$.

Once all the recurrence coefficients are known, the Golub-Welsch algorithm [10] can be used to compute the transformed collocation points ξ_i and corresponding weights w_i. The recurrence coefficients are used to construct a Jacobi matrix:

$$J = \begin{bmatrix} \alpha_1 & \sqrt{\beta_2} & & & & \\ \sqrt{\beta_2} & \alpha_2 & \sqrt{\beta_3} & & \emptyset & \\ & \sqrt{\beta_3} & \alpha_3 & \sqrt{\beta_4} & & \\ & & \ddots & \ddots & \ddots & \\ & \emptyset & & \sqrt{\beta_{N_P-1}} & \alpha_{N_P-1} & \sqrt{\beta_{N_P}} \\ & & & & \sqrt{\beta_{N_P}} & \alpha_{N_P} \end{bmatrix} \tag{2.23}$$

The coefficients ξ_i are the eigenvalues of J and the roots of the polynomial of order N_P. The weights are defined as

$$w_i(\xi) = \beta_1 v_{1,i}^2 \qquad i = 1, 2, ..., N_P, \tag{2.24}$$

where $v_{1,i}$ is the first component of the normalized eigenvector corresponding to the eigenvalue ξ_i. Now the transformed collocation points in the ξ-domain are known, the collocation points θ_i are found by

$$\theta_i = F_\xi(\xi_i) \qquad i = 1, 2, ..., N_P. \tag{2.25}$$

Finally, equation (2.16) can be substituted into (2.15) and the approximated Galerkin projection is applied on each polynomial $\{L_j(\xi(\theta))\}$:

$$\left\langle \mathcal{L}\left(\mathbf{x}, t, \theta; \sum_{i=1}^{N_P} u_i L_i\right), L_j \right\rangle = \langle S, L_j \rangle \qquad j = 1, 2, ..., N_P \tag{2.26}$$

This results in a fully decoupled deterministic system of equations. Finally, the mean and variance of the solution u are given by the following two equations:

$$\mu_u = \sum_{i=1}^{N_P} u_i(\mathbf{x}, t) w_i \tag{2.27}$$

$$\sigma_u^2 = \sum_{i=1}^{N_P} (u_i(\mathbf{x}, t))^2 w_i - \mu_u^2, \tag{2.28}$$

in which $u_i(\mathbf{x}, t)$ is the solution of collocation point θ_i, with w_i its corresponding weight. The next section will show the application of the polynomial collocation method to the 1D viscous Burgers equation.

2.2.2 Example: The 1D Viscous Burgers Equation

As an example, we study the 1D viscous Burgers equation for $x \in [-1, 1]$, $x \in \mathbb{R}$ and $t > 0$. The velocities at the boundaries are $u(x = -1) = 1$ and $u(x = 1) = -1$, also known as the Dirichlet boundary conditions.

$$\frac{\partial u}{\partial t} + u\frac{\partial u}{\partial x} = \nu\frac{\partial^2 u}{\partial^2 x} \tag{2.29}$$

The parameter which is considered uncertain is the viscosity coefficient ν. It is assumed that its value is Gaussian distributed with a mean $\mu_\nu = 0.15$ and a coefficient of variation $CV = 1.5\%$[2]. For this case, we will use the Gauss-Hermite chaos quadrature.

The probabilistic collocation method starts by obtaining the collocation points at which the deterministic solutions have to be obtained. These collocation points correspond to the quadrature points, which are equal to the roots of the Hermite polynomial θ_i[3]. Finally, the values of the viscosity can be calculated from the transformation $\xi(\theta) = \mu_\nu + \sqrt{2}\sigma_\nu\theta_i$. For a polynomial order of 5, we obtain 5 different values for the viscosity. The solutions of the 1D viscous Burgers equation for these 5 different values are plotted in Figure 2.5.

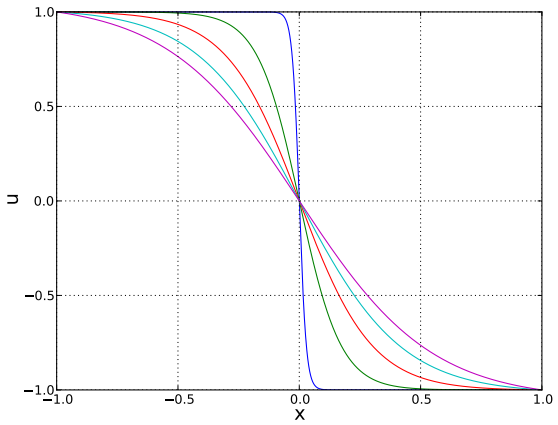

Figure 2.5: The deterministic solutions of the 1D viscous Burgers equation at the five quadrature points. The uncertain parameter is the viscosity ν, which is assumed to be Gaussian distributed with a mean $\mu_\nu = 0.15$ and a $CV = 1.5\%$.

From the deterministic solutions u_i and the obtained weights w_i, the mean and variance of the solution can be obtained using Equations (2.27) and (2.28). To illustrate the efficiency of the Probabilistic Collocation method, it is compared to a Monte Carlo method[4] using 2000 random samples of the proposed Gaussian distribution for the viscosity parameter ν. Note that the error between the two methods is relatively small.

[2] The coefficient of variation is calculated as the standard deviation of the random variable divided by its mean: $CV = \frac{\sigma}{\mu}$.

[3] For details about the Hermite polynomials, see Appendix B.

[4] For a detailed explanation of the Monte Carlo method, see Appendix C.

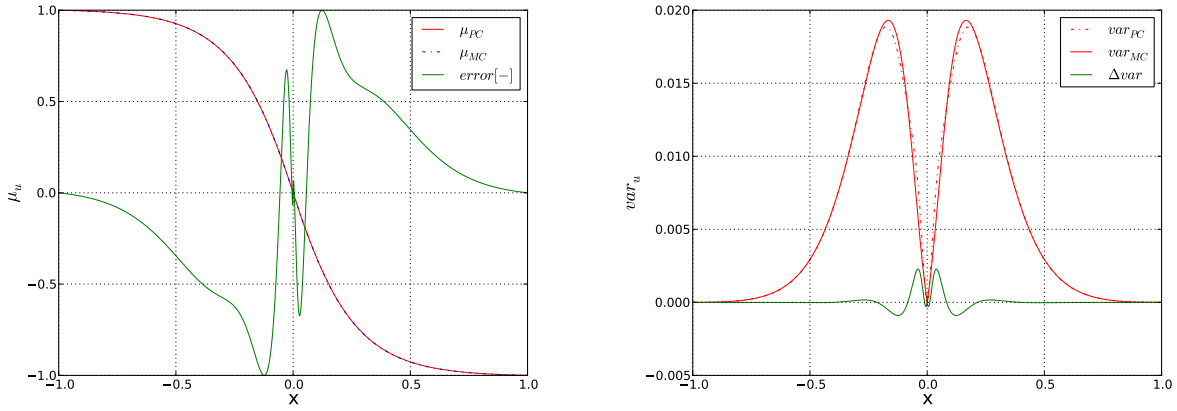

(a) A comparison of the mean solution.

(b) A comparison of the variance.

Figure 2.6: Comparison of the statistics obtained by the Probabilistic Collocation method (PC) and the Monte Carlo method (MC). In (a) the error is normalized by the maximum error in the domain, while in (b) the error $\Delta var = var_{PC} - var_{MC}$.

2.3 Markov Chain Monte Carlo for Posterior Sampling

The Markov chain Monte Carlo method (MCMC) is a more efficient adaptation of the basic Monte Carlo method, which is explained in Appendix C. More efficient in the sense that it needs less samples to reconstruct a particular probability density function, in our case of the posterior $P(\boldsymbol{\theta} \mid \boldsymbol{d})$. In addition to its enhanced efficiency, it is also an important property of the MCMC method to not need a normalisation factor $P(\boldsymbol{d})$, which is generally hard to obtain as was mentioned in Section 2.1.

The enhanced efficiency of the MCMC method as compared to the basic Monte Carlo method is the result of the application of a Markov chain. A Markov chain is a sequence of random variables x_{n+1}, x_n,..., x_0 with the Markov property, i.e. the next state is only dependent on the present state and not on any other state in the past:

$$p(X_{n+1} = x | X_1 = x_1, X_2 = x_2, ..., X_n = x_n) = p(X_{n+1} = x | X_n = x_n). \tag{2.30}$$

This means that, contrary to the basic Monte Carlo method, the MCMC method's samples are not entirely independent. The MCMC method which we apply to sample the posterior distribution is a random walk Monte Carlo method. This method is often implemented by the Metropolis-Hastings algorithm, which is also the preferred choice in our work.

Metropolis-Hastings

1. Randomly generate the initial parameter vector $\boldsymbol{\theta}_{t=0}$ using the prior distribution $P(\boldsymbol{\theta})$.

2. Generate a candidate vector $\boldsymbol{\theta}^{'}$ by adding a $\delta\boldsymbol{\theta}$, generated from a proposal distribution, to the current state $\boldsymbol{\theta}_t$, i.e. $\boldsymbol{\theta}^{'} = \boldsymbol{\theta}_t + \delta\boldsymbol{\theta}$.
3. Obtain the likelihood term for the current state $P(\boldsymbol{d} \mid \boldsymbol{y}, \boldsymbol{r}, \boldsymbol{\theta}_t)$ and candidate future state $P(\boldsymbol{d} \mid \boldsymbol{y}, \boldsymbol{r}, \boldsymbol{\theta}^{'})$, using Equation (2.14).
4. Using Bayes theorem (2.1), the posterior probability of the current state $P(\boldsymbol{\theta}_t \mid \boldsymbol{d})$ and candidate future state $P(\boldsymbol{\theta}^{'} \mid \boldsymbol{d})$ can now be computed.
5. Calculate the acceptance ratio $a = \min\left\{1, \frac{P(\boldsymbol{\theta}^{'}|\boldsymbol{d})}{P(\boldsymbol{\theta}_t|\boldsymbol{d})}\right\}$.
6. Pick a random value b from a uniform distribution with bounds 0 and 1, i.e. $\mathcal{U}(0, 1)$.
7. If $b \leq a$, the candidate vector is accepted and $\boldsymbol{\theta}_{t+1} = \boldsymbol{\theta}^{'}$. When a candidate vector is not accepted, we start again from the current state, i.e. $\boldsymbol{\theta}_{t+1} = \boldsymbol{\theta}^{t}$.
8. Repeat steps 2 to 7 until a sufficient number of samples is obtained to reconstruct the posterior probability density function.

As the Markov chain starts with a random initial parameter vector $\boldsymbol{\theta}_{t=0}$, it takes some iterations before it converges to the equilibrium solution. These first iterations are part of the so-called *burn-in* period, and are eliminated from the final samples which compose the probability density function of the posterior.

Chapter 3

Parametric Uncertainty of Reynolds-averaged Navier-Stokes Models

The first step in the application of the Bayesian inference technique to the calibration of uncertain RANS model parameters, is to define an initial (prior) uncertainty interval for these parameters. The chapter starts by explaining how the RANS equations are confronted with a so-called closure problem, resulting in the necessity of models containing closure coefficients who's values are uncertain. This is followed by an extensive discussion on the determination of prior uncertainty intervals for each of the considered model's uncertain parameters.

3.1 The Reynolds-averaged Navier-Stokes Models and the Closure Problem

A commonly used technique to determine the mean flow properties of a turbulent flow is the application of Reynolds-averaging to the Navier-Stokes equations. Assuming zero body forces, the Navier-Stokes equations as represented by Equation (3.1), (3.2) and (3.3) describe the motion of incompressible fluids by embodying the principles of conservation of mass, momentum and energy, respectively.

$$\frac{\partial u_i}{\partial x_i} = 0 \tag{3.1}$$

$$\frac{\partial u_i}{\partial t} + u_j \frac{\partial u_i}{\partial x_j} = -\frac{1}{\rho}\frac{\partial p}{\partial x_i} + \nu \frac{\partial^2 u_i}{\partial x_j^2} \tag{3.2}$$

$$\frac{\partial \theta}{\partial t} + u_j \frac{\partial \theta}{\partial x_j} = \kappa \frac{\partial^2 \theta}{\partial x_j^2} \tag{3.3}$$

Consequently, the Reynolds-averaged Navier-Stokes equations can be derived by using Reynolds decomposition, i.e. the instantaneous variables for velocity (u) and pressure (p), are split into a mean part and a fluctuating part i.e.

$$q = Q + q'. \tag{3.4}$$

The mean (Q) in this equation is described as an ensemble mean,

$$Q = \lim_{N\to\infty} \frac{1}{N} \sum_{\alpha=1}^{N} q^{(\alpha)} = \bar{q}, \tag{3.5}$$

which is obtained by averaging all realizations, q^{α}, of an experiment performed N times.

The Reynolds-averaged Navier-Stokes equations can now be obtained by substituting the decomposed variables into the Navier-Stokes equations.

$$\frac{\partial \bar{u}_i}{\partial x_i} = 0 \tag{3.6}$$

$$\rho\left(\frac{\partial \bar{u}_i}{\partial t} + \bar{u}_j \frac{\partial \bar{u}_i}{\partial x_j}\right) = -\frac{\partial \bar{p}}{\partial x_i} + \mu \frac{\partial^2 \bar{u}_i}{\partial x_j^2} - \frac{\partial \rho \overline{u_i' u_j'}}{\partial x_j} \tag{3.7}$$

$$\frac{\partial \bar{\theta}}{\partial t} + \bar{u}_j \frac{\partial \bar{\theta}}{\partial x_j} = \kappa \frac{\partial^2 \bar{\theta}}{\partial x_j^2} - \frac{\partial \overline{u_j' \theta'}}{\partial x_j} \tag{3.8}$$

In these equations, $\mu = \nu/\rho$ is the dynamic viscosity, $\bar{p}$ the mean pressure and $\bar{u}$ the mean velocity in direction i.

Notice the last term of (3.7). This so-called Reynolds stress term represents the additional stress caused by the transportation of mean momentum by turbulent fluctuations. Using the equation for shear stress

$$\bar{\tau}_{ij} = 2\mu S_{ij} = \mu\left(\frac{\partial \bar{u}_i}{\partial x_j} + \frac{\partial \bar{u}_j}{\partial x_i}\right), \tag{3.9}$$

with S_{ij} the strain-rate tensor, (3.7) can be rewritten to

$$\rho \frac{\partial \bar{u}_i}{\partial t} + \rho \frac{\partial}{\partial x_j}\left(\bar{u}_i \bar{u}_j\right) = -\frac{\partial \bar{p}}{\partial x} + \frac{\partial}{\partial x_j}\left(\bar{\tau}_{ij} - \rho \overline{u_i' u_j'}\right). \tag{3.10}$$

The pressure and shear stress terms on the right hand side of this equation are related to molecular stress, while the term $\Sigma_{ij} \equiv -\rho \overline{u_i' u_j'}$ represents the turbulent stress tensor or Reynolds stress tensor.

As a result of the additional Reynolds stress terms, there are more unknowns than available equations. This so-called closure problem has to be resolved by introducing additional relationships between the variables. In order to close the problem, let's first compare the

molecular stress σ_{ij} to the turbulent stress tensor Σ_{ij}. The molecular shear stress is given by

$$\sigma_{ij} = -p\delta_{ij} + \tau_{ij} = -p\delta_{ij} + \mu\left(\frac{\partial u_i}{\partial x_j} + \frac{\partial u_j}{\partial x_i}\right), \tag{3.11}$$

in which the first part of the equation is the isotropic part related to pressure. The second part is deviatoric and caused by shear stress. Analogous to equation (3.11), the turbulent stress tensor can be rewritten to

$$\Sigma_{ij} = -\frac{1}{3}\rho\bar{u}_k^2\delta_{ij} + \rho\left(-\overline{u_i u_j} + \frac{1}{3}\bar{u}_k^2\delta_{ij}\right). \tag{3.12}$$

Here again, the first part of the equation is the isotropic part, which can be seen as turbulent pressure. The second part of the equation is the deviatoric part, interpretable as the turbulent shear stress. Based on the similarity of the Reynolds stress with the molecular stress, the Boussinesq hypothesis is formulated as

$$\rho\left(-\overline{u_i' u_j'} + \frac{1}{3}\overline{u_k'^2}\delta_{ij}\right) = \rho\nu_t\left(\frac{\partial \bar{u}_i}{\partial x_j} + \frac{\partial \bar{u}_j}{\partial x_i}\right) = 2\mu_T S_{ij}, \tag{3.13}$$

in which ν_T and μ_T are called the eddy or turbulent kinematic/dynamic viscosity.

The Boussinesq hypothesis shifts the closure problem towards determining the turbulent viscosity ν_T. Usually, one or more differential equations are constructed in order to determine this quantity. Based on the number of additional differential equations, the models are classified as zero-, half-, one- and two-equation models. This thesis will address several types of models: the one-equation Spalart-Allmaras model, the two-equation $k-\epsilon$ model and the two-equation Smith $k-l$ model. In the remainder of this chapter, the composition and prior uncertainty of these models will be described in Section 3.2, 3.3 and 3.4.

3.2 Parametric Uncertainty of the Spalart-Allmaras Turbulence Model

3.2.1 The Composition of the Spalart-Allmaras Turbulence Model

This section presents the Spalart-Allmaras (SA) model the way it was originally defined in 1992 [22], with the exception of the so-called transition terms[1]. It is important to understand how the SA model is constructed, because it is its particular composition which finally leads to the uncertainty in the model's predictions. As mentioned in the introduction of this chapter, the SA model is a one-equation model. In this case, the single additional equation represents transport of turbulent viscosity, and is constructed by means of dimensional analysis and empiricism. The following describes step by step how the equation is constructed. It does this by defining the relationship for a simple free shear flow first. Consequently, terms are added to include the effects of walls for an approximately inviscid and, finally, viscous flow.

[1]The transition terms provide control over the laminar region of the shear layers, i.e. these terms determine where transition from laminar to turbulent flow occurs. Note that the SA model can by no means predict transition. For more information about the transition terms, see reference [22].

Free Shear Flows

As was mentioned in the introduction of this section, the additional equation models transport of turbulent viscosity ν_t. Its simplest version is constructed for free shear flows at high Reynolds numbers. Consequently, molecular viscosity is negligible. For such flows, it can be assumed that the energy cascades unidirectionally from the largest towards the smaller scales. This assumption results from the conceptualization of turbulent flows as a superposition of so-called eddies, which are broadly defined as coherent patterns of velocity, vorticity and pressure at different scales. The largest eddies are created by instabilities in the mean flow and are intrinsically unstable. As a result they brake down into ever smaller eddies, until their energy is finally dissipated at the smallest, or Kolmogorov scales. This is what is referred to as the energy cascade.

With this assumption in mind, the first version of the model can be constructed. The left-hand side of the equation consists of the material derivative of the turbulent viscosity, representing its rate of change in time. The right-hand side of the equation is composed of a production term and a diffusion term. For the production term, the scalar norm S of the strain rate tensor $S_{ij} \equiv (\frac{\partial U_i}{\partial x_j} + \frac{\partial U_j}{\partial x_i})/2$ is multiplied by the turbulent viscosity and a so-called basic coefficient c_{b1}. The diffusion term consists of the spatial derivatives of ν_t, a second basic coefficient c_{b2} and a Prandtl number σ. The basic model for free shear flows then becomes:

$$\frac{D\nu_t}{Dt} = c_{b1} S \nu_t + \frac{1}{\sigma}\left[\nabla\left(\nu_t \nabla \nu_t\right) + c_{b2}\left(\nabla \nu_t\right)^2\right]. \tag{3.14}$$

Notice that this version of the SA model contains three closure coefficients, i.e. $\sigma = 2/3$, $c_{b1} = 0.1355$ and $c_{b2} = 0.622$. Their values have been determined by calibrating the model with experimental data for mixing layers and wakes. A more thorough discussion of how the closure coefficients are determined will follow in Section 3.2.2.

This concludes the discussion of the SA model for free shear flows. The next section will tune this model in such a way that it becomes capable of predicting wall-bounded flows at high Reynolds numbers, i.e. inviscid wall-bounded flows.

Near-wall Region, High Reynolds Number

Additional terms need to be added to the free shear flow version of the model (3.14) in order to predict the behaviour of wall-bounded flows. The presence of a wall causes a disturbance in the pressure term which is felt throughout the flow, and acts as a destruction term for the Reynolds shear stress. Such a destruction term can be defined as a negative contribution to the turbulent viscosity. Furthermore, its effect becomes negligible far away from the wall, hence from dimensional analysis the destruction term can be defined as $-c_{w1}(\nu_t/d)^2$, with d the distance to the wall. The coefficient c_{w1} cannot be determined independently, as an equilibrium between the production and diffusion terms (both positive) and the destruction term is required. Knowing that $S = u_\tau/(\kappa d)$ and $\nu_t = u_\tau \kappa d$ in the log layer[2], with friction

[2]After Reynolds-averaging the Navier-Stokes equations, wall-bounded flows can be divided into several regions in which certain laws apply. These regions are usually called the viscous sublayer and buffer layer, together forming the inner layer, the overlap or log layer, and the outer layer. See Appendix F for a more thorough discussion on this topic.

velocity u_τ and Von Kármán constant $\kappa = 0.41$, c_{w1} is constrained as follows:

$$c_{w1} = c_{b1}/\kappa^2 + (1 + c_{b2})/\sigma. \tag{3.15}$$

Note that up to now there are a total of five parameters defined: σ, c_{b1}, c_{b2}, c_{w1} and κ. However, there are only two independent parameters, which are a turbulent Prandtl number σ and the Von Kármán constant κ.

According to Spalart and Allmaras, tests show that the model including the destruction term makes an accurate prediction of the log layer. However, its prediction for the friction coefficient is too low. In order to overcome this deficiency, the destruction term needs to be multiplied with a function f_w, which makes the destruction term decrease faster within the outer region of the boundary layer. To guarantee equilibrium, this function is of non-dimensional nature and equals 1 within the log layer.

The non-dimensional variable r of the function f_w equals the square of $l_m/\kappa d$, in which $l_m \equiv \sqrt{\nu_t/S}$ represents the mixing length[3]. With this in mind, the wall function f_w is defined as follows:

$$\begin{aligned} f_w(r) &= g\left[\frac{1 + c_{w3}^6}{g^6 + c_{w3}^6}\right]^{1/6} \\ g &= r + c_{w2}(r^6 - r) \\ r &\equiv \frac{\nu_t}{S\kappa^2 d^2}. \end{aligned} \tag{3.16}$$

The transport equation for turbulent viscosity which includes the effects of walls at high Reynolds numbers results into the second version of the model:

$$\frac{D\nu_t}{Dt} = c_{b1} S \nu_t + \frac{1}{\sigma}\left[\nabla\left(\nu_t \nabla \nu_t\right) + c_{b2}\left(\nabla \nu_t\right)^2\right] - c_{w1} f_w \left[\frac{\nu_t}{d}\right]^2. \tag{3.17}$$

This version of the model introduces two additional independent parameters, i.e. c_{w2} and c_{w3}. The original paper of Spalart and Allmaras states that the results are most sensitive to the slope of f_w, which is controlled by c_{w2}. The coefficient c_{w3} is used in the conversion of g into f_w, which is only intended to prevent undesirably large values of f_w. About the value of c_{w3}, Spalart and Allmaras say nothing more than that 2 is a reasonable value for it. After setting c_{w3} equal to 2, the wall coefficient c_{w2} is calibrated such that the resulting friction coefficient matches the friction coefficient for a flat plate boundary layer. This is done for a friction coefficient of $C_f = 0.00262$ at $Re_\theta = 10^4$, and results into $c_{w2} = 0.3$.

The model given by equation (3.17) is capable of predicting wall-bounded flows at high Reynolds numbers. Finally, we would also like to predict wall-bounded flows for low Reynolds numbers, where viscous effects become important. Therefore, the following section discusses the third version of the SA model, which takes these effects into account.

[3]Ludwig Prandtl introduced the concept of mixing length l_m. It is based on the fact that for a turbulent boundary layer, the turbulent viscosity varies with the distance from the wall: $\nu_t = S l_m^2$

Near-wall Region, Finite Reynolds Number

When including the viscous effects into the SA model, some additional tuning is needed for the buffer layer and viscous sublayer. The turbulent viscosity ν_t in the buffer layer cannot be modelled in the same way as for the log layer, i.e. $\nu_t = \kappa y u_\tau$. In order to model the near-wall behaviour correctly, a damping function f_{v1} is introduced, and multiplied with the turbulent viscosity as modelled for the log layer, i.e. $\tilde{\nu} \equiv \kappa y u_\tau$. The turbulent viscosity for the entire flow is defined as

$$\nu_t = \tilde{\nu} f_{v1}, \qquad f_{v1} = \frac{\chi^3}{\chi^3 + c_{v1}^3}, \tag{3.18}$$

in which $\chi \equiv \dfrac{\tilde{\nu}}{\nu}$, with ν the molecular viscosity.

Finally, a similar kind of damping function is applied to the production term, i.e. $c_{b1} S \nu_t$. Its strain rate tensor S is redefined as

$$\tilde{S} \equiv S + \frac{\tilde{\nu}}{\kappa^2 d^2} f_{v2}, \qquad f_{v2} = 1 - \frac{\chi}{1 + \chi f_{v1}}. \tag{3.19}$$

This way, also $\tilde{S}$ maintains its log-layer behaviour all the way to the wall. As such, the standard version of the SA model is fully defined by (3.20). The relations between its variables are given by (3.21).

$$\frac{\partial \tilde{\nu}}{\partial t} + \bar{u}_j \frac{\partial \tilde{\nu}}{\partial x_j} = c_{b1} \tilde{S} \tilde{\nu} - c_{w1} f_w \left(\frac{\tilde{\nu}}{d} \right)^2 + \frac{c_{b2}}{\sigma} \frac{\partial \tilde{\nu}}{\partial x_k} \frac{\partial \tilde{\nu}}{\partial x_k} + \frac{1}{\sigma} \frac{\partial}{\partial x_k} \left[(\nu + \tilde{\nu}) \frac{\partial \tilde{\nu}}{\partial x_k} \right], \tag{3.20}$$

$$\begin{aligned} \text{where;} \quad \nu_t = \tilde{\nu} f_{v1}, \quad \chi = \frac{\tilde{\nu}}{\nu}, \quad r = \frac{\tilde{\nu}}{\tilde{S} \kappa^2 d^2}, \quad g = r + c_{w2} \left(r^6 - r \right), \\ f_{v1} = \frac{\chi^3}{\chi^3 + c_{v1}^3}, \quad f_{v2} = 1 - \frac{\chi}{1 + \chi f_{v1}}, \quad f_w = g \left[\frac{1 + c_{w3}^6}{g^6 + c_{w3}^6} \right]^{1/6}, \\ \tilde{S} = \sqrt{2 \Omega_{ij} \Omega_{ij}} + \frac{\tilde{\nu}}{\kappa^2 d^2} f_{v2}, \quad \Omega_{ij} = \frac{1}{2} \left(\frac{\partial \bar{u}_i}{\partial x_j} - \frac{\partial \bar{u}_j}{\partial x_i} \right). \end{aligned} \tag{3.21}$$

From the above, it can be concluded that there are a total of seven closure coefficients: σ, c_{b1}, c_{b2} κ, c_{w2}, c_{w3} and c_{v1}. The first wall coefficient c_{w1} is considered to be a function of κ, σ, c_{b1} and c_{b2} as defined by equation (3.15). The suggested values for these constants by Spalart and Allmaras are listed below:

$$\sigma = 2/3, \quad c_{b1} = 0.1355, \quad c_{b2} = 0.622, \quad \kappa = 0.41, \quad c_{w2} = 0.3, \quad c_{w3} = 2, \quad c_{v1} = 7.1$$

From the derivation of the SA model, its empirical nature becomes apparent. The model itself is a composition of approximations, and also its parameters are uncertain. Particularly this parametric uncertainty is what will be discussed in the coming section.

3.2.2 The Prior Uncertainty of the Spalart-Allmaras' Closure Coefficients

The Von Kármán Constant

The Von Kármán constant is a returning dimensionless constant in many turbulence models as it describes the velocity profile of a turbulent boundary layer within the log-layer. Within this layer, the velocity profile is determined by

$$u^+ = \frac{1}{\kappa} \ln\left(y^+\right) + C^+. \tag{3.22}$$

A common value for the Von Kármán constant is $\kappa = 0.41$, however, other values have been reported by several authors of which plenty are conveniently summarized by Zanoun et al. [26]. In this article, the Von Kármán constant ranges from 0.33 to 0.45, often in combination with a varying value for the constant C^+.

Now, let's have a look at the velocity profiles of the experiments we are using for calibration in this thesis. We will consider incompressible flat plate flow for a zero, a favourable and an adverse pressure gradient is considered. Figure 3.1 shows that their profiles more or less coincide where the log-layer holds. In addition, the logarithmic law is plotted for the minimum and maximum values of the Von Kármán constant as found by Zanoun et al., i.e. $\kappa = 0.33$ and $\kappa = 0.45$, and the common value for the Von Kármán constant $\kappa = 0.41$. Figure 3.1 (a) assumes a constant value for $C^+ = 5.5$, while in Figure 3.1 (b) this constant varies.

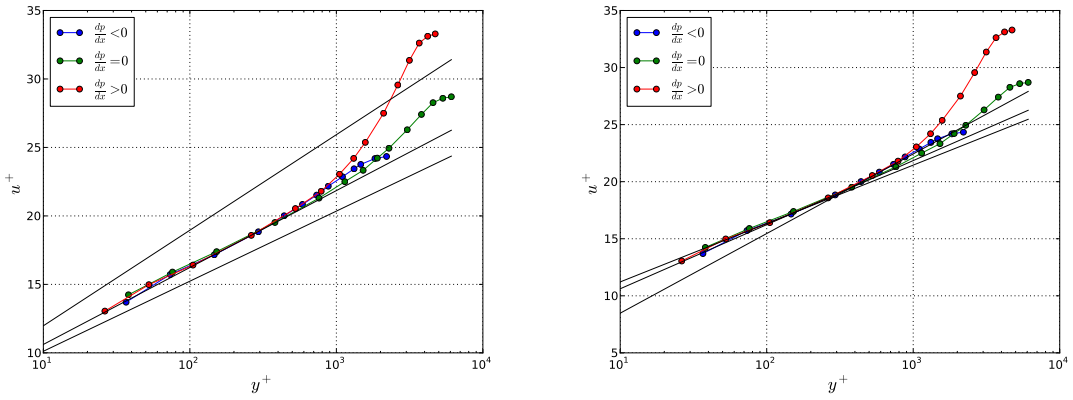

(a) (b)

Figure 3.1: These graphs show the velocity profiles for a turbulent flat plate flow under zero, adverse and favourable pressure gradient conditions. In addition, (a) shows the plots of the logarithmic law for varying κ and constant C^+, while in (b) also C^+ is varying.

Figure 3.1 (b) seems to confirm that various values for the Von Kármán constant, in combination with a certain value for C^+, can deliver a velocity profile which is in close agreement with experimental values. For a value of $\kappa = 0.33$, which is a relatively large deviation from

its common value, the slope of the velocity profile deviates significantly. However, it seems to coincide with the experimental velocity profiles for higher values of y^+. Hence, one could conclude that the value for the Von Kármán constant also depends on the chosen borders of the log-layer, which are indeed uncertain as well.

From the arguments above, it is concluded that choosing an interval ranging from [0.3-0.5] should suffice to include all physically possible values for the Von Kármán constant. Larger deviations would generate unrealistic slopes of the velocity profiles within the log-layer.

The Spalart-Allmaras Turbulent Prandtl Number and Basic Coefficients

Notice that there are three coefficients in the model which need to be calibrated, i.e. c_{b1}, c_{b2} and σ. According to Spalart and Allmaras, this can be done by requiring correct levels of shear stress for two-dimensional mixing layers and wakes. In their original paper, they assume peak shear stresses of $0.01(\Delta U)^2$ and $0.06(\Delta U)^2$ for the mixing layers and wakes, respectively, in which ΔU represents the peak velocity difference. From these conditions, the coefficients c_{b1} and c_{b2} can be expressed in terms of σ by equations (3.23) and (3.24), respectively. Note that these relationships, as well as Figure 3.2 are derived from a similar image as presented in the original Spalart-Allmaras paper [22].

$$10c_{b1} = 0,187\sigma^2 - 0,4973\sigma + 1,6046 \tag{3.23}$$

$$1 + c_{b2} = 0,0751\sigma^2 + 0,0834\sigma + 1,5321 \tag{3.24}$$

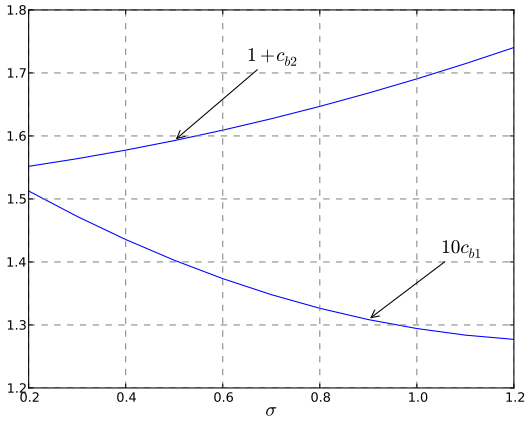

Figure 3.2: The basic coefficients c_{b1} and c_{b2} in relation to σ.

Originally, Spalart and Allmaras assumed the plausible range of σ to be at most [0.6-1]. First of all, from their paper, it is unclear how they arrived at this assumption. Consequently, by choosing different values for σ within this plausible range, they matched their results for a mixing layer to existing numerical data. Based on how well their results match the data, they "favour a fairly diffusive member of the plausible range". Finally, a value for $\sigma = 2/3$

was chosen, which corresponds to $c_{b1} = 0.1355$ and $c_{b2} = 0.622$. They state that the peak turbulent viscosity in the wake is in good agreement with experimental results for these values.

One can see that the approach to determine the coefficients is of an empirical nature. Finally, it is questionable whether choosing a constant value for these coefficients is the correct approach to simulate different flow cases. Of course, this has been considered by Spalart and Allmaras as well. They for example did not attempt to match their results to any axisymmetric flow, and also mention the model is not intended to be universal. This confirms what is stated in Section 1.1; it is important to choose an appropriate model for the investigated quantity of interest.

In this thesis, we will consider the full plausible range of σ, which was defined to range from [0.6-1] by Spalart and Allmaras.

The Wall Coefficients

When looking back to the relations given in (3.21), we see that the function f_w uses the wall constants c_{w2} and c_{w3}. The original paper by Spalart and Allmaras [22] states that the results are most sensitive to the slope of f_w at $r = 1$, which is controlled by c_{w2} as can be seen from Figure 3.3 (a). The conversion of the function g into f_w only serves the purpose of preventing large values for f_w. Basically no argumentation for a value of $c_{w3} = 2$ is given, except that it is a reasonable value. In fact, Figure 3.3 (b) shows that the closure coefficient $c_{w3} = 2$ has no influence on the value for f_w.

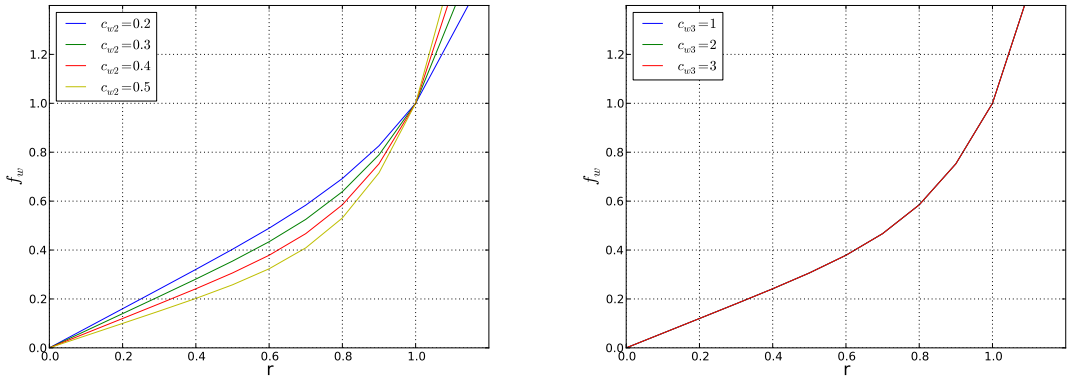

(a) (b)

Figure 3.3: These graphs show the variation of the wall function f_w with changing wall coefficients c_{w2} and c_{w3}, respectively (a) and (b).

After defining the value of $c_{w3} = 2$, Spalart and Allmaras[22] calibrated c_{w2} such that the predicted skin-friction coefficient would match the one in a flat-plate boundary layer. Finally, a value of $c_{w2} = 0.3$ was determined based on a friction coefficient of $C_f = 0.00262$ at

$Re_\theta = 10^4$. In the paper of Cheung et al., an interval of ±50% of the nominal value was chosen. Although the resulting posterior distribution for $c_{w2} = 0.3$ of Cheung et al. remains more or less within these bounds, it tends towards the upper boundary of the chosen range. Therefore we define a uniform distribution for c_{w2} ranging from [0.2-0.5]. Although it is expected that the value for closure coefficient c_{w3} will have little influence, it is still assumed uncertain and given a range of [0.2-0.5]. As such, it can be checked whether our hypothesis is correct.

The Viscous Coefficient

Equation (3.18) introduces the viscous coefficient c_{v1}. The value of this closure coefficient is based on Spalart and Allmaras' believes of where the point is located at which the velocity profile can be modelled by means of the log law (3.22). They mention that Mellor and Herring, of whom they borrowed the f_{v1} function, use a value of $c_{v1} = 6.9$. Spalart and Allmaras state that this yields a low intercept of the log law, which is why they prefer a value of $c_{v1} = 7.1$. Based on the fact that the prior distribution defined by Cheung et al.[2] proved to be satisfactory, i.e. keeping the posterior well within bounds, we define a uniform prior distribution with bounds [4.0-10.0] for the coefficient c_{v1}.

A total of five uncertain closure coefficients have been defined. A summary of the ranges of their prior uniform distributions is given in Table 3.1.

Table 3.1: Summary of the ranges for the prior uniform distributions of the SA closure coefficients

Parameter	Lower	Upper
κ	0.3	0.5
σ	0.6	1.0
c_{w2}	0.2	0.5
c_{w3}	1.0	3.0
c_{v1}	4.0	10.0

3.3 Parametric Uncertainty of the $k-\epsilon$ Turbulence Model

3.3.1 The Composition of a $k-\epsilon$ Turbulence Model

The $k-\epsilon$ turbulence models obtain the local turbulent viscosity (3.25) by means of solving the transport equations for the turbulent kinetic energy (3.26) and the energy dissipation rate (3.27).

$$\mu_T = C_\mu f_\mu \rho k^2/\epsilon \tag{3.25}$$

$$\rho\frac{\mathrm{D}k}{\mathrm{D}t} = \frac{\partial}{\partial y}\left[\left(\mu+\frac{\mu_T}{\sigma_k}\right)\frac{\partial k}{\partial y}\right] + \mu_T\left(\frac{\partial u}{\partial y}\right)^2 - \rho\epsilon - 2\mu\left(\frac{\partial k^{\frac{1}{2}}}{\partial y}\right)^2 \tag{3.26}$$

$$\rho\frac{\mathrm{D}\epsilon}{\mathrm{D}t} = \frac{\partial}{\partial y}\left[\left(\mu+\frac{\mu_T}{\sigma_\epsilon}\right)\frac{\partial \epsilon}{\partial y}\right] + C_{\epsilon 1}f_1\frac{\epsilon}{k}\mu_T\left(\frac{\partial u}{\partial y}\right)^2 - C_{\epsilon 2}f_2\frac{\rho\epsilon^2}{k} + 2\mu\mu_T\left(\frac{\partial^2 u}{\partial y^2}\right) \tag{3.27}$$

The boundary conditions for the turbulent kinetic energy $k[m^2/s^2]$ and the energy dissipation rate $\epsilon[m^2/s^3]$ are defined as follows, where y indicates the distance from a wall:

$$y = 0; \quad k = 0, \quad \epsilon = 0 \quad \text{and} \tag{3.28}$$

$$y = y_G; \quad u_G\frac{dk_G}{dx} = -\epsilon_G, \quad u_G\frac{d\epsilon_G}{dx} = -C_{\epsilon 2}f_2\epsilon_G^2/k_G. \tag{3.29}$$

The subscript G denotes the free-stream conditions.

In the RANS code of Cinnella, there are three $k-\epsilon$ models available, i.e. Launder-Sharma, Jones-Launder and Chien. The difference between these models is in the definition of the damping functions and the closure coefficients. A summary of these for the three $k-\epsilon$ models included is given in Table 3.2, where $Re_T \equiv \frac{k^2}{\nu\epsilon}$.

Table 3.2: Summary of closure coefficients and damping functions for the $k-\epsilon$ model.

	Launder-Sharma	Jones-Launder	Chien
Damp. Func.			
f_1	1.0	1.0	1.0
f_2	$1.0-0.3\exp(-Re_T^2)$	$1.0-0.3\exp(-Re_T^2)$	$1.0-0.22\exp(-\frac{Re_T}{6})^2$
f_μ	$\exp[-3.4/(1+Re_T/50)]$	$\exp[-2.5/(1+Re_T/50)]$	$1.0-\exp(-0.0115y^+)$
Clos. Coeff.			
C_μ	0.09	0.09	0.09
$C_{\epsilon 1}$	1.44	1.55	1.35
$C_{\epsilon 2}$	1.92	2.0	1.8
σ_k	1.0	1.0	1.0
σ_ϵ	1.3	1.3	1.3

Notice that the Jones-Launder and Launder-Sharma turbulence model use the same damping functions, except for a slight difference in the numerator value for f_μ's exponent. It will be interesting to see whether there is a similarity in the calibrated results for these two models. To reduce the simulation time, we therefore opted to simulate only these two $k-\epsilon$ models and disregard the Chien model.

3.3.2 The Prior Uncertainty of the $k-\epsilon$ Turbulence Model's Closure Coefficients

Note that the below is largely based on work of Platteeuw [19] and Edeling [5].

Coefficient $C_{\epsilon 2}$

The traditional calibration method starts with considering a homogeneous, decaying turbulent flow, i.e. gradients and production equal zero. As a result, (3.26) and (3.27) reduce to

$$\frac{dk}{dt} = -\epsilon \tag{3.30}$$

$$\frac{d\epsilon}{dt} = -C_{\epsilon 2}\frac{\epsilon^2}{k} \tag{3.31}$$

The solutions for these equations are

$$k(t) = k_0 \left(\frac{t}{t_0}\right)^{-n} \tag{3.32}$$

and

$$\epsilon(t) = \epsilon_0 \left(\frac{t}{t_0}\right)^{-(n+1)} \tag{3.33}$$

where k and ϵ have the values k_0 and ϵ_0 at reference time $t_0 = n\dfrac{k_0}{\epsilon_0}$, and $n = 1/\left(C_{\epsilon 2} - 1\right)$. Hence, the closure coefficient $C_{\epsilon 2}$ is actually fully dependent on the decay exponent n.

$$C_{\epsilon 2} = \frac{n+1}{n} \tag{3.34}$$

Mohamed & LaRue [14] have investigated the value of the decay exponent n with respect to the Reynolds number Re_{M_u}. They looked at four cases with changing mesh size ($M_u = 2.54$ cm to $M_u = 5.08$ cm) or solidity ($\sigma = 0.34$ to $\sigma = 0.44$). Each of these cases is pictured in Figure 3.4. From this figure, we observe that the minimum value attained for the decay component equals about $n = 1.23$, while reaching a maximum value of about $n = 1.34$. For convenience, the relationship between $C_{\epsilon 2}$ and n will be coded into pyPCM. As a consequence, we'll investigate the decay exponent as the uncertain parameter instead of $C_{\epsilon 2}$ directly. The used interval for the decay exponent will be $n = [1.23 - 1.34]$.

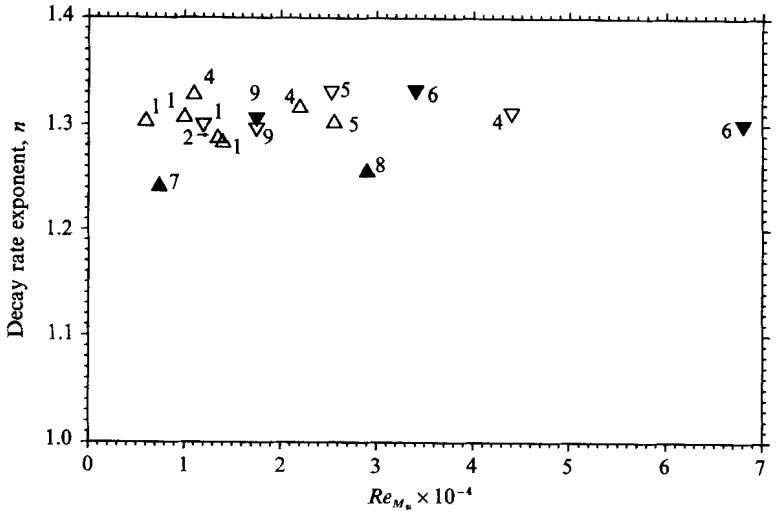

Figure 3.4: This figure shows the variation of the decay exponent n for different Reynolds numbers, mesh sizes M_u and solidities σ [14].

Coefficient C_μ

In order to calibrate the coefficient C_μ, we consider the approximate balance between production and dissipation which exists in free shear flows and certain parts of the boundary layers, i.e.

$$\mathcal{P} = -\overline{u'v'}\frac{\partial u_i}{\partial x_j} = C_\mu \frac{k^2}{\epsilon}\left(\frac{\partial u_i}{\partial x_j}\right)^2 = \epsilon \tag{3.35}$$

Iwamoto and Hoyas & Jimenez simulated a free shear flow using direct numerical simulation at Reynolds numbers ranging from $Re_\tau = [110 - 2000]$. The results of these simulations can be substituted into Equation (3.35), of which the outcome is presented in Figure 3.5. Note that there seems to be quite some variation in the value of C_{mu}. Close to the wall, a steep gradient can be observed. Furthermore, overall, the value for C_μ is decreasing with increasing Reynolds number. To cover the full spectrum of values for C_μ, a range is taken of $C_\mu = [0.02 - 0.14]$.

Coefficient $C_{\epsilon 1}$

The value for $C_{\epsilon 1}$ can be found by considering a uniform shear flow ($S = \frac{\partial u}{\partial y} = c^{st}$). For these kind of flows, Reynolds stresses are self-similar and the non-dimensional parameters Sk/ϵ and P/ϵ are constant. As a consequence, also the turbulence timescale $\tau \equiv k/\epsilon$ is constant. Taking these conditions into account, the following equation can be derived from the governing equations (3.26) and (3.27):

$$\frac{\mathrm{d}}{\mathrm{d}t}\left(\frac{k}{\epsilon}\right) = \frac{\mathrm{d}\tau}{\mathrm{d}t} = (C_{\epsilon 2} - 1) - (C_{\epsilon 1} - 1)\left(\frac{P}{\epsilon}\right). \tag{3.36}$$

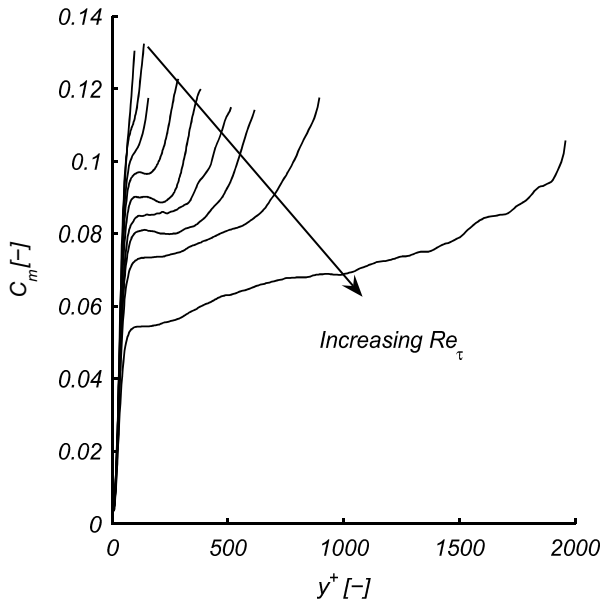

Figure 3.5: This figure shows the variation of the decay exponent n for different Reynolds numbers, mesh sizes M_u and solidities σ [14].

As the timescale $\tau \equiv k/\epsilon$ is constant, the following holds:

$$\left(\frac{P}{\epsilon}\right) = \frac{C_{\epsilon 2} - 1}{C_{\epsilon 1} - 1}. \tag{3.37}$$

As a consequence, the coefficient $C_{\epsilon 1}$ can be expressed as a function of $C_{\epsilon 2}$ and the ratio P/ϵ.

$$C_{\epsilon 1} = \frac{1}{(P/\epsilon)} C_{\epsilon 2} + \frac{(P/\epsilon) - 1}{(P/\epsilon)} \tag{3.38}$$

This last relation will be coded into pyPCM. Consequently, the uncertainty parameter becomes the ratio P/ϵ. The value which is normally taken for the $k-\epsilon$ model is 2.09. However, Tavoularis et al. reported P/ϵ values between 1.33 and 1.75 for several uniform flows. We will consider a relatively wide range, i.e. $P/\epsilon = [1.30 - 2.90]$.

Coefficient σ_ϵ

When calibrating for the coefficient σ_ϵ, we need to take a constraint into account which results from considering a fully developed channel flow.

$$\kappa^2 = \sigma \epsilon C_\mu^{1/2} \left(C_{\epsilon 2} - C_{\epsilon 1}\right) \tag{3.39}$$

Notice the introduction of the Von Kármán constant, whose uncertainty interval is already defined for the Spalart-Allmaras turbulence model. In addition, the interval for coefficients $C_{\epsilon 1}$ and $C_{\epsilon 2}$ was defined earlier in this chapter. As a consequence, we have all the information to derive the interval for σ_ϵ. However, for convenience, we will continue with using the Von Kármán constant as the uncertain parameter and code the relationship with σ_ϵ in pyPCM.

Coefficient σ_k

The coefficient σ_k represents the turbulent Prandtl number. Generally, very little experimental data can be found regarding this model constant. As a result, a rather crude estimate of the range will be taken, i.e. $\pm 50\%$ of its nominal value $\sigma_k = [0.5 - 1.5]$.

This concludes the discussion on the uncertainty parameters for the $k-\epsilon$ turbulence model. Notice that throughout the discussion, constraints and dependencies were found which shifted the uncertainty from the closure coefficient level to other dependent parameters. Table 3.3 summarizes the parameters we will work with during the calibration and their considered intervals.

Table 3.3: Summary of the ranges for the prior uniform distributions of the $k-\epsilon$ uncertain parameters

Parameter	Lower	Upper
n	1.23	1.34
C_μ	0.02	0.14
P/ϵ	1.30	2.90
κ	0.3	0.5
σ_k	0.5	1.5

3.4 Parametric Uncertainty of Smith's $k-l$ Turbulence Model

3.4.1 The Composition of Smith's $k-l$ Turbulence Model

This section presents the original $k-l$ turbulence model as defined by Smith [21]. The $k-l$ model is a rewritten version of the $k-kl$ model, such that it would be able to predict the profiles of turbulent kinetic energy and velocity in the viscous sublayer of a turbulent boundary layer. Both the $k-l$ and $k-kl$ model are similar to the $k-\epsilon$ models. The main difference between them is in the definition of the second transport equation, which is used to define the dissipation length scale.Compared to the $k-\epsilon$ model, the $k-l$ model has the advantage that it is much easier to resolve numerically. Moreover, Smith claims the model is more accurate for compressible turbulent boundary layer flows.

The first equation models the transport of turbulent kinetic energy in terms of k:

$$\rho \frac{\mathrm{D}k}{\mathrm{D}t} = P - \frac{\rho\,(2k)^{3/2}}{B_1 l} + \frac{\partial}{\partial x_i}\left[\left(\mu + \frac{\mu_T}{\sigma_k}\right)\frac{\partial k}{\partial x_i}\right] - 2\mu \frac{\partial k^{1/2}}{\partial x_i}\frac{\partial k^{1/2}}{\partial x_i}. \tag{3.40}$$

Here, P represents the turbulence production

$$P = \tau_{ij}^{'} \frac{\partial U_i}{\partial x_j}. \tag{3.41}$$

The Boussinesq hypothesis is used to obtain the turbulent stresses

$$\tau_{ij}^{'} = \mu_T \left[\left(\frac{\partial u_i}{\partial x_j} + \frac{\partial u_j}{\partial x_i} \right) - \frac{2}{3} \left(\frac{\partial u_i}{\partial x_i} \right) \right] - \frac{2}{3} \rho k \delta_{ij}. \tag{3.42}$$

The next step is to find an equation for the turbulent length scale l. First, near wall terms need to be added to the kl equation Smith defined in his earlier paper [20]. Doing this results in

$$\rho \frac{\mathrm{D}q^2 l}{\mathrm{D}t} = E_1 l P - \frac{\rho q^3}{B_1} \left[E_2 + (2 - E_2) \left(\frac{l}{\kappa d} \right)^2 \right] - 2\mu l \frac{\partial q}{\partial x_i} \frac{\partial q}{\partial x_i} - 2\mu \frac{\partial l}{\partial x_i} \frac{\partial q^2}{\partial x_i} - q^2 \frac{\mu_T}{\sigma_l l} \frac{\partial l}{\partial x_i} \frac{\partial l}{\partial x_i} \left(\frac{l}{\kappa d} \right)^2 + \frac{\partial}{\partial x_i} \left(\mu + \frac{\mu_T}{\sigma_l} \right) \frac{\partial q^2 l}{\partial x_i} \tag{3.43}$$

where $q^2 = 2k$, d depicts the distance to the wall, and E_1 and E_2 are empirical constants. As $q \propto y$ and $l \propto y$, $q^2 l$ becomes very small near the wall, which causes numerical problems. Rewriting Equation (3.43) in terms of l solves these problems.

$$\rho \frac{\mathrm{D}l}{\mathrm{D}t} = (2 - E_2) \frac{\rho q}{B_1} \left[1 - \left(\frac{l}{\kappa d} \right)^2 \right] - \frac{\mu_T}{\sigma_l l} \frac{\partial l}{\partial x_i} \frac{\partial l}{\partial x_i} \left(\frac{l}{\kappa d} \right)^2 + \frac{2\mu_T}{\sigma_l q^2} \frac{\partial l}{\partial x_i} \frac{\partial q^2}{\partial x_i} + \frac{\partial}{\partial x_i} \left[\left(\mu + \frac{\mu_T}{\sigma_l} \right) \frac{\partial l}{\partial x_i} \right] \tag{3.44}$$

Note that the length scale production term can only be eliminated when empirical constant $E_1 = 2.0$. Finally, as $q^2 = 2k$, (3.44) is rewritten in terms of k, such that consistency with (3.40) is guaranteed:

$$\rho \frac{\mathrm{D}l}{\mathrm{D}t} = (2 - E_2) \frac{\rho \sqrt{2k}}{B_1} \left[1 - \left(\frac{l}{\kappa d} \right)^2 \right] - \frac{\mu_T}{\sigma_l l} \frac{\partial l}{\partial x_i} \frac{\partial l}{\partial x_i} \left(\frac{l}{\kappa d} \right)^2 + \frac{2\mu_T}{\sigma_l k} \frac{\partial l}{\partial x_i} \frac{\partial k}{\partial x_i} + \frac{\partial}{\partial x_i} \left[\left(\mu + \frac{\mu_T}{\sigma_l} \right) \frac{\partial l}{\partial x_i} \right]. \tag{3.45}$$

The turbulent viscosity μ_T for the $k - l$ turbulence model is a function of the molecular viscosity μ, the turbulent kinetic energy and the turbulent length scale. This is expressed by the relationships given in (3.46). Here, f_μ is a damping function for the turbulent viscosity in the viscous sublayer and buffer regions. In the logarithmic layer and up, $f_\mu = 1$. The constants for the damping function are set to $c_1 = 25.5$ and $c_2 = 2.0$.

Finally, the Menter shear stress transport (SST) correction is applied to the researched $k - l$ model. This correction is based on the empirical Bradshaw's assumption, connecting the shear stress to the turbulent kinetic energy for a two-dimensional boundary layer:

$$\frac{-\overline{u'v'}}{k} = \sqrt{\frac{P_k}{\epsilon}} \sqrt{C_\mu}, \tag{3.47}$$

$$\begin{aligned} \mu_T &= \mu\chi f_\mu \quad ; \quad \chi = \frac{\rho\sqrt{2k}l}{\mu B_1^{1/3}} \\ f_\mu &= \left(\frac{c_1^4 f_1 + c_2^2\chi^2 + \chi^4}{c_1^4 + c_2^2\chi^2 + \chi^4}\right)^{1/4} \quad ; \quad f_1 = \exp\left[-50\left(\frac{l}{\kappa d}\right)^2\right] \end{aligned} \tag{3.46}$$

in which the constant $C_\mu = 0.09$. The constraint on the turbulent viscosity, derived from Bradshaw's assumption, reads as follows in case of the $k-l$ model:

$$\nu_T = \min\left[\frac{\mu\chi f_\mu}{\rho}, \frac{ck}{\sqrt{2}|\Omega|F_2(y)}\right], \tag{3.48}$$

in which $c = 0.3$, Ω represents the vorticity and F_2 is a so-called blending function tending to zero outside of the boundary layer.

Finally, for the entire model, we investigate five empirical constants: $\kappa = 0.41$, $B_1 = 18$, $E_2 = 1.2$, $\sigma_k = \sigma_l = 1.43$ and $C_\mu = 0.09$. Note that $E_1 = 2.0$ cannot be varied, or Equation (3.45) will not hold.

The next section will dive deeper into the determination and possible variation of the closure coefficients.

3.4.2 The Prior Uncertainty of the $k-l$ Turbulence Model's Closure Coefficients

This section discusses the prior uncertainty of the closure coefficients for the $k-l$ turbulence model, i.e. κ, B_1, E_2, $\sigma_k = \sigma_l$ and C_μ. Just as with the SA and $k-\epsilon$ turbulence models, a uniform distribution is assumed for all coefficients.

The prior uncertainty of the Von Kármán constant κ is already defined in Section 3.2.2. Therefore, we will use the same interval in the case of the $k-l$ model. Secondly, the Menter coefficient is defined by Bradshaw's assumption (3.47). Knowing that $P = -\overline{u'v'}S$, the Menter coefficient can be expressed as

$$c_\mu = \frac{P_k}{\epsilon}\left(\frac{\epsilon}{Sk}\right)^2. \tag{3.49}$$

This definition equals the one for the c_μ coefficient of the $k-\epsilon$ turbulence models. As a consequence, also the same prior uncertainty range is taken into account for the Menter coefficient.

Regarding the tuning of the coefficients B_1, E_2, σ_k and σ_l, very little information can be found. In his original paper on the $k-kl$ turbulence model, Smith only mentions that the constants were determined from simple shear flows, flat plate boundary layer flows, and the decay of isotropic turbulence. For this model, the coefficients were defined as $B_1 = 19.25$,

$E_2 = 0.7$, $\sigma_k = \sigma_l = 5$. In his succeeding paper on the $k-l$ turbulence model, these values change. The constants then become $B_1 = 18.00$, $E_2 = 1.2$, $\sigma_k = \sigma_l = 1.43$.

As the information on the tuning of the coefficients is very limited, we will have to make some assumptions on their prior uncertainty range. These assumptions will be based on the amount of variation of the coefficients by comparing their values for the $k-kl$ and $k-l$ turbulence model. In case of the coefficient B_1, a relatively small variation in the value of the coefficient is observed, i.e. $B_1 = 19.25$ compared to $B_1 = 18.00$. Therefore a range for B_1 of $[15-21]$ is taken, which is slightly more than double the variation observed when comparing the B_1 values for $k-l$ and $k-kl$ model. It is assumed that this double margin should be sufficient to include all possible values for the coefficient. In line with this reasoning, the range for the coefficient E_2 is defined as $[0.2-2.2]$.

This philosophy cannot be applied to determine the range of $\sigma_k = \sigma_l$, as this would result into negative values for the coefficients. This is caused by the large variation of the coefficient's value, i.e. 350% when comparing the two models. In addition, it seems implausible that there would be such a large variation with respect to the nominal value of the coefficient when considering a single model. Therefore, the range for the $\sigma_k = \sigma_l$ is defined as $[0.7-2.1]$, which is a range of $\pm 50\%$ of the coefficient's nominal value for the $k-l$ model.

We recognize that the current definition of the prior uncertainty ranges for the $k-l$ closure coefficients is crude. However, limited information on the tuning of these coefficients has led to this choice. Note also that a crude definition of the closure coefficients is common, e.g. Cheung et al.[2], who simply defined uncertainty ranges of ± 25 or 50%. However, it does hold an increased risk of ending up with truncated posterior distributions.

A prior uncertainty range for the closure coefficients of the $k-l$ turbulence model is given in Table 3.4.

Table 3.4: Summary of the ranges for the prior uniform distributions of the $k-l$ closure coefficients

Parameter	Lower	Upper
κ	0.3	0.5
$\sigma_k = \sigma_l$	0.7	2.1
B_1	15.0	21.0
E_2	0.2	2.2
c_μ	0.02	0.14

Chapter 4

Deterministic Simulations for Turbulent Flat Plate Flows

To be able to compare the uncertainty of the Spalart-Allmaras, Launder-Sharma's $k-\epsilon$ and Smith's $k-l$ turbulence model, we need to apply them to a couple of test cases. For this purpose, three turbulent flat plate flows have been selected. The main difference between them is that each are subject to a different pressure gradient[1], i.e.

- Wieghardt's zero pressure gradient case (zpg) [16];
- Ludwieg and Tillman's favourable pressure gradient case (fpg) [15];
- and Ludwieg and Tillman's adverse pressure gradient case (apg) [15].

For this chapter, the deterministic results of the three studied turbulence models have been compared for the zpg, fpg and apg flow case. The quantity of interest in this thesis is the friction coefficient C_f, usually defined as

$$C_f = \frac{\tau_w}{\frac{1}{2}\rho\bar{u}^2}, \tag{4.1}$$

in which τ_w represents the wall shear stress, ρ the local air density and $\bar{u}$ the local airspeed. However, the results as presented here are normalized using the velocity at the end of the plate.

$$C_f = \frac{\tau_w}{\frac{1}{2}\rho\bar{u}_e^2}. \tag{4.2}$$

[1]Note that the experimental data for the listed cases can be found in Appendix D.

4.1 Test Case 1: A Zero Pressure Gradient Turbulent Flat Plate Flow

This section dives deeper into the zero pressure gradient flow case of Wieghardt. In his experiment, the velocity of the flow was set to $u_\infty = 33[m/s]$ and remains approximately constant along the length of the plate. First, the used mesh and boundary conditions will be discussed. Consequently, the obtained results for Spalart-Allmaras, Launder-Sharma's $k-\epsilon$ and Smith's $k-l$ turbulence model are presented and compared.

The mesh layout for the zero pressure gradient case is represented in Figure 4.1. The mesh is constructed using Grid95 with settings as depicted in Table 4.1. One can see that at the start and close to the plate, the density of the grid cells increases.

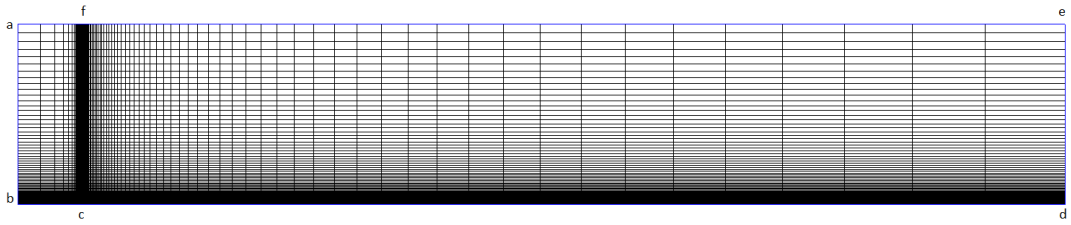

Figure 4.1: Mesh for the zero pressure gradients case.

Table 4.1: Mesh layout for the zero pressure gradient case

Boundary	Begin	End	Stretching Function	Coefficient	Grid gap
a - b	(-1.00, 3.00)	(-1.00, 0.00)	Geometric Progression	1.05	80
b - c	(-1.00, 0.00)	(0.00, 0.00)	Exponential Function	7.00	15
c - d	(0.00, 0.00)	(0.00, 16.50)	Exponential Function	8.00	95
d - e	(16.50, 0.00)	(16.50, 3.00)	Geometric Progression	1.05	80
e - f	(16.50, 3.00)	(0.00, 3.00)	Exponential Function	8.00	95
f - a	(0.00, 3.00)	(-1.00, 3.00)	Exponential Function	7.00	15

Figure 4.2 shows the deterministic results of the three models under investigation for the zero pressure gradient case. One can observer that there is quite some variance in the results. By using Bayesian calibration, this variance should be reduced.

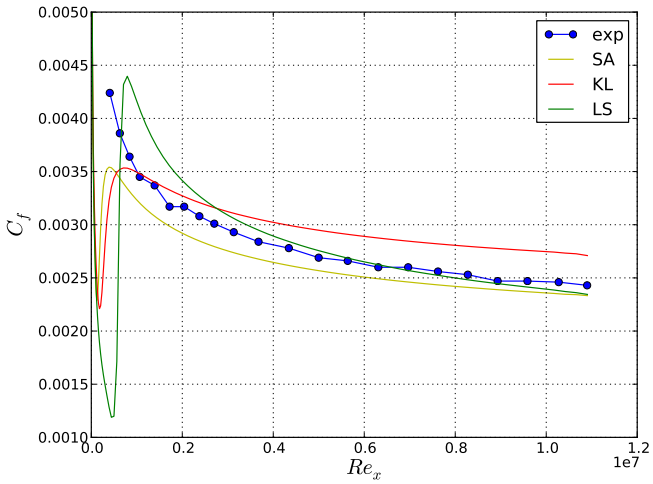

Figure 4.2: Friction coefficient comparison for the zero pressure gradients case.

4.2 Test Case 2: A Favourable Pressure Gradient Turbulent Flat Plate Flow

The second test case considers a turbulent flat plate flow subject to a favourable pressure gradient. As a result of the favourable pressure gradient, the flow will be accelerating along the length of the plate. At the start of the plate, the airspeed is approximately $u_\infty = 11.5[m/s]$. It increases to about $u_\infty = 27.5[m/s]$, which are still subsonic conditions. As a favourable pressure gradient is considered, we need to install a converging mesh and change our boundary conditions with respect to the zero pressure gradient case. How this is done will be discussed in the following section. After that, the results obtained by the Spalart-Allmaras and k-l model for the favourable pressure gradient case will be presented.

In order to simulate a favourable pressure gradient flow, we need to model a converging mesh as is shown in Figure 4.3. The rate of convergence is dependent on the steepness of the pressure gradient. The settings of the mesh for this flow case can be found in Table 4.2. While introducing the converging duct, it is important to keep the density of the grid cells high at the start and close to the plate. In addition, the grid cells should remain parallel for a sufficient distance lateral to the plate.

Figure 4.4 shows the deterministic results for the fpg case. One observes that there is quite some variance between te results again. Especially comparing the SA and KL model to the LS model. Towards the end of the plate, the SA and KL model's results do converge.

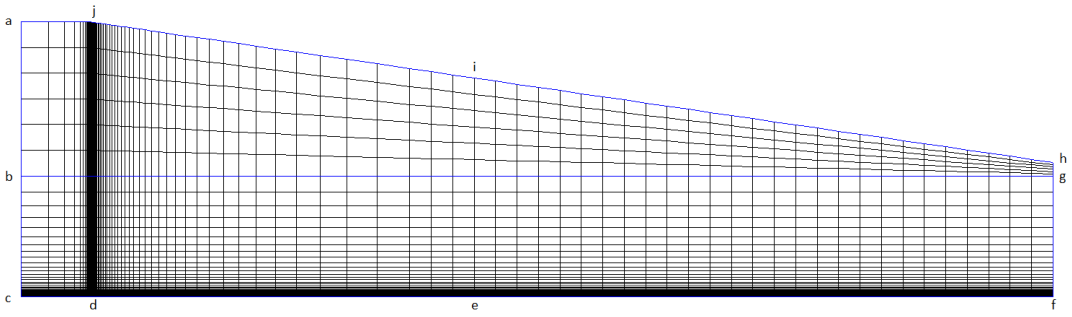

Figure 4.3: Mesh for the favourable pressure gradient case.

Table 4.2: Mesh layout for the favourable pressure gradient case

Boundary	Begin	End	Stretching Function	Coefficient	Grid gap
a - b	(-1.00, 4.10)	(-1.00, 1.80)	Geometric Progression	1.00	6
b - c	(-1.00, 1.80)	(-1.00, 0.00)	Geometric Progression	1.15	74
c - d	(-1.00, 0.00)	(0.00, 0.00)	Exponential Function	7.30	14
d - e	(0.00, 0.00)	(4.80, 0.00)	Exponential Function	7.30	66
e - f	(4.80, 0.00)	(14.4, 0.00)	Geometric Progression	1.00	30
f - g	(14.40, 0.00)	(14.4, 1.80)	Geometric Progression	1.15	74
g - h	(14.40, 1.80)	(14.40, 2.00)	Geometric Progression	1.00	6
h - i	(14.40, 2.00)	(4.80, 3.80)	Geometric Progression	1.00	30
i - j	(4.80, 3.80)	(0.00, 4.10)	Exponential Function	7.30	66
j - a	(0.00, 4.10)	(-1.0, 4.10)	Exponential Function	7.30	14

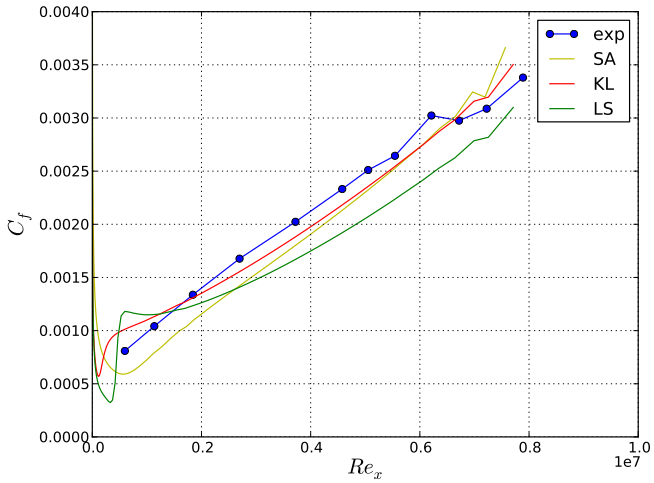

Figure 4.4: Friction coefficient comparison for the adverse pressure gradients case.

4.3 Test Case 3: An Adverse Pressure Gradient Turbulent Flat Plate Flow

Finally, the third test case considers a turbulent flat plate flow subject to an adverse pressure gradient. This is simulated by running the flow through a diverging channel, which results in a slowdown of the flow. The velocity at the beginning of the plate is about $u_\infty = 34[m/s]$, while $u_\infty = 23[m/s]$ at the end. The remaining part of this chapter presents the mesh, boundary conditions and results for the adverse pressure gradient case in a similar way as for the previous two cases.

To model the adverse pressure case, we need to construct a diverging mesh. They layout for this mesh is represented by Figure 4.5. More details can be found in Table 4.3. Similarly to what is been done for the zpg and fpg case, we also introduce more grid cells close to and at the start of the plate. We also keep the cells lateral to the plate for a sufficient upward distance.

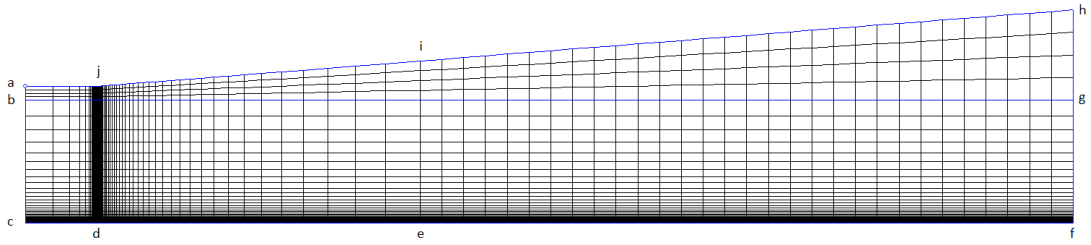

Figure 4.5: Mesh for the adverse pressure gradients case.

Table 4.3: Mesh layout for the adverse pressure gradient case

Boundary	Begin	End	Stretching Function	Coefficient	Grid gap
a - b	(-1.00, 2.00)	(-1.00, 1.80)	Geometric Progression	1.00	4
b - c	(-1.00, 1.80)	(-1.00, 0.00)	Geometric Progression	1.15	76
c - d	(-1.00, 0.00)	(0.00, 0.00)	Exponential Function	7.30	14
d - e	(0.00, 0.00)	(4.80, 0.00)	Exponential Function	7.30	66
e - f	(4.80, 0.00)	(14.40, 0.00)	Geometric Progression	1.00	30
f - g	(14.40, 0.00)	(14.40, 1.80)	Geometric Progression	1.15	76
g - h	(14.40, 1.80)	(14.40, 3.10)	Geometric Progression	1.00	4
h - i	(14.40, 3.10)	(4.80, 2.38)	Geometric Progression	1.00	30
i - j	(4.80, 2.38)	(0.00, 2.00)	Exponential Function	7.30	66
j - a	(0.00, 2.00)	(-1.00, 2.00)	Exponential Function	7.30	14

Figure 4.6 shows the deterministic results for the apg flow case. One observes that the results for the KL and SA model are similar, while there is a higher variance with the LS model.

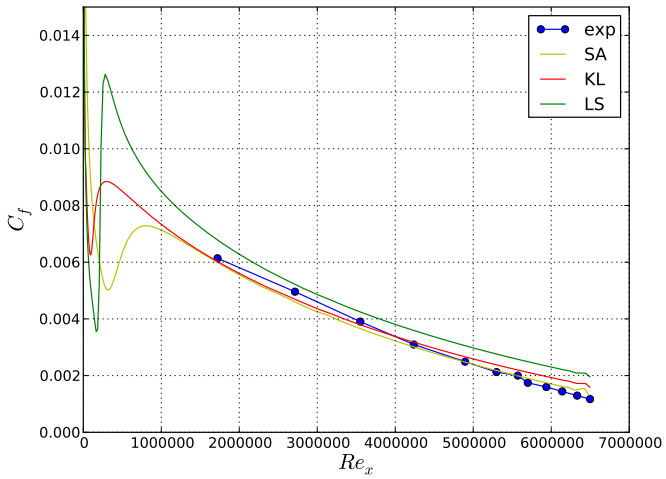

Figure 4.6: Friction coefficient comparison for the adverse pressure gradients case.

Overall it can be concluded that there is quite some variance present between the results of the of the different models for all flow cases. This variance between models should be reduced significantly after the application of Bayesian calibration. The Bayesian calibrated results are discussed in Chapter 6.

Chapter 5

The Creation of Surrogate Models using the Probabilistic Collocation Method

The next step is to propagate the uncertain parameters that are determined in Chapter 3 through the SA, KL and LS model for the three different test cases. In order to do that, we use the probabilistic collocation method to create surrogate models. The creation of a total of nine (3 models $\times$ 3 test cases) is being covered in this chapter.

5.1 Surrogates for the SA Model

In order to create a surrogate model for the SA, KL and LS RANS models, we use the Probabilistic Collocation method. Section 2.2.1 explains the theory behind this method. The first step in the Probabilistic Collocation method is obtaining the collocation points at which the deterministic solutions have to be obtained. To determine these collocation points, we first need to estimate the polynomial order for each uncertainty parameter until we get an amount that suffices to obtain quality surrogate models.

Section 3.2.2 describes the SA model's uncertainty parameters and their intervals. Now we need to determine the polynomial order for each single one of them. In order to do this, five deterministic simulations for each uncertainty parameter are performed while only varying the value of the uncertainty parameter within the predetermined intervals; every other parameter, including boundary conditions are kept equal.

The resulting graphs for the SA model's uncertainty parameters are displayed in Figure 5.1. In these graphs, the friction coefficient C_f is plotted against each uncertainty parameter of the SA model. The order of these polynomials can now be determined from these figures. Table 5.1 summarizes the polynomial orders for each uncertainty parameter. The number of collocation points then becomes $(3+1)^2 \times (2+1)^3 = 432$. For each of these collocation

points, we run a deterministic simulation. The results of these then serve as the basis of the surrogate model.

The polynomial order for each uncertainty parameter is not the only conclusion that can be obtained from the graphs displayed in Figure 5.1. By looking at the variation of the QoI within the predetermined interval of the uncertainty parameters, we can conclude which ones are most influential. As such, it can be concluded that for the SA model the QoI is most dependent on the values of the viscous coefficient c_{v1} and the Von Kármán coefficient κ.

For the LS and KL model, the same procedure is being followed. Note that for the SA model, it was repeated for the zpg, fpg, and apg case. However, the results were the same for each flow case. Therefore, for the other models this exercise was done for just one of the flow cases.

The graphs for the uncertainty parameters of these models are depicted in Figures 5.2 and 5.3. In case of the LS model we end up with a total of 192 collocation points, while for the KL model it adds up to 180 collocation points. For the LS model, just as for the SA model, it can be concluded that two uncertainty parameters are much more influential on the solution than the others, i.e. the Von Kármán coefficient κ and the ratio of P/ϵ. For the KL model, these are the parameters E_2 and the Von Kármán coefficient κ.

Performing such a huge amount of simulations makes it seem as if the Probabilistic Collocation method is computationally expensive. In a certain way it is of course, as the number of deterministic simulations that have to be run to generate a surrogate model increases rapidly with the number of uncertainty parameters. However, by looking at the sensitivity of the model to the chosen uncertainty parameters, a number of them can be eliminated without significant effect, as they have little influence on the results of the simulation. The amount of required deterministic simulations will consequently decrease, resulting in less computational time. However, in the present investigation the non-influential uncertainty parameters are included as to prove this point.

SA Model	Poly. Order	LS Model	Poly. Order	KL Model	Poly. Order
κ	2	n	2	κ	2
σ	3	C_μ	3	$\sigma_k = \sigma_l$	2
c_{w2}	2	P/ϵ	3	B_1	1
c_{w3}	3	κ	3	E_2	4
c_{v1}	2	σ_k	0	c_μ	1

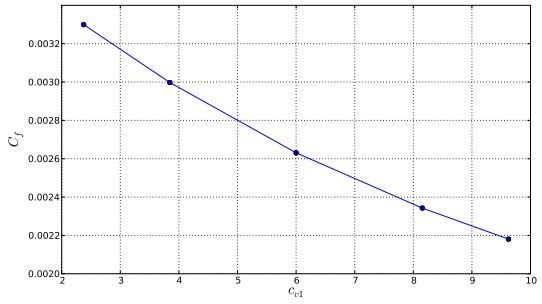

(a)

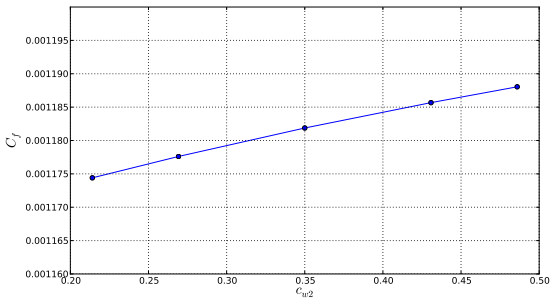

(b)

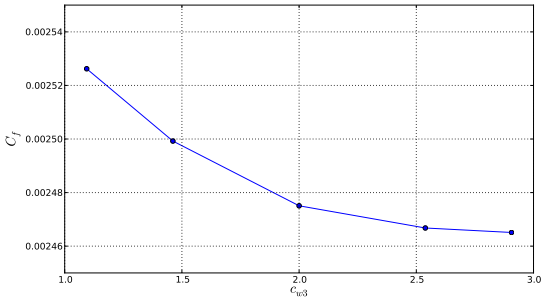

(c)

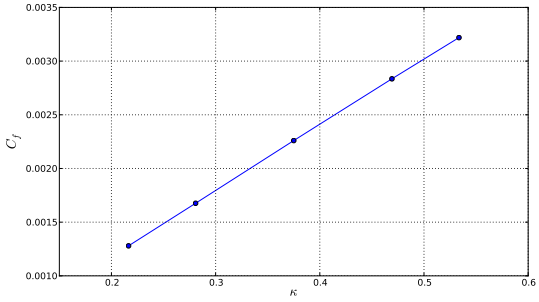

(d)

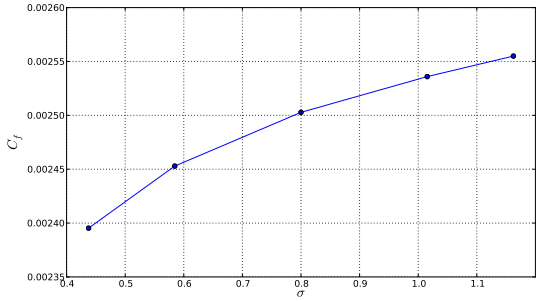

(e)

Figure 5.1: These five figures show the evolution of the friction coefficient with a single varying closure coefficient - keeping all else equal - for the SA model.

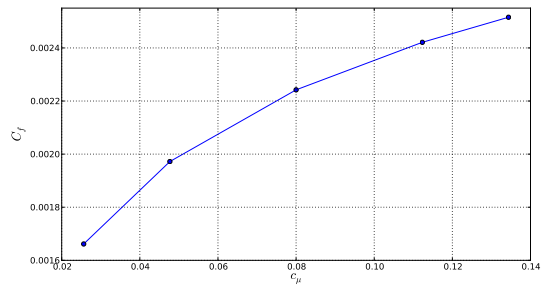

(a)

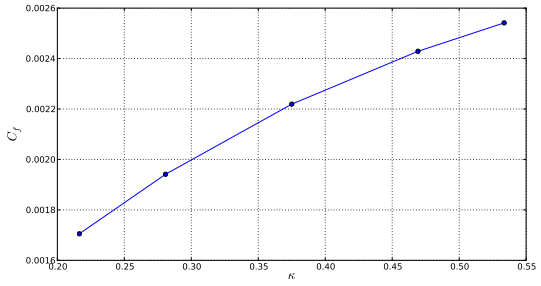

(b)

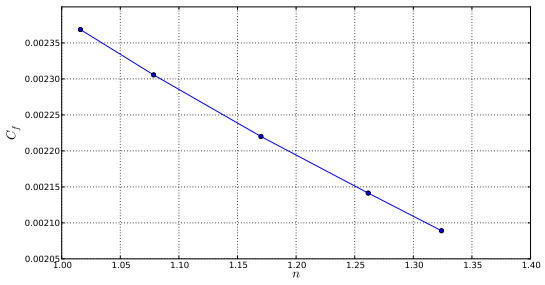

(c)

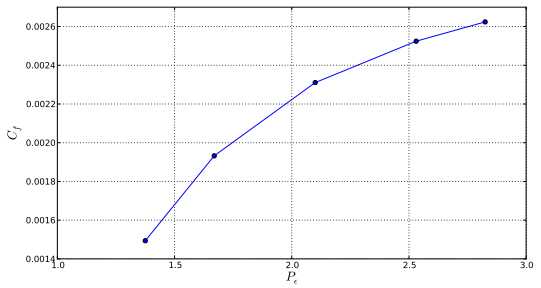

(d)

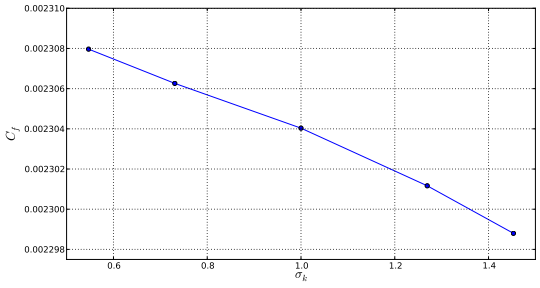

(e)

Figure 5.2: These five figures show the evolution of the friction coefficient with a single varying closure coefficient - keeping all else equal - for the LS model.

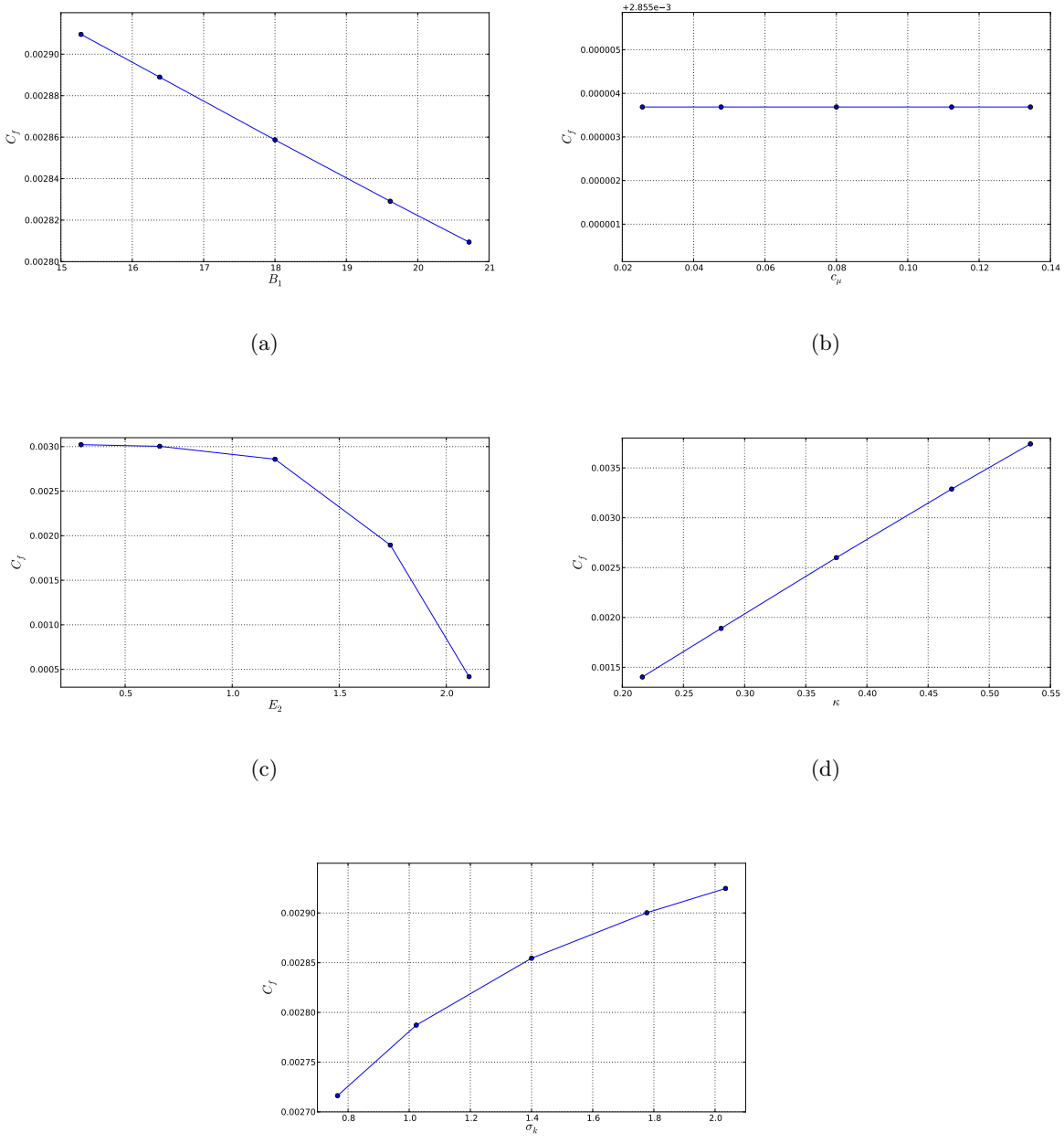

Figure 5.3: These five figures show the evolution of the friction coefficient with a single varying closure coefficient - keeping all else equal - for the KL model.

5.2 An Accuracy Check of the Surrogate Models

To check the accuracy of the surrogate models with respect to the simulation code, we perform two types of comparisons:

1. A comparison of the surrogate model's and simulation code's results at a single x-location while varying the two most influential uncertainty parameters;
2. A comparison of the surrogate model's and simulation code's results along the entire length of the flat plate using the uncertainty parameter's values at the boundaries of the predetermined intervals.

These checks are done for every model and every use case.

Figure 5.4 shows the comparison of type 1 for the SA model zpg case. Figure (a) shows the results for the simulation code, while Figure (b) shows the results for the surrogate model. They are constructed by running the simulation code and surrogate model 64 times at 64 different combinations of the two depicted uncertainty parameters, i.e. κ and c_{v1} in this case. The coloured lines on the planes of the graphs show the 2-dimensional relationship between the uncertainty parameters and the friction coefficient and their mutual relationship. Figure (c) finally shows the relative error of the surrogate model as compared to the simulation code. This error is calculated using Equation 5.1.

$$RelativeError[\%] = \frac{C_{fsimulation} - C_{fsurrogate}}{C_{fsurrogate}} \times 100 \tag{5.1}$$

One can see that for the SA model zpg case, the results of the simulation code and the surrogate model look similar in shape. This is also shown by the calculated relative error, which doesn't exceed 2% at any point of the uncertainty parameter envelope. The largest error is observed at the smallest values for κ and c_{v1}.

Figure 5.5 shows the comparison of type 1 for the SA model fpg case. For the SA model fpg case, again one can see that the similar results are obtained from the simulation code and the surrogate model. However, this time there is a significant relative error between the two. For a large part of the uncertainty parameter envelope, a relative error of -7% is present, with peaks to more than -10%. Furthermore, the graph depicts that for a combination of low κ and high c_{v1} values, the error becomes positive, reaching a peak of 5%.

Figure 5.6 shows the comparison of type 1 for the SA model apg case. When comparing graphs (a) and (b) of the SA model apg case, they look similar in shape. Graph (c) however, shows a relative error ranging between 7-9% for the majority of the envelope, with a peak to 10%. Finally, when comparing the proximity of the lines in the 2-dimensional planes, it can be concluded that the Von Kármán constant κ is the most influential uncertainty parameter for all three pressure gradient cases. This can also be seen when comparing graph (a) and (d) of Figure 5.1. Nevertheless, the difference of influence is much more pronounced in the zpg and apg case. It is unknown why this is the case.

Figure 5.7 shows the comparison of type 2 for the SA model. Graphs (a) and (b) show the results of the SA zpg case. In graph (a), the red dotted lines show the results obtained by the simulation code, while the blue dash-dotted line shows the results obtained by the surrogate model. One can conclude that for the default and lower end values of the uncertainty parameters, the relative error converges quickly to a small value. For the upper end of the uncertainty parameter envelope, it takes longer. Nevertheless, towards the end of the plate it becomes similar in absolute terms to the error at the lower end of the envelope.

Graphs (c) and (d) show the results of the SA fpg case. Looking at the error for the default and lower end values of the uncertainty parameters, a similar conclusion as for the SA zpg case can be made. They converge quickly to a small error. For the upper end of the uncertainty parameter envelope, this is not at all the case. Rather large errors ranging between $\pm 10\%$ occur.

Finally, for the SA apg case, we observe the opposite. Graph (e) shows that at the lower end of the uncertainty parameter envelope the solution obtained by the surrogate model is rather unstable. As a result, there is a large fluctuation in its relative error. Now, for the default and upper end uncertainty parameter values, the relative error converges to a small value quickly. Nevertheless, for the upper boundary, the error increases again to a value of about 10%.

Figure 5.8 shows the comparison of type 1 for the LS model zpg case. Although at first sight the shapes of graphs (a) and (b) look similar, there are notable differences when you take a closer look. This becomes especially obvious when comparing the 2-dimensional planes to each other. While the friction coefficient C_f plunges abruptly around $P_\epsilon = 1.6$, there is a smoother transition taking place with the surrogate model. This results in a large relative error for values of $P_\epsilon < 1.6$. For larger values of P_ϵ the error remains close to zero.

Figure 5.9 shows the comparison of type 1 for the LS model fpg case. In the LS fpg case, graphs (a) and (b) are very similar to the LS zpg case. Again, for values of $P_\epsilon < 1.6$, very large relative errors are observed. This means that if we would obtain small values for P_ϵ after Bayesian calibration, the result should be considered untrustworthy.

Figure 5.10 shows the comparison of type 1 for the LS model apg case. Graphs (a) and (b) for the LS apg case seem to have a very different shape from the ones that are generated for the zpg and fpg case. That should not be the case as the same LS model was used for all three cases and the mathematical relations therefore stay the same. In fact, when you have a closer look, they are not that different. The only difference is that there is no plunge for the two graphs at value of $P_\epsilon < 1.6$. Without the plunge, the relative error for the LS apg case is also limited between $\pm 6\%$.

Figure 5.11 shows the comparison of type 2 for the LS model. Note that for the LS model, the relative error for at the upper and lower end of the uncertainty parameter envelope is perfectly zero. That is because we cheated a bit. For the SA model the real default, lower and upper boundary values were simulated. In the LS model case we used the simulations for the collocation points that matched closest the default, lower and upper boundaries in order to save simulation time. After applying our interpolation technique, this causes an exact

match for the simulation and surrogate model results in case the upper and lower end values are used. However, for the default values this is not the case. Except towards the end of the plate for the apg case, graph (f), a large relative error occurs when the default values are used. Also for graph (e), showcasing the LS apg case, an instability can be observed towards the end of the plate when using the lower end of the uncertainty parameter envelope.

Figure 5.12 shows the comparison of type 1 for the KL model zpg case. The simulation code's results show similar behaviour to what is observed for the LS model's zpg and fpg case. Here, there is an abrupt dent in the results at a value of $\kappa > 0.50$, especially when combined with high values of E_2. This then becomes apparent in graph (c), showing a large relative error when $\kappa > 0.50$ and growing for increasing E_2. The exact same conclusions can be drawn from **Figure 5.13, which shows the comparison of type 1 for the KL model fpg case.** However, note that the peak relative error is still much smaller compared to the zpg case, i.e. 150% vs. 600%.

Figure 5.14 shows the comparison of type 1 for the KL model apg case. The KL model's apg case shows similar behaviour as the zpg and fpg case, however, the large error is postponed for larger values of E_2. It can be concluded that if after calibration we're obtaining large values of κ and E_2, the results should be considered unreliable.

Figure 5.15 shows the comparison of type 2 for the KL model. For the KL model, the same "trick" is applied as for the LS case to save simulation time. One can observe that the simulation code and surrogate results almost match exactly. Although there is a rather large oscillation when the default values are used, the error quickly turns to practically zero as well, which was notably not the case for the LS model.

Overall it can be concluded that there is room for improvement when creating the surrogate models. The sometimes large errors that occur should be eliminated as much as possible. It is not completely clear whether these large errors are the result of a combination of values for the uncertainty parameters that turn the model unstable. However, as these errors usually occur at the boundaries of the envelope, this is expected to be the main cause.

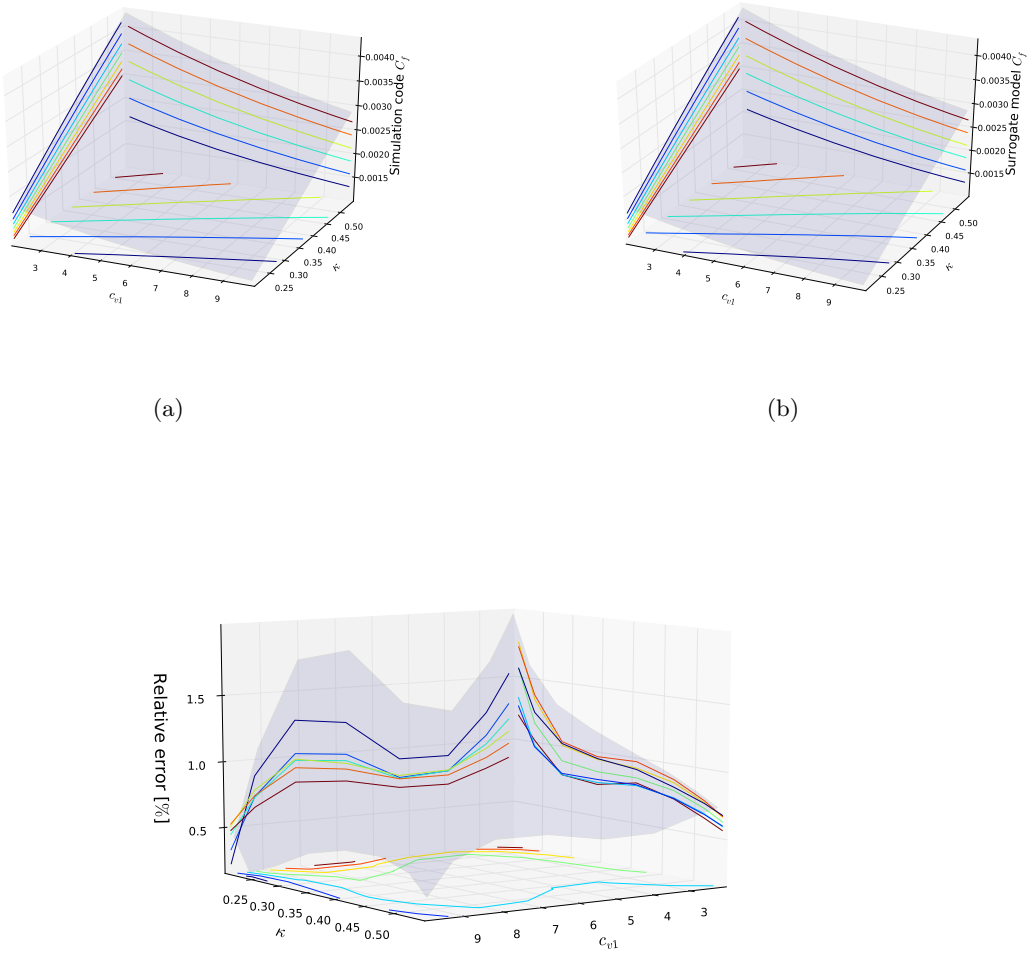

(a)

(b)

(c)

Figure 5.4: These three figures show the evolution of the friction coefficient at a single location on the flat plate for two varying closure coefficients. These are results for the zpg case using the SA model. Figure (a) shows the results from the simulation code, Figure (b) shows the results from the surrogate model for the same simulation conditions and finally Figure (c) shows the error between the two results.

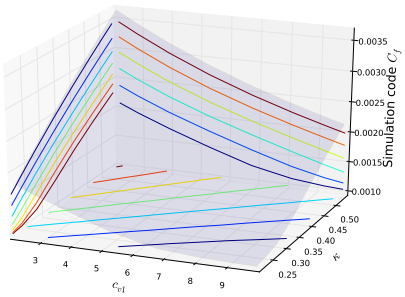

(a)

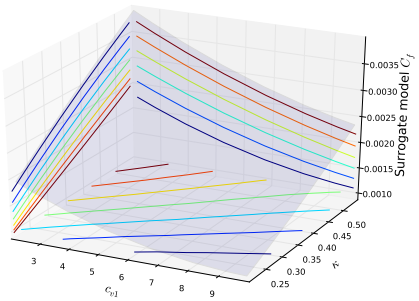

(b)

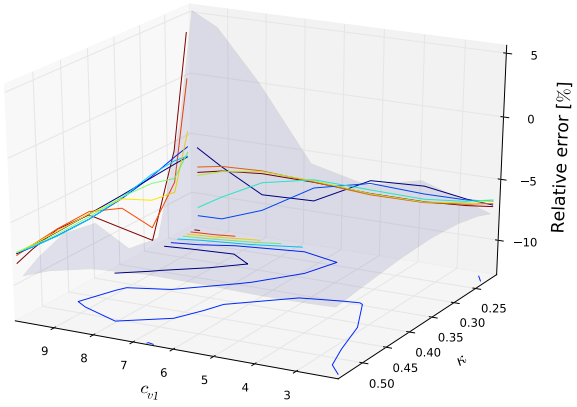

(c)

Figure 5.5: These three figures show the evolution of the friction coefficient at a single location on the flat plate for two varying closure coefficients. These are results for the fpg case using the SA model. Figure (a) shows the results from the simulation code, Figure (b) shows the results from the surrogate model for the same simulation conditions and finally Figure (c) shows the error between the two results.

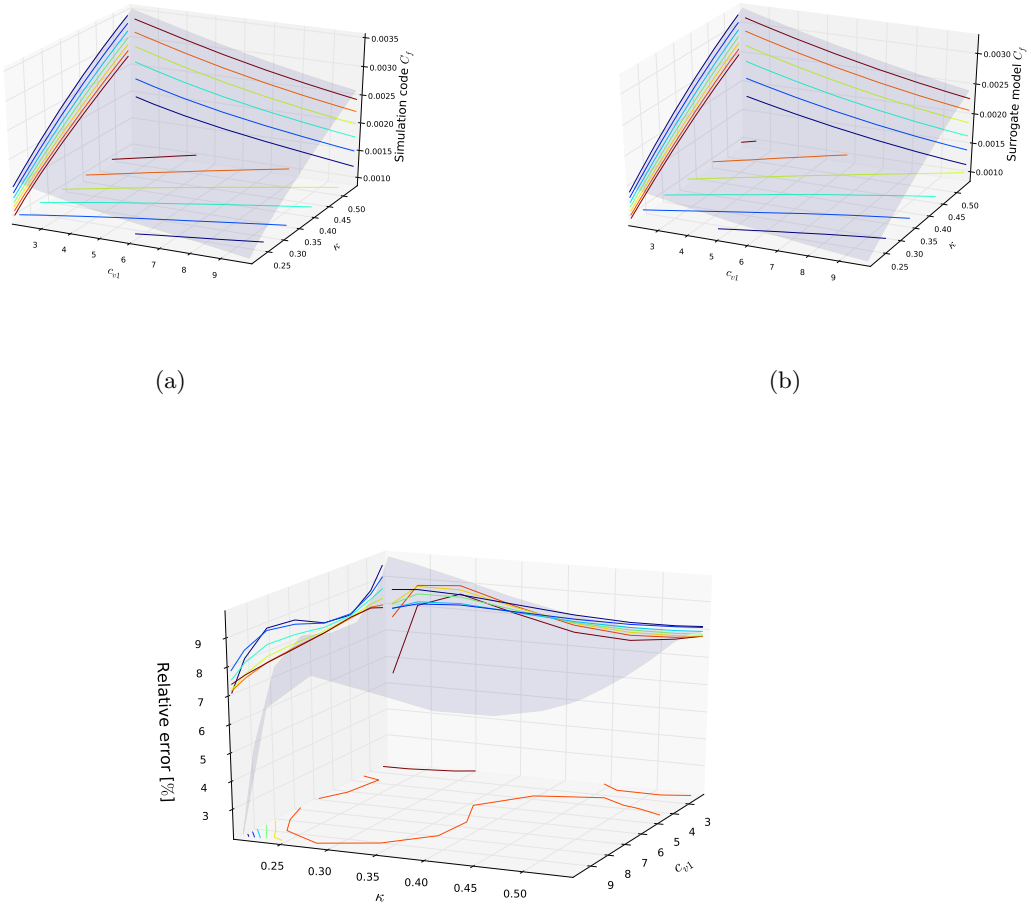

(a)

(b)

(c)

Figure 5.6: These three figures show the evolution of the friction coefficient at a single location on the flat plate for two varying closure coefficients. These are results for the apg case using the SA model. Figure (a) shows the results from the simulation code, Figure (b) shows the results from the surrogate model for the same simulation conditions and finally Figure (c) shows the error between the two results.

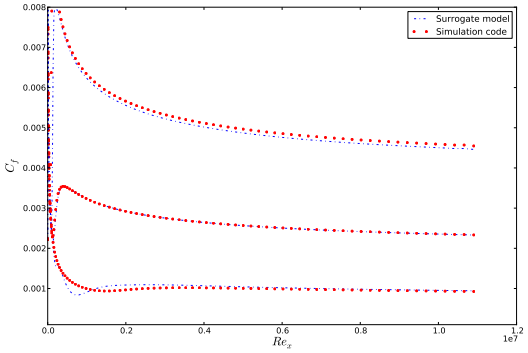

(a)

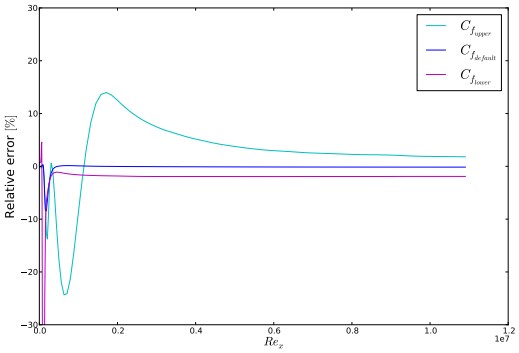

(b)

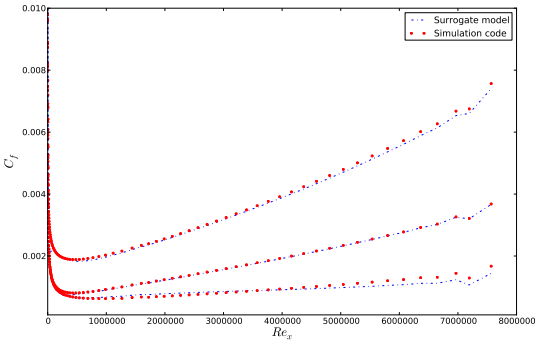

(c)

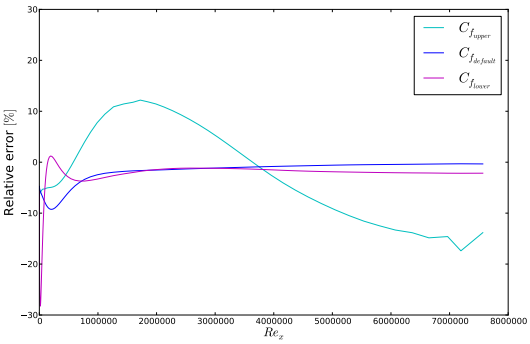

(d)

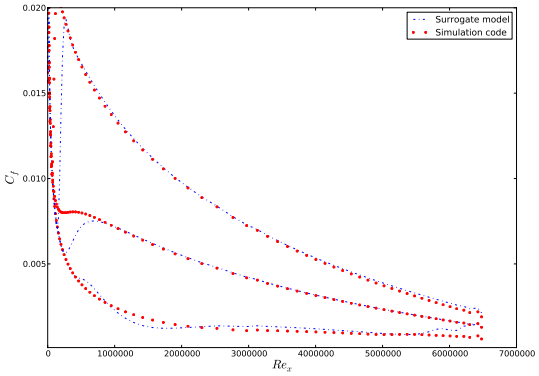

(e)

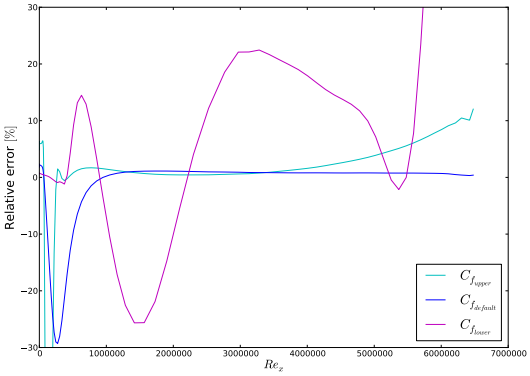

(f)

Figure 5.7: These six figures show the results for the zpg, fpg and apg case using the SA model and its surrogate model, as well as an error measurement at the outer edges of the closure coefficient's uncertainty intervals.

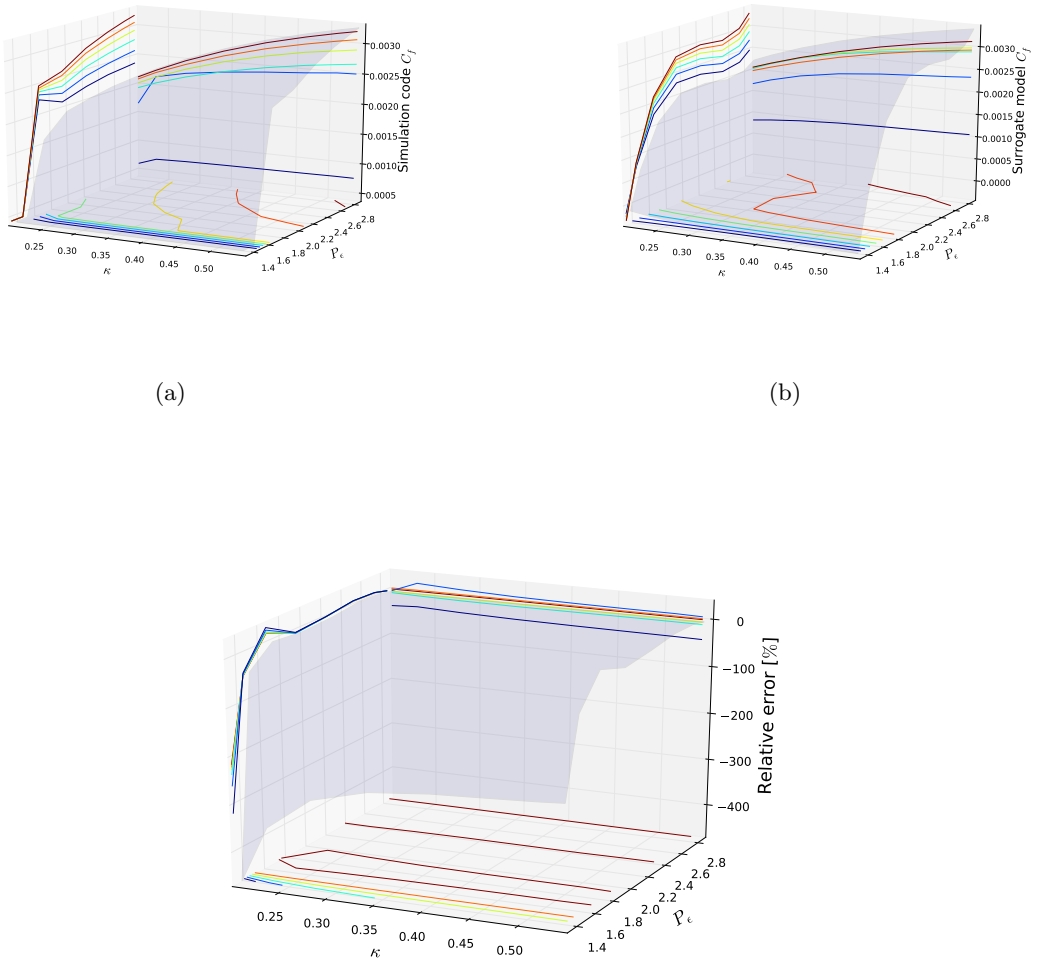

(a) (b)

(c)

Figure 5.8: These three figures show the evolution of the friction coefficient at a single location on the flat plate for two varying closure coefficients. These are results for the zpg case using the LS model. Figure (a) shows the results from the simulation code, Figure (b) shows the results from the surrogate model for the same simulation conditions and finally Figure (c) shows the error between the two results.

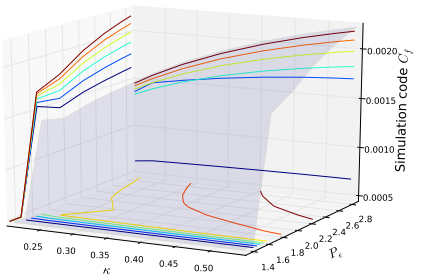

(a)

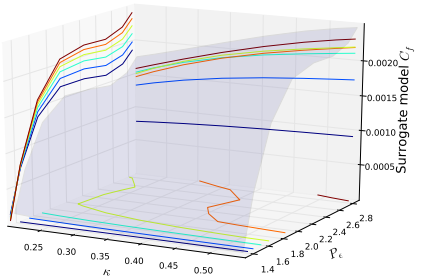

(b)

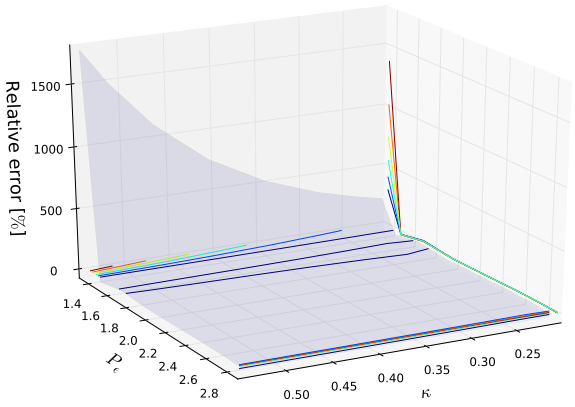

(c)

Figure 5.9: These three figures show the evolution of the friction coefficient at a single location on the flat plate for two varying closure coefficients. These are results for the fpg case using the LS model. Figure (a) shows the results from the simulation code, Figure (b) shows the results from the surrogate model for the same simulation conditions and finally Figure (c) shows the error between the two results.

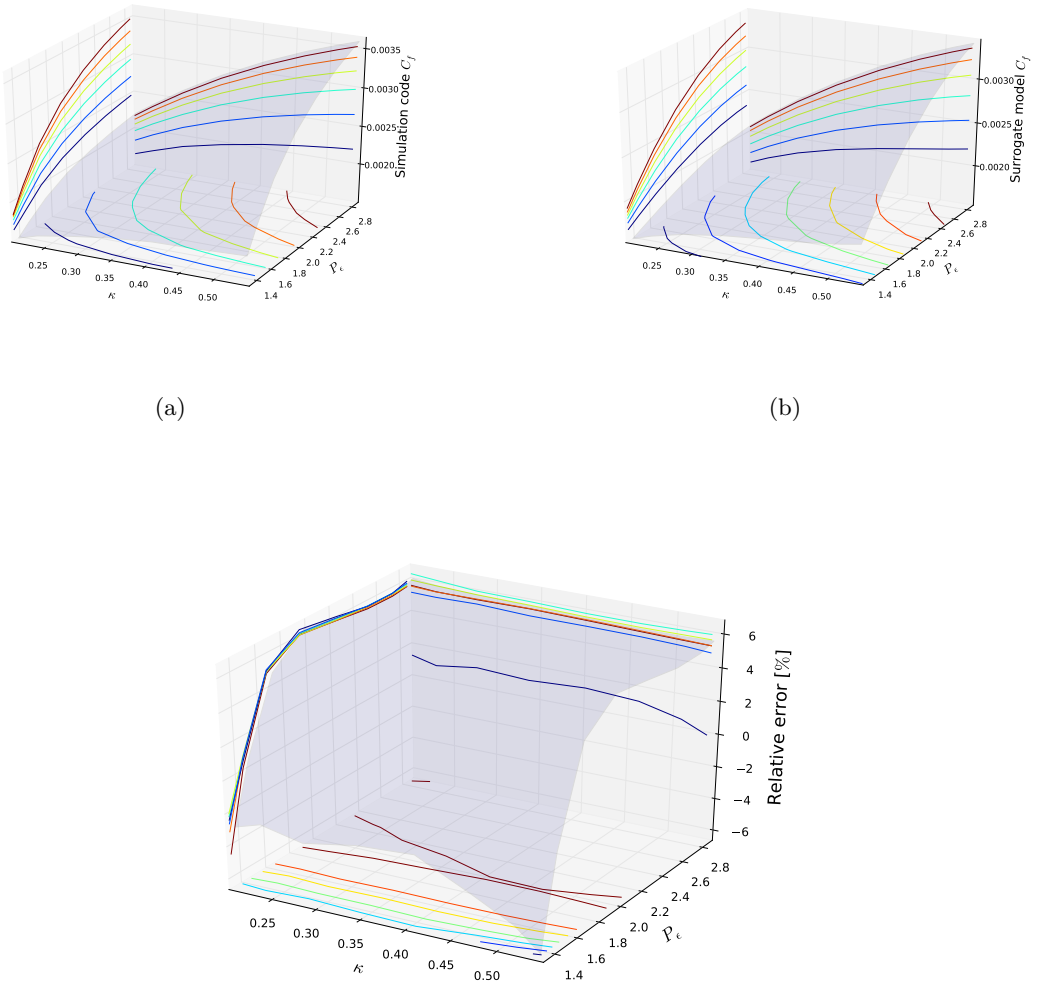

(a)

(b)

(c)

Figure 5.10: These three figures show the evolution of the friction coefficient at a single location on the flat plate for two varying closure coefficients. These are results for the apg case using the LS model. Figure (a) shows the results from the simulation code, Figure (b) shows the results from the surrogate model for the same simulation conditions and finally Figure (c) shows the error between the two results.

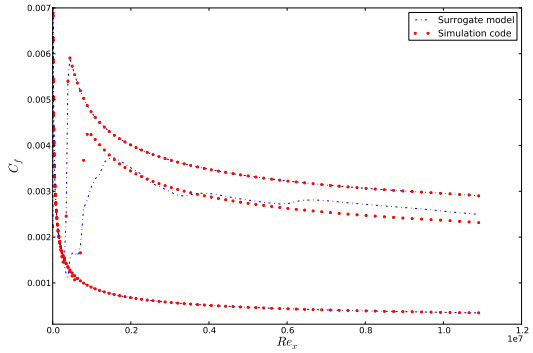

(a)

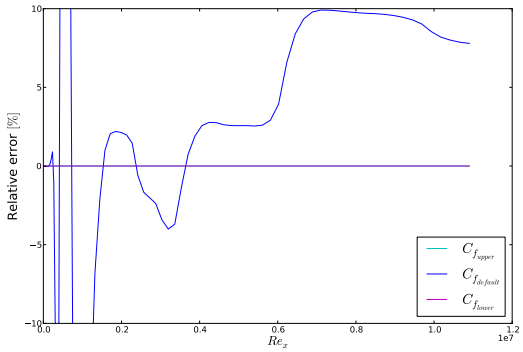

(b)

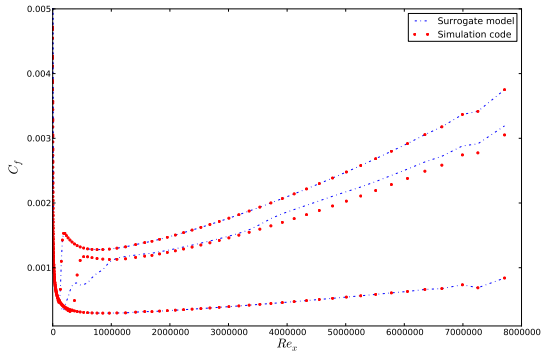

(c)

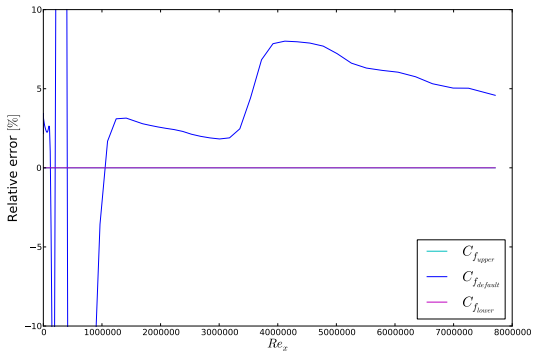

(d)

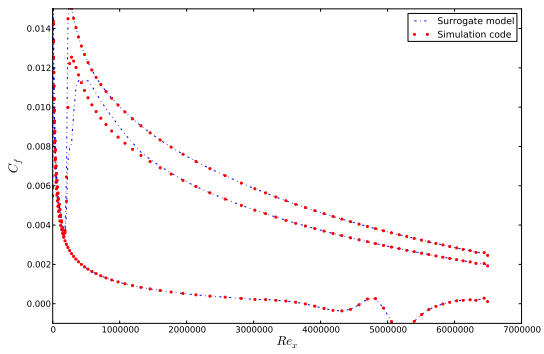

(e)

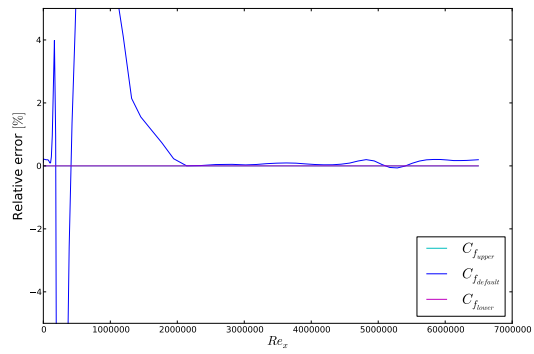

(f)

Figure 5.11: These six figures show the results for the zpg, fpg and apg case using the LS model and its surrogate model, as well as an error measurement at the outer edges of the closure coefficient's uncertainty intervals.

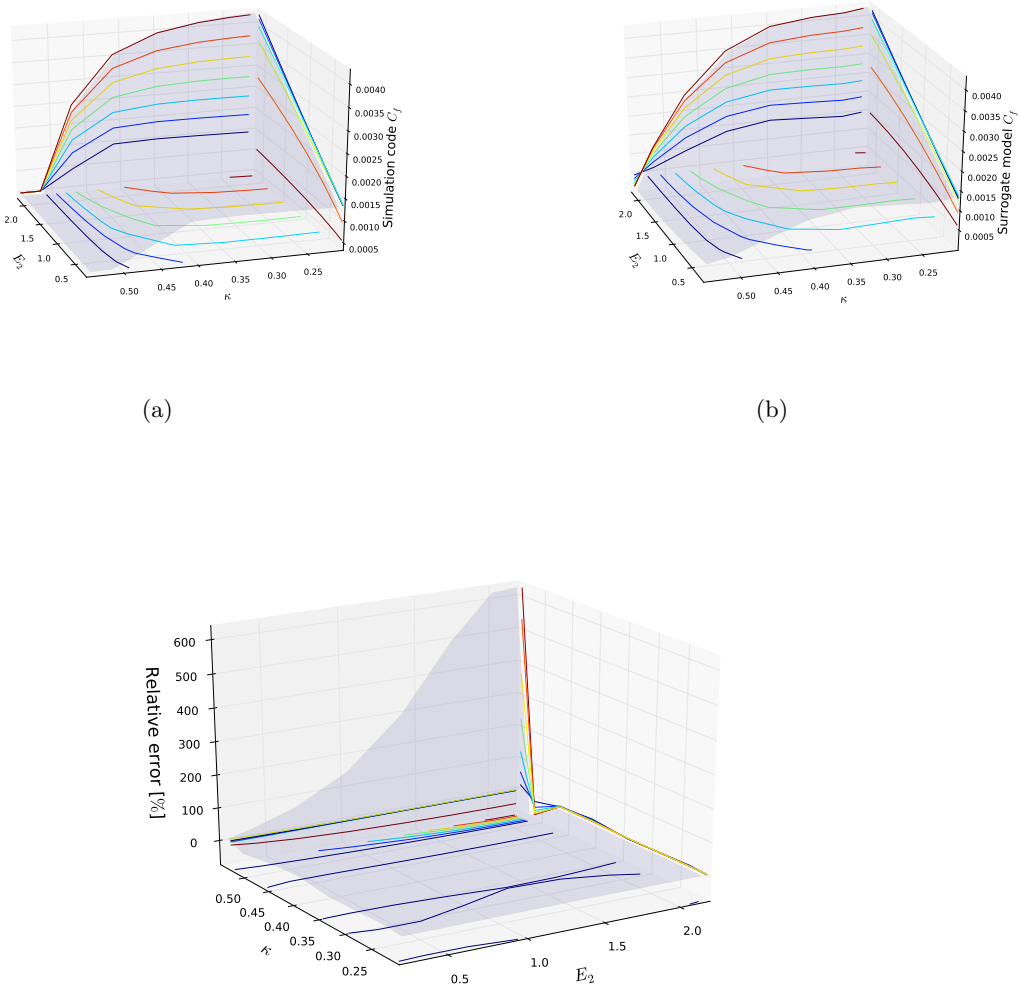

(a)

(b)

(c)

Figure 5.12: These three figures show the evolution of the friction coefficient at a single location on the flat plate for two varying closure coefficients. These are results for the zpg case using the KL model. Figure (a) shows the results from the simulation code, Figure (b) shows the results from the surrogate model for the same simulation conditions and finally Figure (c) shows the error between the two results.

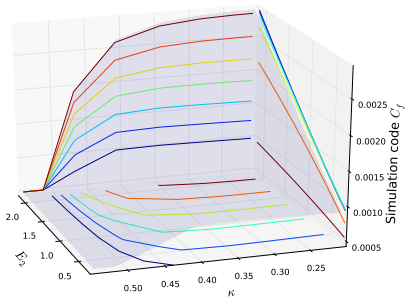

(a)

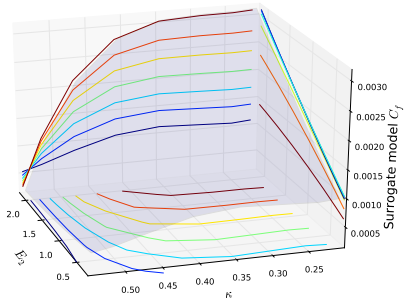

(b)

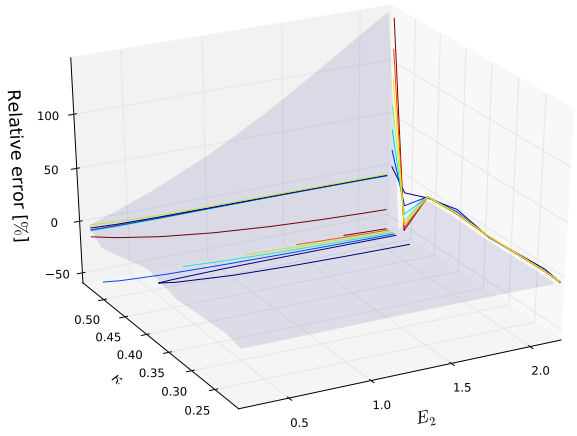

(c)

Figure 5.13: These three figures show the evolution of the friction coefficient at a single location on the flat plate for two varying closure coefficients. These are results for the fpg case using the KL model. Figure (a) shows the results from the simulation code, Figure (b) shows the results from the surrogate model for the same simulation conditions and finally Figure (c) shows the error between the two results.

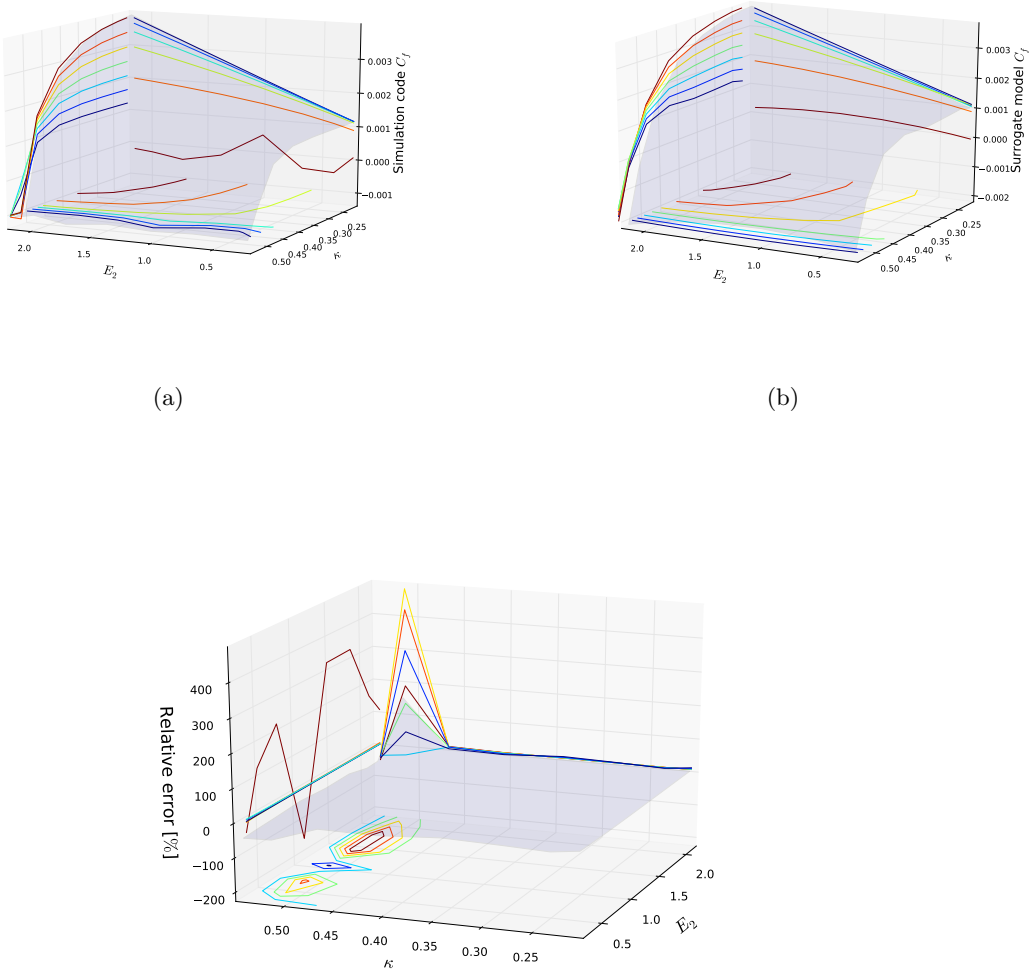

(a)

(b)

(c)

Figure 5.14: These three figures show the evolution of the friction coefficient at a single location on the flat plate for two varying closure coefficients. These are results for the apg case using the KL model. Figure (a) shows the results from the simulation code, Figure (b) shows the results from the surrogate model for the same simulation conditions and finally Figure (c) shows the error between the two results.

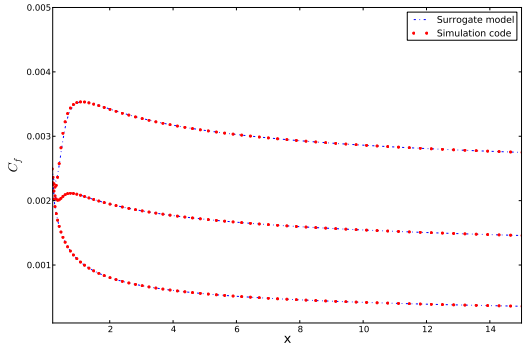

(a)

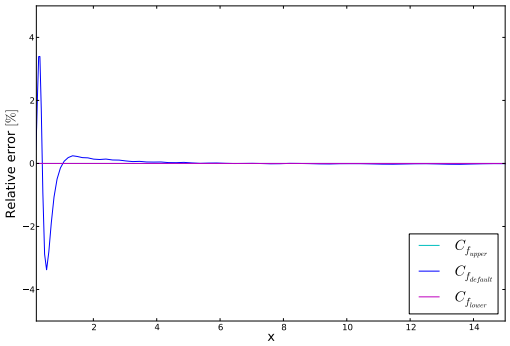

(b)

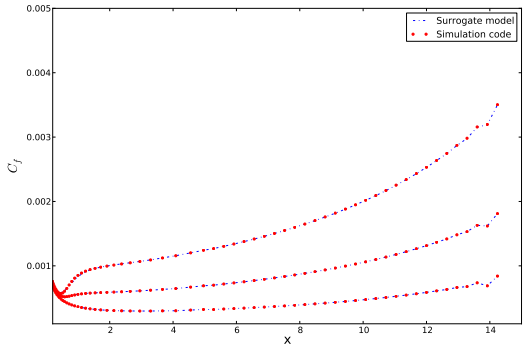

(c)

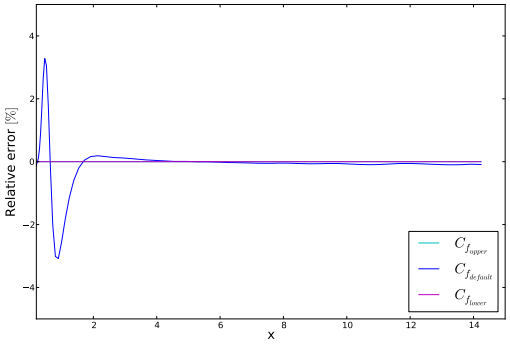

(d)

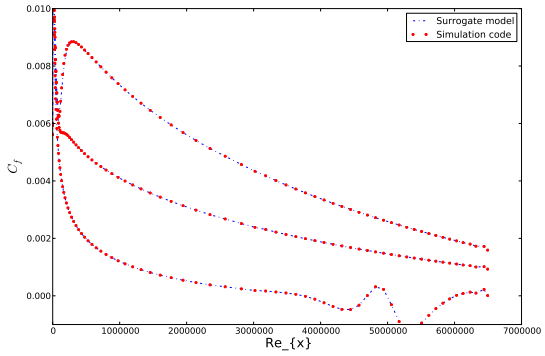

(e)

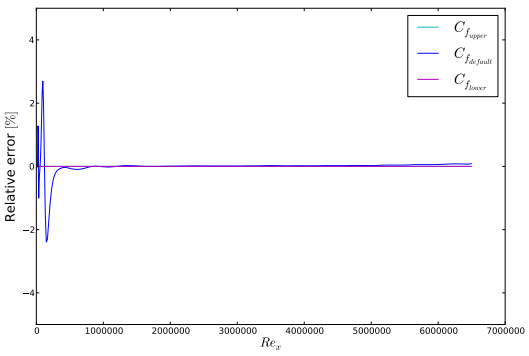

(f)

Figure 5.15: These six figures show the results for the zpg, fpg and apg case using the KL model and its surrogate model, as well as an error measurement at the outer edges of the closure coefficient's uncertainty intervals.

Chapter 6

Bayesian Calibrated Uncertainty Parameters

This chapter discusses the results of the Bayesian calibration for the SA and KL model. Unfortunately the Bayesian calibration for the Launder-Sharma model did not work. Why that is the case is unclear, as the process that was followed was exactly the same as for the two other models. The results for the SA and KL model proved to be successful as you will see later on in this chapter.

When looking at Figures 6.1, 6.3 and 6.5, it can be concluded that for the SA model the Von Kármán coefficient κ and the viscous coefficient c_{v1} are well-informed by the experimental data. Unsurprisingly, these are also the two coefficients to which the SA model is most sensitive as is shown in Chapter 5. For the other coefficients, c_{w2}, c_{w3} and σ, no clear conclusion on their posterior probability can be drawn as they are not sufficiently informed by the experimental data. The exception is the apg flow case however, where a tendency does seem to appear for the 3rd and 4th most sensitive coefficients c_{w3} and σ.

The most probable value for the Von Kármán coefficient in the zpg case lies a bit below 0.36. For the fpg case the value gets closer to 0.24, and in the apg case it's slightly higher than 0.30. This shows that the Von Kármán coefficient is flowcase dependent. In addition, for non of the cases it reaches a value which is close to its default value of 0.41.

When looking at the viscous coefficient c_{v1}, the value for the zpg case is around 4.5. In the fpg case, it moves to the lower edge of the uncertainty interval that was determined in Chapter 3, i.e. 2.0. The same, but less outspoken, happens in the apg case. It can be concluded therefore that it would have been better to increase the uncertainty parameter range to a lower boundary than 2.0. Secondly, the uncertainty parameter is dependent on the flowcase, similarly to what was observed with the Von Kármán parameter. Finally, also the most probable values of the viscous coefficient doesn't get close to its default value of 7.1.

In the SA model apg case, also coefficients c_{w3} and σ are informed to some extent. Although the results are not as clear as for the κ and c_{v1} coefficients, a tendency can be observed

towards slightly higher values of c_{w3} and slightly lower values of σ.

Similar conclusions can be drawn for the KL model, represented in Figures 6.7, 6.9 and 6.11. The two most influential coefficients, E_2 and κ, are also the ones that are well-informed by the data. For the other coefficients, no clear conclusion can be drawn, except that B_1 seems to have a tendency to the lower bounds of the uncertainty interval for the zpg and apg case.

In the KL model zpg case, the most probable value for coefficient E_2 is slightly above 0.24. For the fpg case, the value of E_2 seems to have two preferred values. One is close to $E_2 = 1.2$, but a higher probability is achieved at a value close to $E_2 = 0.4$. The reason for this bimodel distribution is unclear. Finally for the apg case, the most probable value for E_2 is close to 1.56. As was the case for the SA model, again a high dependency is observed between the posterior probability distribution of the closure coefficient and the flowcase. This proves that choosing a default value of $E_2 = 1.2$ is rather crude.

For the KL model Von Kármán coefficient, one observes that the highest probability is where it obtains a value between $\kappa = 0.3 - 0.38$ in the zpg case, $\kappa = 0.41 - 0.45$ in the fpg case and $\kappa = 0.48 - 0.55$ in the apg case. For the apg case, the probability density function is truncated at the higher end of the interval. Hence, it would be better to choose an even larger uncertainty interval. Again the coefficient proves to be flowcase dependent. In addition, the Von Kármán coefficient is model dependent, as for the KL model it obtains totally different values than for the SA model.

Figures 6.2, 6.4, 6.6, 6.8, 6.10 and 6.12 display the friction coefficient resulting after Bayesian calibration of the uncertainty parameters. The red dots show the experimental data, with an added experimental uncertainty indicated by the error bars. The dashed blue line shows the mean value (μ) for the friction coefficient $\pm$ one standard deviation σ. The blue line shows the mean value $\pm$ three standard deviations. Note that the friction coefficient given in the histograms is basically a "cross-section" at a single location of the plate, while these figures show the evolution along the entire length of the plate.

Generally we observe that the uncertainty of the results is reduced at places where the density of the experimental data is highest. In addition, when the experimental uncertainty is lower, this also improves the uncertainty of the simulation results. This can be seen by comparing the calibrated results for the apg cases to the results of the zpg and fpg case. For the apg cases, the experimental uncertainty of the data is chosen to be lower as can be seen from the red "error" bars. This reduces the uncertainty which is apparent by $\mu \pm \sigma$ and $\mu \pm 3\sigma$ lines lying closer to each other.

The Bayesian calibrated results also prove to be much more accurate than the deterministic results obtained using the default closure coefficients. The variance between the different model's results has also reduced as predicted in Chapter 4.

The above discussion leads to the overall conclusion that closure coefficients are both flow case as well as model (in case of the Von Kármán coefficient) dependent. Choosing a constant value for these parameters, as is regular practice when using RANS simulations, is therefore a rather inadequate approach.

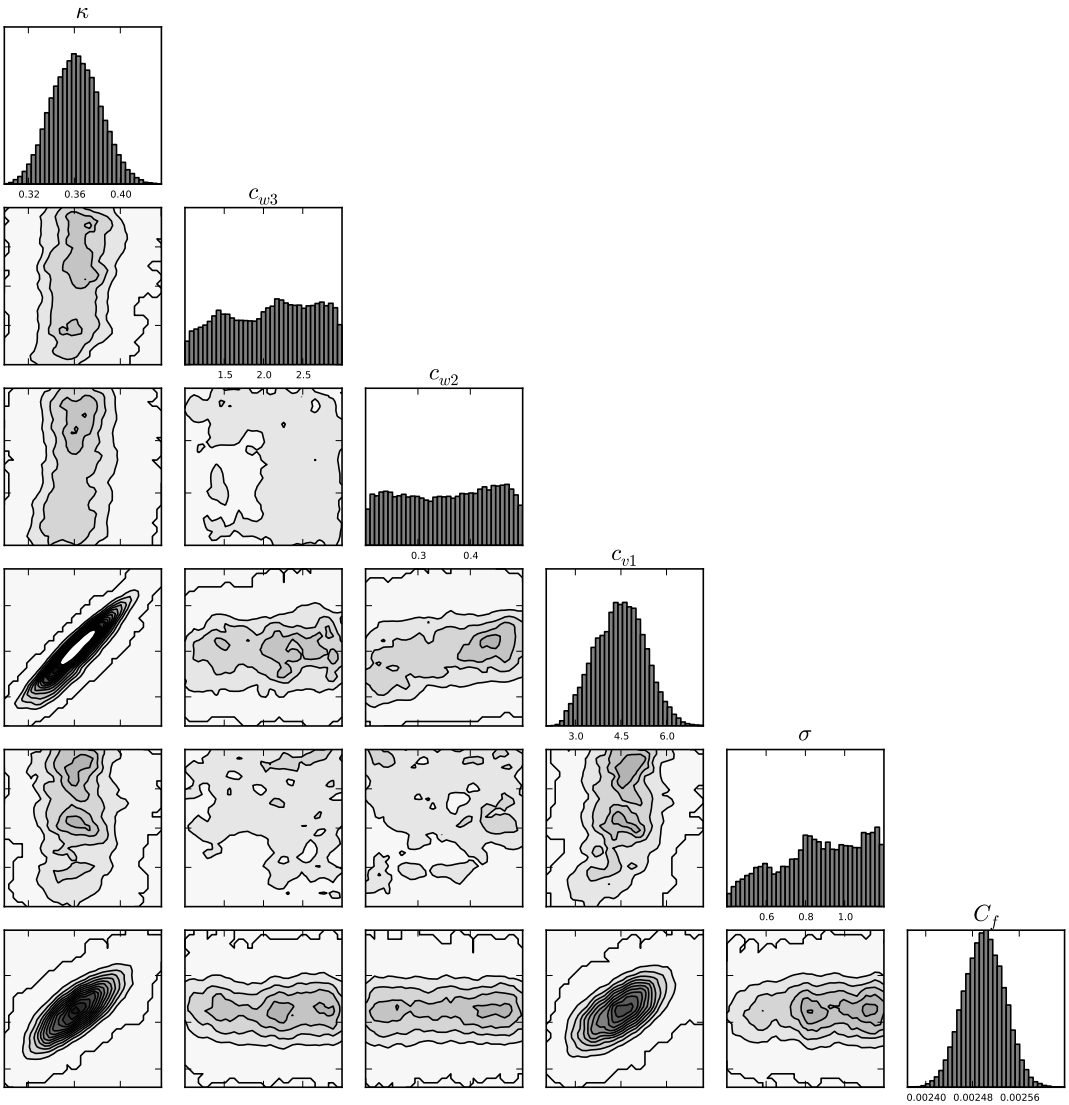

Figure 6.1: Histogram for the SA model zpg case after Bayesian calibration.

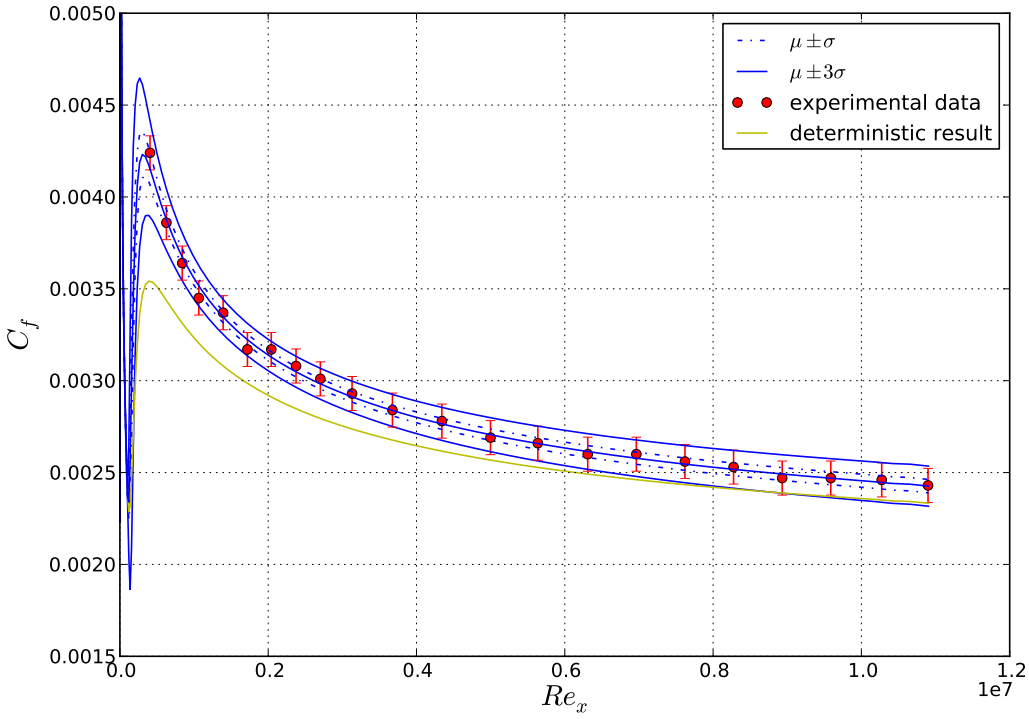

Figure 6.2: Friction coefficient along a flat plate for the SA model zpg case after Bayesian calibration.

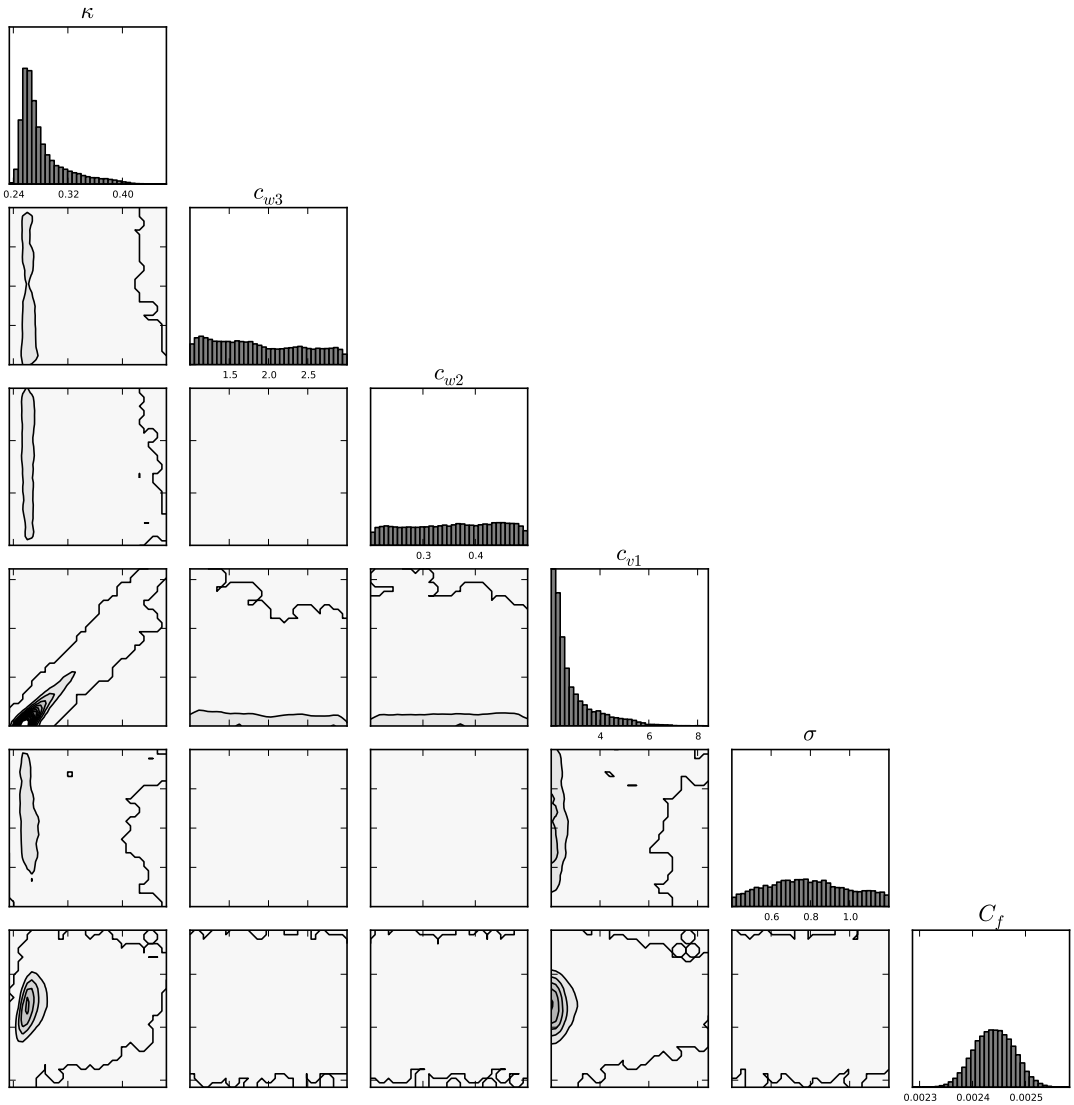

Figure 6.3: Histogram for the SA model fpg case after Bayesian calibration.

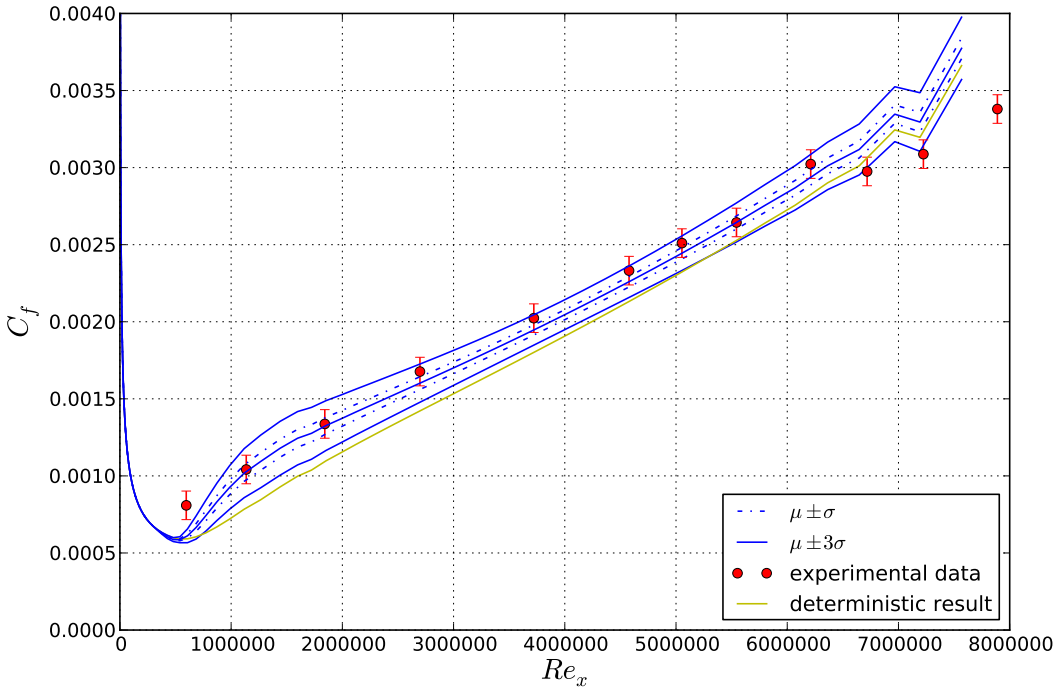

Figure 6.4: Friction coefficient along a flat plate for the SA model fpg case after Bayesian calibration.

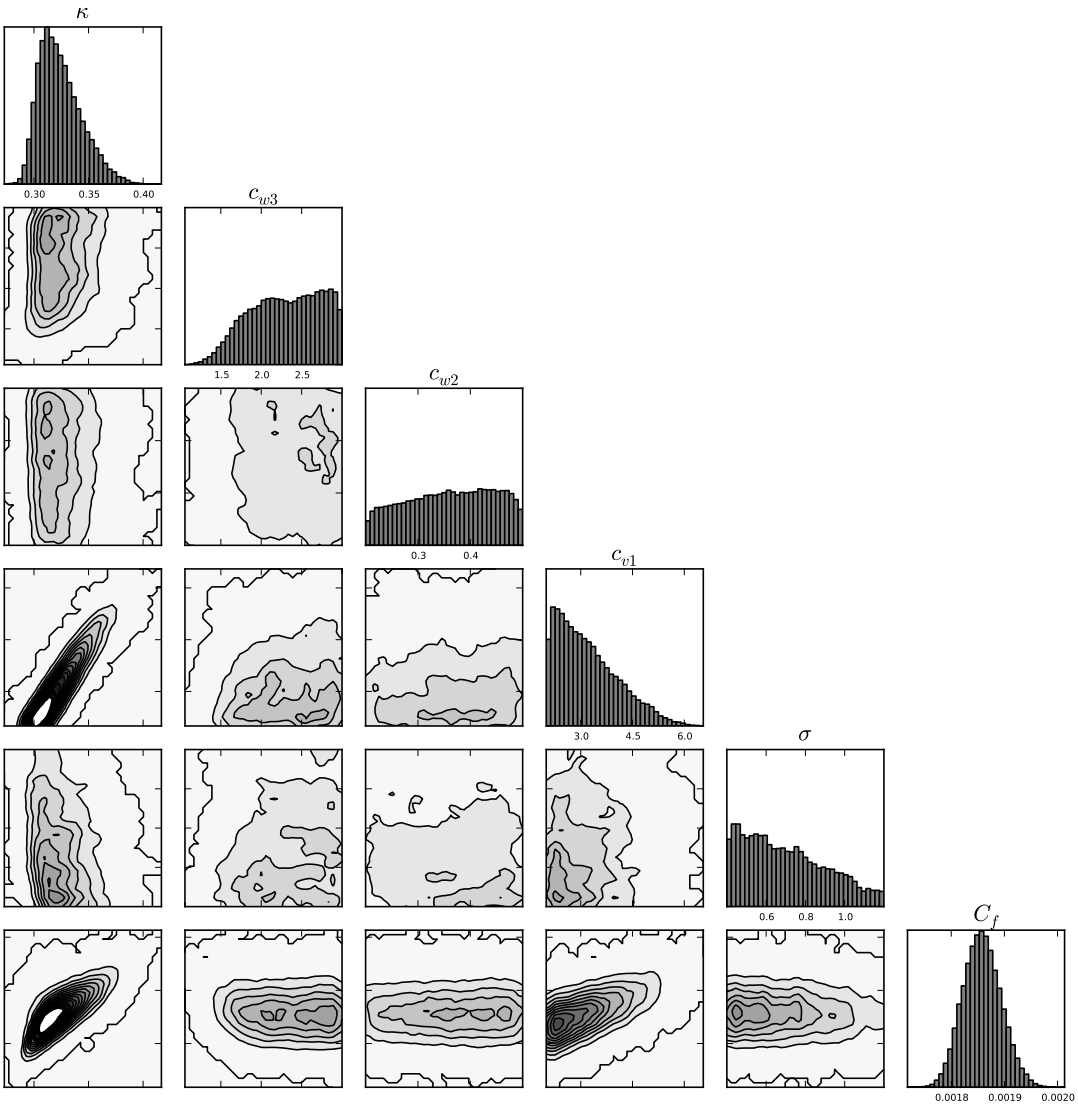

Figure 6.5: Histogram for the SA model apg case after Bayesian calibration.

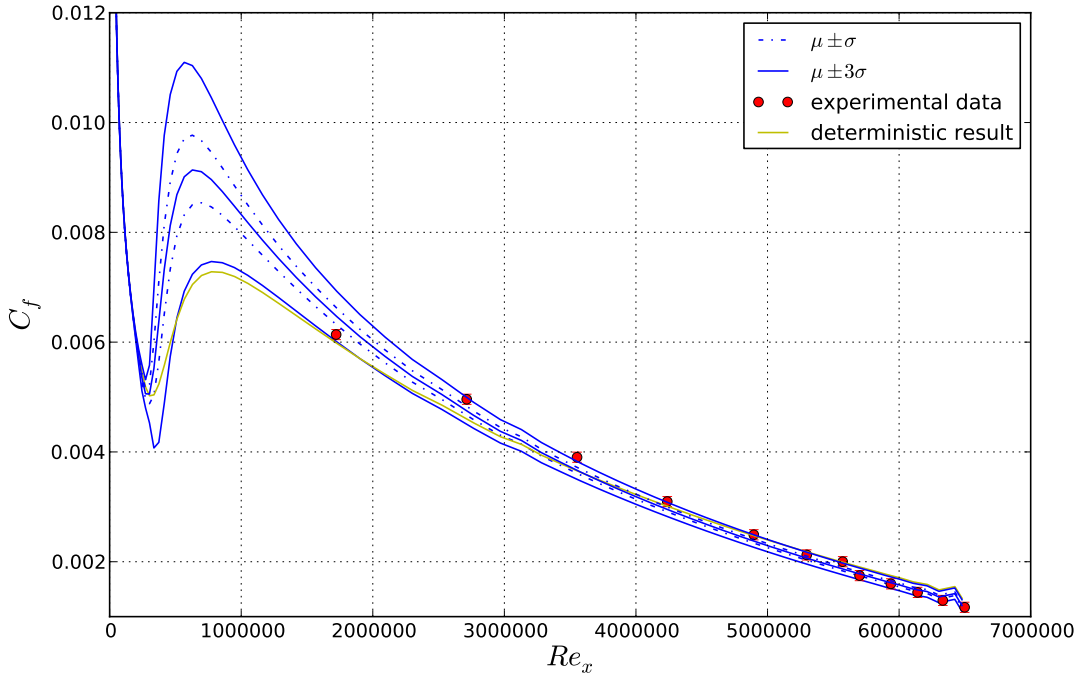

Figure 6.6: Friction coefficient along a flat plate for the SA model apg case after Bayesian calibration.

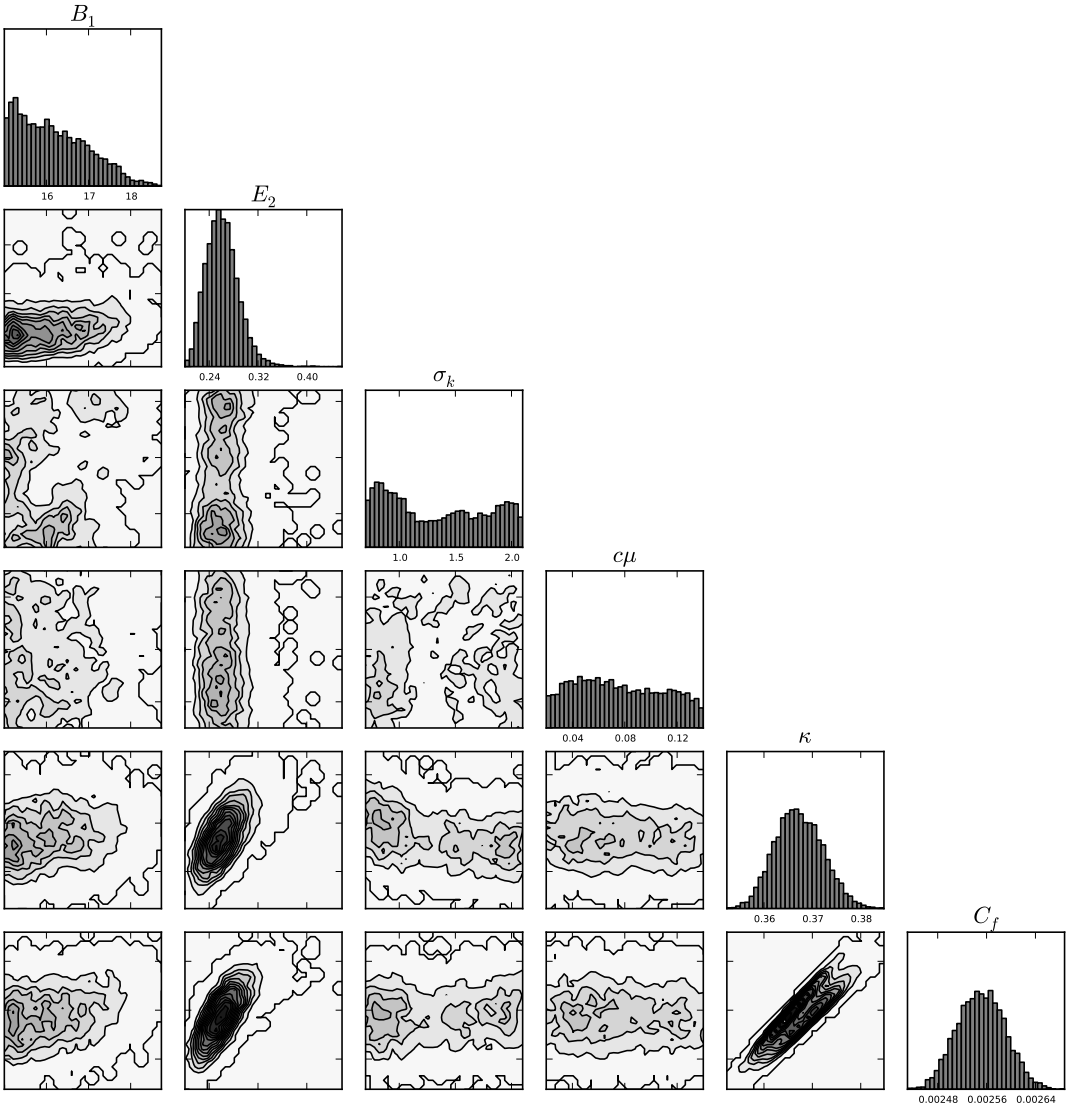

Figure 6.7: Histogram for the KL model zpg case after Bayesian calibration.

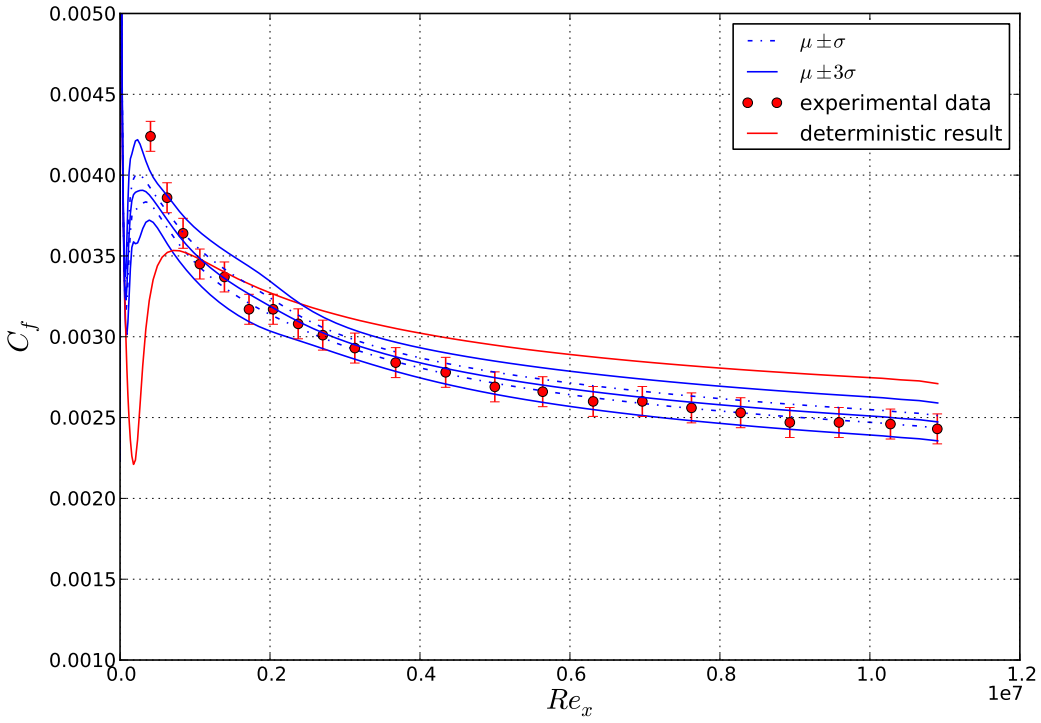

Figure 6.8: Friction coefficient along a flat plate for the KL model zpg case after Bayesian calibration.

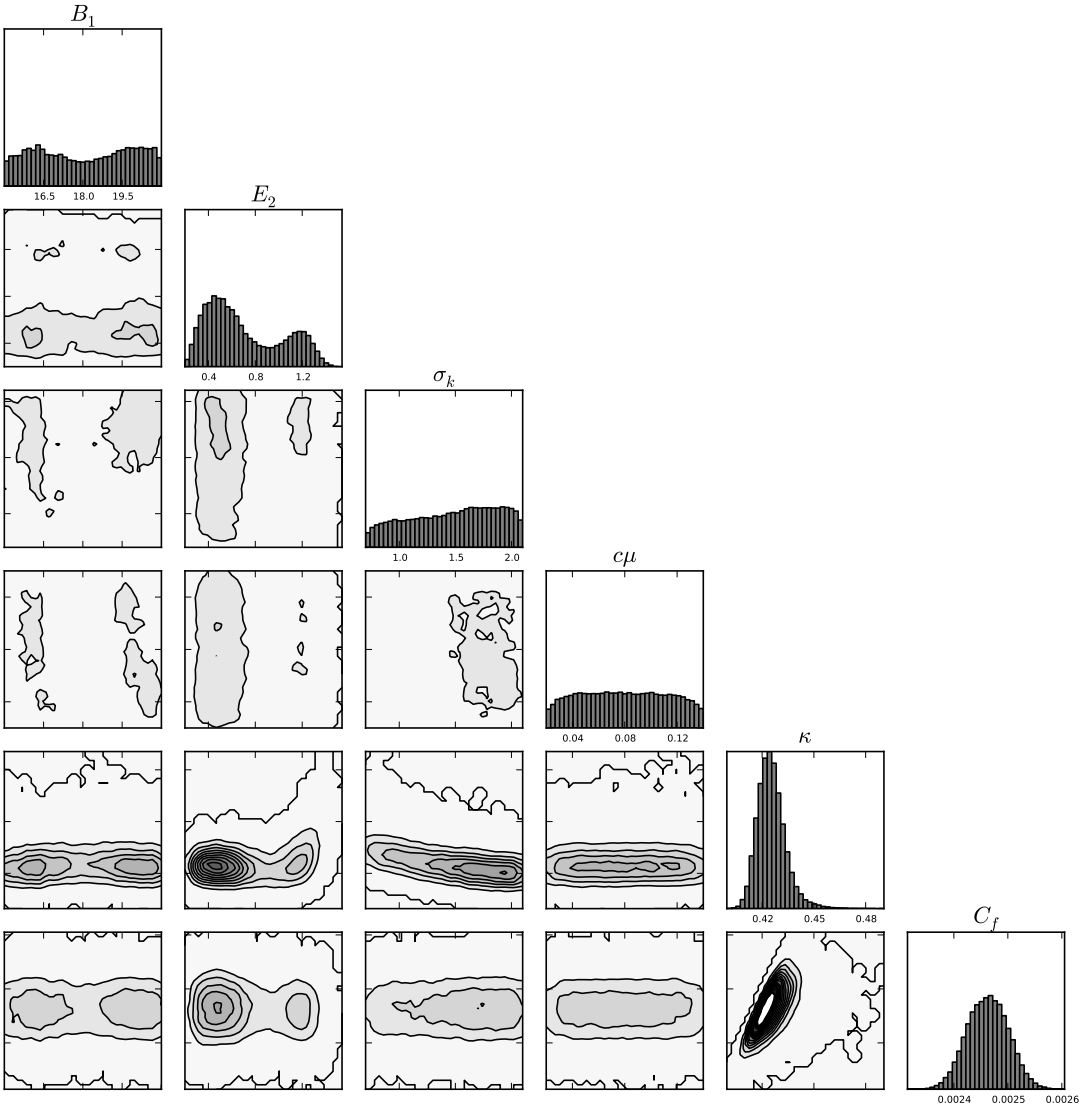

Figure 6.9: Histogram for the KL model fpg case after Bayesian calibration.

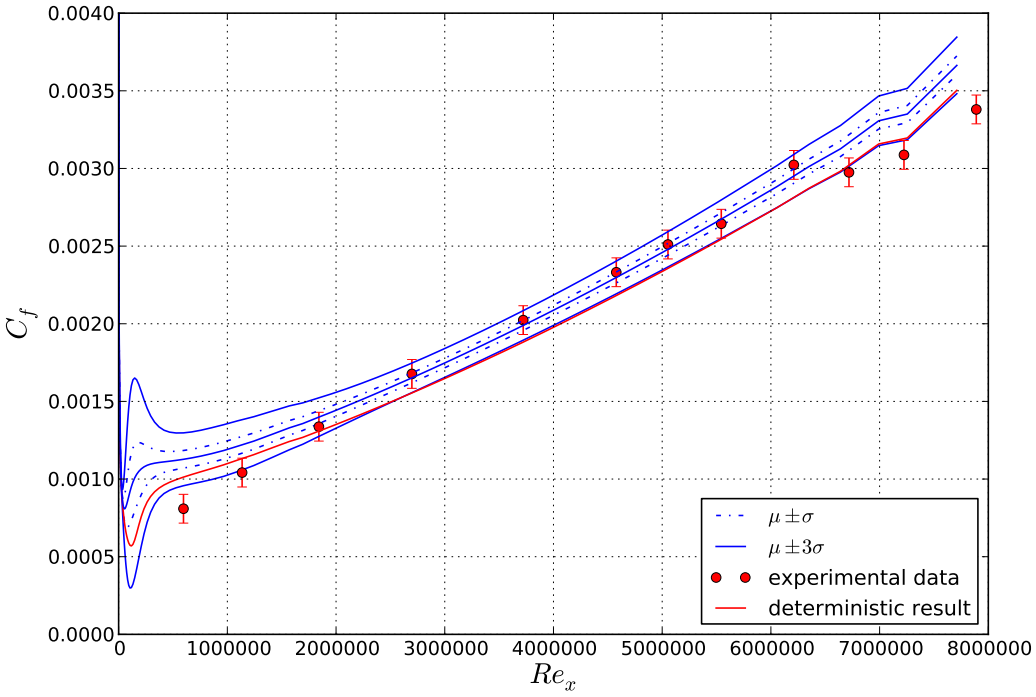

Figure 6.10: Friction coefficient along a flat plate for the KL model fpg case after Bayesian calibration.

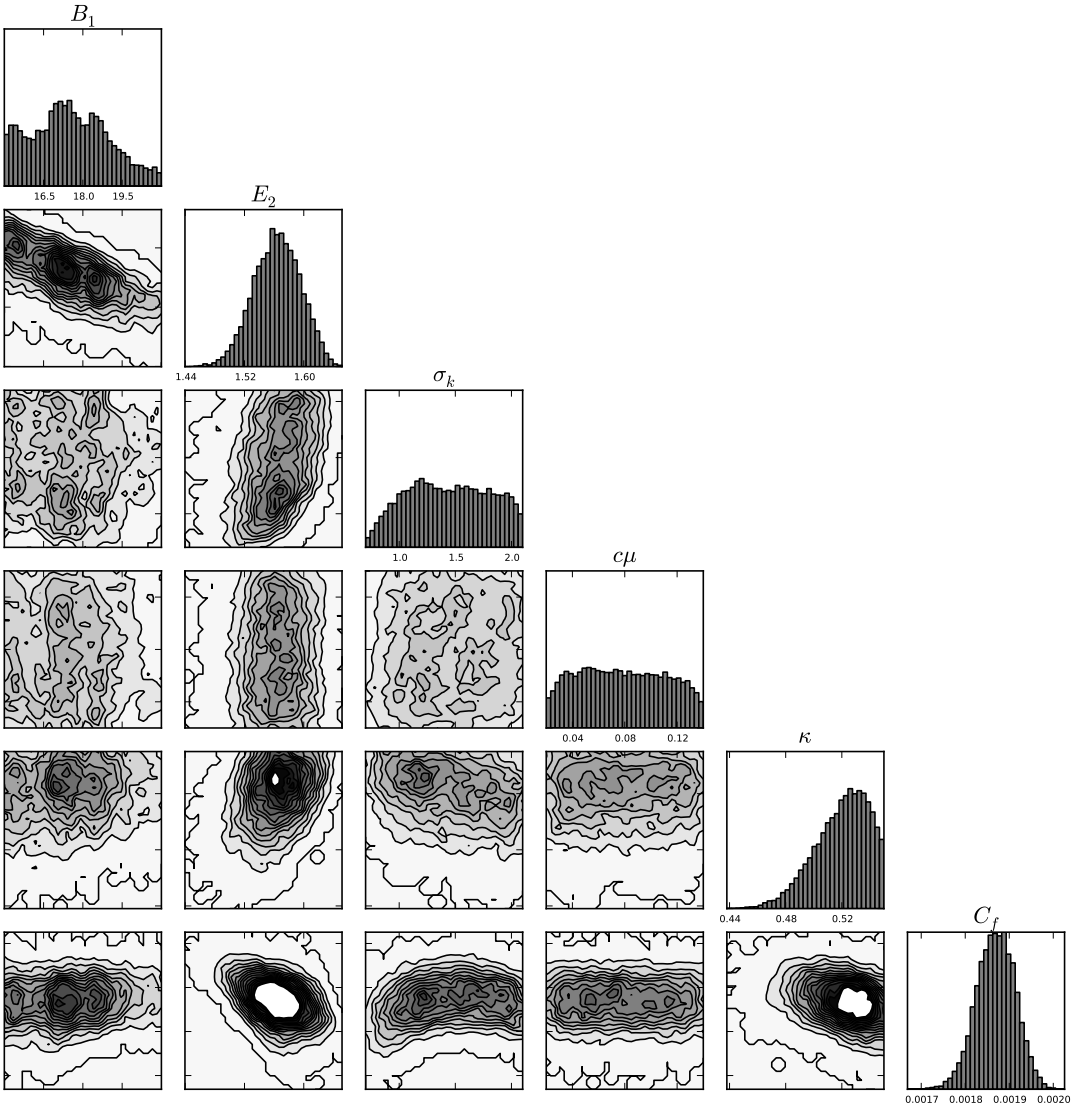

Figure 6.11: Histogram for the KL model apg case after Bayesian calibration.

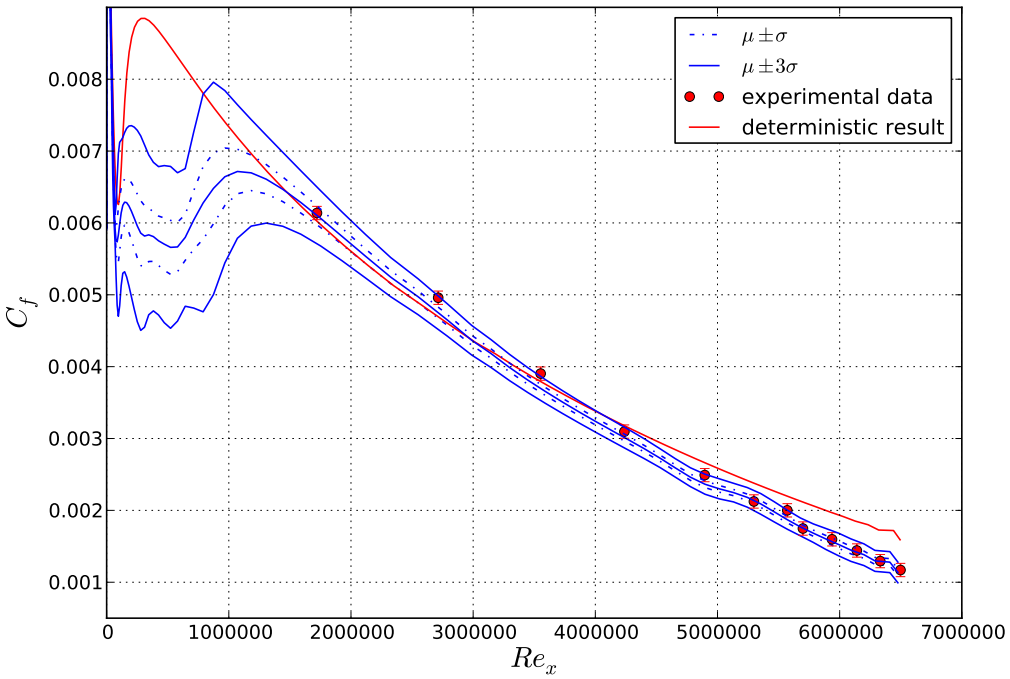

Figure 6.12: Friction coefficient along a flat plate for the KL model apg case after Bayesian calibration.

Chapter 7

Conclusions and Recommendations

The main purpose of the thesis is to investigate whether it is possible to quantify and to reduce the uncertainty of RANS models using the Bayesian inference theorem. More specifically, the Spalart-Allmaras (SA), KL and Launder-Sharma (LS) RANS turbulence models are investigated. A secondary objective is to determine the prior uncertainty by means of the analyst's knowledge of the considered RANS models, rather than merely guestimating a prior uncertainty interval. In addition, a method is developed to create a surrogate model for these models and to verify their correctness.

7.1 The Prior Uncertainty of RANS Turbulence Models

A closure problem results from applying the Reynolds-averaging technique to the Navier-Stokes equations. The model equations that are created (e.g. SA, KL and LS model) to mitigate the closure problem contain coefficients who's values are determined from calibration with experimental values. It is for some of these so-called closure coefficients that a prior uncertainty interval is determined in this thesis. Chapter 3 contains a detailed study on the prior uncertainty intervals for the closure coefficients. Some of the models' closure coefficients can be related to each other, effectively reducing the number of uncertainty parameters. For each model, we finally consider five uncertain parameters. In order to produce a reliable uncertainty interval for these closure coefficients, it is important to know the model inside out. The better knowledge you have about the model, the more reliable your prior uncertainty interval will be. In this thesis, the intervals have been determined by studying how the models are build up, and by comparing the values of the closure coefficients from different sources in literature.

Tables 7.1, 7.2 and 7.3 contain a summary of the prior uncertainty intervals that are determined for the different models. Note that for each model, there are some coefficients that they have in common. For example the Von Kármán coefficient κ is present in each model, and

coefficient C_μ occurs in both the KL and LS model. In this thesis, we have kept the interval the same for each of these coefficients across the three models. It is arguable that this is not necessarily the best approach as they don't directly correspond with a physical quantity. Therefore, as is concluded from the Bayesian calibration, their values can be different for each model.

Table 7.1: Summary of the ranges for the prior uncertainty interval of the SA closure coefficients

Parameter	Lower	Upper
κ	0.3	0.5
σ	0.6	1.0
c_{w2}	0.2	0.5
c_{w3}	1.0	3.0
c_{v1}	4.0	10.0

Table 7.2: Summary of the ranges for the prior uncertainty interval of the $k-\epsilon$ closure coefficients

Parameter	Lower	Upper
n	1.23	1.34
C_μ	0.02	0.14
P/ϵ	1.30	2.90
κ	0.3	0.5
σ_k	0.5	1.5

Table 7.3: Summary of the ranges for the prior uncertainty interval of the $k-l$ closure coefficients

Parameter	Lower	Upper
κ	0.3	0.5
$\sigma_k = \sigma_l$	0.7	2.1
B_1	15.0	21.0
E_2	0.2	2.2
C_μ	0.02	0.14

7.2 The Surrogate Model Creation

The prior uncertainty interval that is determined for the uncertainty parameters needs to be propagated through the models in order to be able to apply Bayesian calibration. To enable this, surrogate models of the actual RANS turbulence models are created. The first step in the process is to estimate a polynomial order for each single uncertain parameter. A reasonable estimate can be obtained by performing deterministic simulations for a varying closure coefficient, while keeping all other parameters constant. The polynomial orders for the uncertainty parameters of each model are summarized in Table 7.2. Note that the same

SA Model	Poly. Order	LS Model	Poly. Order	KL Model	Poly. Order
κ	2	n	2	κ	2
σ	3	C_μ	3	$\sigma_k = \sigma_l$	2
c_{w2}	2	P/ϵ	3	B_1	1
c_{w3}	3	κ	3	E_2	4
c_{v1}	2	σ_k	0	c_μ	1

closure coefficient does not necessarily have the same polynomial order across the different models, proving that its order is definitely model dependent. In case of the Spalart-Allmaras model, the polynomial order has also been determined for the different flow cases. However, results showed that for varying flow cases, the polynomial order did not change. Hence, the polynomial order is not dependent on the flow cases and these results have therefore been disregarded.

When looking at the Figures from which the polynomial orders are determined, i.e. Figure 5.1, 5.2 and 5.3, it becomes apparent that some coefficients are more influential than others. For the three investigated models, two coefficients were always so much more influential than the others, that only they could be calibrated using Bayesian inference. Although not included in the thesis, results have been obtained where the less influential coefficients do get calibrated when the more influential are taken constant. However, this is not of much use, as they are not influential enough on the solution to get a well-calibrated Quantity of Interest. It can

therefore be concluded that only calibrating the most influential uncertainty parameters yield good-enough results for the Quantity of Interest, while dramatically increasing the efficiency of the technique, as much less simulations are required to obtain the surrogate model.

We are able to create surrogate models for all RANS models and every use case. Overall it can be concluded that there is room for improvement when creating these surrogate models. The sometimes large errors when compared to the actual simulation results should be eliminated as much as possible. It is not completely clear whether these large errors are the result of a combination of values for the uncertainty parameters that turn the model unstable. However, as these errors usually occur at the boundaries of the envelope, this is expected to be the main cause. In retrospect, when determining the interval of the prior uncertainty coefficients, it would be good to look at which combinations of closure coefficients yield a model for which convergence can be obtained. This would probably eliminate the large error at the boundaries of the surrogates.

7.3 Results of the Bayesian Uncertainty Quantification

The results of the Bayesian calibration are discussed in detail in Chapter 6. Generally we observe that the prior uncertainty is significantly reduced. Hence, the main objective of this thesis has been achieved. Note that the best results are obtained at places where the density of the experimental data is highest. In addition, when the experimental uncertainty is lower, this also improves the uncertainty of the simulation results. It is therefore very important to be in the possession of good experimental data in order to apply the technique successfully. The availability of good experimental data is something which can definitely be improved.

The Bayesian calibrated results also prove to be much more accurate than the deterministic results obtained using the default closure coefficients. The variance between the different model's results has also reduced as was predicted in Chapter 4.

Finally, when comparing the Bayesian calibrated closure coefficients for the different scenarios, we can conclude that they are both flow case as well as model dependent. Choosing a constant value for these parameters, as is regular practice when using RANS simulations, is therefore a rather inadequate approach.

Bibliography

[1] J.L. Beck and K.V. Yuen. Model selection using response measurements: a Bayesian probabilistic approach. *ASCE Journal of Engineering Mechanics*, 130:192–203, 2004.

[2] S.H. Cheung, T.A. Oliver, E.E. Prudencio, S. Prudhomme, and R.D. Moser. Bayesian uncertainty analysis with applications to turbulence modeling. *Reliability Engineering and System Safety*, 96:1137–1149, 2011.

[3] P. Cinella and A. Lerat. A fully implicit third-order scheme in time and space for compressible turbulent unsteady flow simulations. In *European Congress on Computational Methods in Applied Sciences and Engineering*, 2000. Barcelona, Spain.

[4] A.C. Cullen and H.C. Frey. *Probabilistic Techniques in Exposure Assessment: A handbook for dealing with variability and uncertainty in models and inputs.* Plenum Press, 1999.

[5] Cinnella P. Dwight R.P. Edeling, W.N. and H. Bijl. A one-equation turbulence model for aerodynamic flows. *AIAA Paper*, 1992. (AIAA-92-0439).

[6] M.J. Gander and A.H. Karp. Stable computation of high order Gauss quadrature rules using discretization for measures in radiation transfer. *Journal of Quantitative Spectroscopy Radiative Transfer*, 68:213–223, 2001.

[7] W. Gautschi. Orthogonal polynomials (in Matlab). *Journal of Computational and Applied Mechanics*, 178:215–234, 2005.

[8] R.G. Ghanem. Ingredients for a general purpose stochastic finite elements implementation. *Comp. Meth. Appl. Mech. Engrg.*, 168:19–34, 1999.

[9] R.G. Ghanem and P.D. Spanos. Stochastic Finite Elements: A Spectral Approach, 1991.

[10] G.H. Golub and J.H. Welsch. Calculation of Gauss quadrature rules. *Mathematics of Computation*, 23(106):221–230, 1969.

[11] G.J.A. Loeven. *Efficent Uncertainty Quantification in Computational Fluid Dynamics.* PhD thesis, Delft University of Technology, Faculty of Aerospace Engineering, Chair of Aerodynamics, 2010.

[12] G.J.A. Loeven, J.A.S. Witteveen, and H. Bijl. Probabilistic collocation: an efficient non-intrusive approach for arbitrarily distributed parametric uncertainties. In *Proceedings of*

the 45th AIAA Aerospace Science Meeting and Exhibit, 2007a. AIAA paper 2007-317, Reno(NV), USA.

[13] Witteveen J.A.S. Loeven, G.J.A. and H. Bijl. Efficient uncertainty quantification using a two-step approach with chaos collocation. In *Proceedings of the ECCOMAS CFD Conference*, 2006. Egmond aan Zee, The Netherlands.

[14] M.S. Mohamed and J.C. LaRue. The decay power law in grid-generated turbulence. *Journal of Fluid Mechanics*, 219(1):195–214, 1990.

[15] NACA. Investigations Of The Wall-shearing Stress In Turbulent Boundary Layers. Technical report, National Advisory Committee for Aeronautics, 1950. NACA TM 1285, Washington D.C., USA.

[16] NACA. On The Turbulent Friction Layer For Rising Pressure. Technical report, National Advisory Committee for Aeronautics, 1951. NACA TM 1314, Washington D.C., USA.

[17] W.L. Oberkampf, S.M. DeLand, B.M. Rutherford, et al. Estimation of total uncertainty in modeling and simulation. Technical report, Sandia National Laboratories, 2000. SAND2000-0824.

[18] T. Oden, R. Moser, and O. Ghattas. Computer Predictions with Quantified Uncertainty. Technical report, The Institute for Computational Engineering and Sciences, 2000.

[19] P.D.A. Platteeuw. Application of the Probabilistic Collocation method to uncertainty in turbulence models: Investigation of the k-ϵ model of turbulence. Master's thesis, Delft University of Technology, Faculty of Aerospace Engineering, Chair of Aerodynamics, 2008.

[20] B.R. Smith. The k-kl Turbulence Model and Wall Layer Model for Compressible Flows. *AIAA Paper*, 1990. (AIAA-90-1483).

[21] B.R. Smith. A Near Wall Model for the k-l Two Equation Turbulence Model. *AIAA Paper*, 1994. (AIAA-94-2386).

[22] P.R. Spalart and S.R. Allmaras. A one-equation turbulence model for aerodynamic flows. *AIAA Paper*, 1992. (AIAA-92-0439).

[23] R.W. Walters and L. Huyse. Uncertainty Analysis for Fluid Mechanics with Applications. Technical report, NASA Langley Research Center, 2002. ICASE Report No. 2002-1, Hampton, Virginia USA.

[24] J.A.S. Witteveen and H. Bijl. Modeling arbitrary uncertainties using gram−schmidt polynomial chaos. In *Proceedings of the 44th AIAA Aerospace Science Meeting and Exhibit*, 2006a. AIAA paper 2006-896, Reno(NV), USA.

[25] D. Xiu and G.E. Karniadakis. The Wiener-Askey polynomial chaos for stochastic differential equations. *SIAM J. Sci. Comput.*, 24(2):619–644, 2002.

[26] Durst F. Nagib H. Zanoun, E.-S. Evaluating the law of the wall in two-dimensional fully developed turbulent channel flows. *Physics of Fluids*, 15(10):3079–3089, 2003.

Appendix A

The Galerkin Polynomial Chaos Method

The Galerkin Polynomial Chaos Method is the most general Polynomial Chaos method. Its name originates from the Galerkin projection, which is used to obtain the polynomial chaos coefficients. The general idea of the Galerkin Polynomial Chaos method is to introduce uncertainty into the problem as an additional dimension on which the final solution depends. A fundamental concept of the method is the decomposition of a random function into deterministic and stochastic components. For example, a solution for a velocity field u, depending on a transformed variable $\xi(\theta)$, is approximated by equation (A.1).

$$u\left(\mathbf{x},t,\theta\right) \approx \sum_{i=0}^{M} \bar{u}_i(\mathbf{x},t)\Psi_i\left(\xi(\theta)\right) \tag{A.1}$$

The solution $u\left(\mathbf{x},t,\theta\right)$ is a function of space $\mathbf{x} \in D \subset \mathbb{R}^n$, time t and the random event $\theta \in \Theta$. The probability space is given by $(\Theta, \mathcal{F}, P)$, where Θ is the set of outcomes, $\mathcal{F} \subset 2^{\Theta}$ is the σ-algebra of events, and $P : \mathcal{F} \to [0,1]$ is a probability measure [11].

In equation (A.1), the random variable u is divided into a deterministic part, the coefficients $\bar{u}_i$, and a stochastic part, the polynomial chaoses Ψ_i. Note that a polynomial chaos is a polynomial dependent on random variables instead of ordinary variables. The vector ξ consists out of these random variables $\{\xi_1, ..., \xi_d\}$, which are linear transformations of the d uncertain parameters. Furthermore, these polynomials are orthogonal with respect to the distribution of the input parameters. For standard distributions, corresponding polynomials exist. These can be found in the Askey scheme [25]. For arbitrary distributions, the orthogonal polynomial can be constructed using the Gram-Schmidt algorithm, see Witteveen and Bijl [24]. The expansion consists out of $M+1$ terms, which are determined by the number of random variables, d, and the highest order, p, of the applied set of polynomials, $\{\Psi_i\}$:

$$M + 1 = \frac{(d+p)!}{d!p!} \tag{A.2}$$

Now consider the general stochastic differential equation represented by equation (A.3).

$$\mathcal{L}\left(\mathbf{x},t,\theta;u\left(\mathbf{x},t,\theta\right)\right) = S\left(\mathbf{x},t,\theta\right) \tag{A.3}$$

The differential operator $\mathcal{L}$ contains space and time derivatives and can be stochastic, denoted by θ. The source term S depends on space, time and a random event, just like the solution u. The solution u (A.1), can now be substituted into the differential equation (A.3).

$$\mathcal{L}\left(\mathbf{x}, t, \theta; \sum_{i=0}^{M} \bar{u}_i(\mathbf{x}, t)\Psi_i\left(\xi(\theta)\right)\right) \approx S\left(\mathbf{x}, t, \theta\right) \tag{A.4}$$

Now the Galerkin projection can be applied on each basis polynomial $\{\Psi_k\}$. This is done in order to ensure that the truncation error is orthogonal to the functional space spanned by $\{\Psi_i\}$.

$$\left(\mathcal{L}\left(\mathbf{x}, t, \theta; \sum_{i=0}^{M} \bar{u}_i\Psi_i\right), \Psi_k\right) = (S, \Psi_k) \qquad k = 0, 1, ..., M, \tag{A.5}$$

in which $(\cdot, \cdot)$ represents an inner product, which is defined by equation (A.6).

$$\left(f\left(\xi\right), g\left(\xi\right)\right) = \int f(\xi)g(\xi)w(\xi)\mathrm{d}\xi, \tag{A.6}$$

in which the weighting function $w\left(\xi\right)$ denotes the probability density function of the uncertain parameters. The following orthogonality holds:

$$\left(\Psi_i, \Psi_j\right) = \left(\Psi_i^2\right)\delta_{ij}, \tag{A.7}$$

where δ_{ij} is the Kronecker delta. Finally, the resulting $M + 1$ set of deterministic equations can be solved numerically in order to find the coefficients $\bar{u}_i$. Once these are known, the probability distribution of the solution (A.1) can be constructed. The mean and variance are given by equation (A.8) and (A.9) respectively.

$$\mu_u = \bar{u}_0(\mathbf{x}, t) \tag{A.8}$$

$$\sigma_u^2 = \sum_{1}^{M} \bar{u}_i(\mathbf{x}, t)^2\left(\Psi_i^2\right) \tag{A.9}$$

Typically, a number of 2-5 iterations is required in order to solve for a number of M+1 coefficients $\bar{u}_i$. This results into an order of 2-5 times M+1 deterministic computations, depending on the required accuracy.

Appendix B

The Hermite Polynomials

The Hermite polynomials are an orthogonal polynomial sequence used in probability theory. The equation for the Hermite polynomials can be written as follows:

$$He_n(x) = (-1)^n e^{x^2/2} \frac{d^n}{dx^n} e^{-x^2/2} = \left(x - \frac{d}{dx} \right)^n \cdot 1 \tag{B.1}$$

The first eleven Hermite polynomials are:

$$He_0(x) = 1 \tag{B.2a}$$
$$He_1(x) = x \tag{B.2b}$$
$$He_2(x) = x^2 - 1 \tag{B.2c}$$
$$He_3(x) = x^3 - 3x \tag{B.2d}$$
$$He_4(x) = x^4 - 6x^2 + 3 \tag{B.2e}$$
$$He_5(x) = x^5 - 10x^3 + 15x \tag{B.2f}$$
$$He_6(x) = x^6 - 15x^4 + 45x^2 - 15 \tag{B.2g}$$
$$He_7(x) = x^7 - 21x^5 + 105x^3 - 105x \tag{B.2h}$$
$$He_8(x) = x^8 - 28x^6 + 210x^4 - 420x^2 + 105 \tag{B.2i}$$
$$He_9(x) = x^9 - 36x^7 + 378x^5 - 1260x^3 + 945x \tag{B.2j}$$
$$He_{10}(x) = x^{10} - 45x^8 + 630x^6 - 3150x^4 + 4725x^2 - 945 \tag{B.2k}$$

Appendix C

The Basic Monte-Carlo Method

A simple way to propagate an input distribution through a simulation is by means of a Monte-Carlo method. The procedure of a basic Monte-Carlo method is executed as follows[23]:

1. Sample the (joint-) probability density function for the random variable(s).
2. Calculate the deterministic solution for each sampled input value
3. Determine the statistics of the output distribution from the obtained deterministic solutions, e.g. mean, variance, skewness, ...

The statistics can be obtained from the definition of the expected value, $\mathbb{E}$, of a function $g(\xi)$, in which ξ is a random variable. This definition is mathematically represented by equation (C.1).

$$\mathbb{E}\left[g(\xi)\right] = \int g(\xi)p(\xi)\mathrm{d}\xi, \tag{C.1}$$

in which $p(\xi)$ is the probability density function of variable ξ. The mean of the probability density function, also called the *first moment about the origin* is defined by equation (C.2).

$$\bar{\xi} = \mathbb{E}\left[\xi\right] = \int \xi p(\xi)\mathrm{d}\xi, \tag{C.2}$$

The r^{th} moment about the mean is given by equation (C.3).

$$\mathbb{E}\left[(\xi - \bar{\xi})^r\right] = \int (\xi - \bar{\xi})^r p(\xi)\mathrm{d}\xi, \tag{C.3}$$

For numerical applications, the integrals represented by equation (C.3) are replaced by discrete sums. The variance, skewness and kurtosis are respectively related to the 2^{nd}, 3^{rd} and 4^{th} moment about the mean. Finally, the distribution of the data can be derived from these statistics.

Theoretically, the Monte-Carlo method converges to the exact solution as the number of samples $N \to \infty$. However, the convergence of the method is slow, typically of the order $O\left(N^{-1/2}\right)$. Generally, the Monte-Carlo method is too expensive in terms of time and computing power when complex simulations are considered.

Appendix D

Experimental Turbulent Flat Plate Flow

This Appendix contains copies of experiments performed by Wieghardt [16] and Ludwieg & Tillman [15]. These experiments are used as reference cases in this thesis.

D.1 Wieghardt's zero pressure gradient case

IDENTIFICATION: 1400

DESCRIPTION: Equilibrium boundary layer at constant pressure; 23 profiles

STATUS: MANDATORY RUN with match at fourth profile

REFERENCE: Wieghardt, K. and Tillmann, W., U & M 6617 (1944), translated as "On the Turbulent Friction Layer for Rising Pressure," NACA TM 1314 (1951). The data were first reported in U & M 6603 (1943), and are also cited in U & M 6612 (1944) and U & M 6627 (1945). The wind tunnel as modified for these experiments is described in AVA Monograph MAP-VG-246T, Sect. D_1 II 3.3 (1947). The probe rake is described in Techn. Ber. 11, 7, p. 207 (1944). The mean-velocity profiles were provided in tabulated form by W. Tillmann.

EDITORS' COMMENTS: These measurements have been chosen as typical of the standard flat-plate boundary layer, with certain reservations. The model was a waxed-plywood plate with a slightly undulating surface; the tripping device was a blunt leading edge fitted with a small trip wire. The first profile is probably at about the minimum Reynolds number for turbulent flow. The tunnel turbulence level was about 0.25 percent. An average value of 0.151 cm^2/sec has been used for ν. Note that the data were obtained using a rake rather than a single probe. This technique fixes the relative position of the data points, and also avoids some effects of drift in tunnel conditions by speeding up the data-taking process. However, the profiles may be subject to more wall interference than usual. Moreover, the profiles are defined by a relatively small number of points, none of which lie in the sublayer. Consequently, computed values for the integral parameters (especially for the first few stations) are strongly affected by the choice of interpolation scheme for the integration.

ORIGINATORS' COMMENTS:

WIEGHARDT FLAT PLATE FLOW U = 33 MPS IDENT = 1400 V = 0.151000

X	UI	DUI	THETA	H	HS	G	CF	CFLT	CFE	BETA
0.087	33.10	0.0	0.021	2.102	1.836	10.148	0.00534	0.00179	0.0	-0.0
0.187	32.80	0.0	0.049	1.642	1.803	8.491	0.00424	0.00292	0.0	-0.0
0.287	33.00	0.0	0.071	1.543	1.793	8.012	0.00386	0.00308	0.0	-0.0
0.387	32.80	0.0	0.092	1.503	1.783	7.838	0.00364	0.00307	0.0	-0.0
0.487	33.00	0.0	0.110	1.469	1.784	7.692	0.00345	0.00308	0.0	-0.0
0.637	33.00	0.0	0.131	1.438	1.786	7.414	0.00337	0.00309	0.0	-0.0
0.787	33.00	0.0	0.157	1.428	1.779	7.523	0.00317	0.00299	0.0	-0.0
0.937	32.90	0.0	0.177	1.401	1.787	7.186	0.00317	0.00302	0.0	-0.0
1.087	33.00	0.0	0.201	1.397	1.783	7.235	0.00308	0.00294	0.0	-0.0
1.237	33.00	0.0	0.222	1.390	1.782	7.236	0.00301	0.00289	0.0	-0.0
1.437	32.90	0.0	0.251	1.382	1.781	7.211	0.00293	0.00283	0.0	-0.0
1.687	32.90	0.0	0.286	1.377	1.780	7.266	0.00284	0.00276	0.0	-0.0
1.987	33.00	0.0	0.328	1.365	1.782	7.175	0.00278	0.00270	0.0	-0.0
2.287	33.00	0.0	0.374	1.358	1.782	7.189	0.00269	0.00264	0.0	-0.0
2.587	32.90	0.0	0.408	1.345	1.786	7.039	0.00266	0.00263	0.0	-0.0
2.887	33.00	0.0	0.449	1.340	1.787	7.035	0.00260	0.00259	0.0	-0.0
3.187	33.00	0.0	0.486	1.333	1.789	6.932	0.00260	0.00256	0.0	-0.0
3.487	33.00	0.0	0.525	1.331	1.789	6.954	0.00256	0.00252	0.0	-0.0
3.787	33.00	0.0	0.559	1.330	1.788	6.971	0.00253	0.00248	0.0	-0.0
4.087	33.00	0.0	0.597	1.334	1.787	7.130	0.00247	0.00242	0.0	-0.0
4.387	33.00	0.0	0.642	1.321	1.790	6.917	0.00247	0.00242	0.0	-0.0
4.687	33.10	0.0	0.671	1.314	1.794	6.819	0.00246	0.00242	0.0	-0.0
4.987	33.00	0.0	0.710	1.314	1.793	6.856	0.00243	0.00238	0.0	-0.0

D.2 Ludwieg & Tillman's favourable pressure gradient case

TITLE: Ludwieg and Tillmann, accelerating flow
IDENTIFICATION: 1300
DESCRIPTION: Near-equilibrium boundary layer in moderate negative pressure gradient; 12 profiles
STATUS: MANDATORY RUN with match at second profile
REFERENCE: Ludwieg, H. and Tillmann, W., Ing.-Arch. 17, p. 288-299 (1949); translated as "Investigations of the Wall Shearing Stress in Turbulent Boundary Layers," NACA TM 1285 (1950). Tabulated mean-velocity profiles were supplied by W. Tillmann.
EDITORS' COMMENTS: These are the experiments with a heated element which originally suggested the idea of a universal law of the wall. Apparently by accident, this flow with falling pressure seems to be quite close to equilibrium, at least up to $x = 3.5$ meters. The profiles were measured with a rake rather than with a single probe (for references and other remarks see Wieghardt's flow at constant pressure, run 1400). The free-stream velocity is known only at the profile stations. The profile at $x = 3.732$ meters seems to be distorted, and a slight raggedness in the other profiles combined with lack of detail near the wall makes the integral parameters somewhat unreliable. An average value of 0.154 cm^2/sec has been used for ν.
ORIGINATORS' COMMENTS:
FLOW PARAMETERS ACCORDING TO ORIGINATORS: For u_∞ and c_f by heated-element technique, see p. 1300-3.

x meters	ν cm^2/sec	x meters	ν cm^2/sec
0.782	0.1545	3.532	0.1550
1.282	0.1525	3.732	0.1555
1.782	0.1551	3.932	0.1535
2.282	0.1530	4.132	0.1540
2.782	0.1540	4.332	0.1553
3.132	0.1545		
3.332	0.1539		

LUDWIEG ANC TILLMANN ACCELERATING FLOW — IDENT = 1300 — V = 0.154000

X	UI	DUI	THETA	H	HS	G	CF	CFLT	CFE	BETA
0.782	11.52	3.650	0.135	1.426	1.798	6.219	0.00461	0.00416	0.00454	-0.264
1.282	13.38	4.000	0.149	1.376	1.815	5.820	0.00440	0.00421	0.00434	-0.278
1.782	15.61	4.330	0.158	1.371	1.812	5.940	0.00415	0.00400	0.00415	-0.290
2.282	17.85	4.680	0.173	1.360	1.815	5.932	0.00398	0.00384	0.00396	-0.310
2.782	20.20	4.900	0.189	1.368	1.806	6.214	0.00375	0.00358	0.00365	-0.334
3.132	22.07	5.000	0.196	1.363	1.806	6.255	0.00362	0.00349	0.00356	-0.334
3.332	22.90	5.000	0.196	1.355	1.810	6.156	0.00362	0.00350	0.00347	-0.320
3.532	23.70	4.960	0.203	1.347	1.812	6.106	0.00356	0.00348	0.00342	-0.321
3.732	25.13	4.860	0.196	1.336	1.819	5.907	0.00362	0.00351	0.00348	-0.280
3.932	25.80	4.600	0.219	1.353	1.806	6.352	0.00338	0.00330	0.00336	-0.313
4.132	26.40	4.130	0.227	1.346	1.808	6.281	0.00335	0.00328	0.00330	-0.285
4.332	27.50	3.500	0.227	1.341	1.811	6.191	0.00338	0.00327	0.00320	-0.230

D.3 Ludwieg & Tillman's adverse pressure gradient case

TITLE: Ludwieg and Tillmann, mild adverse pressure gradient

IDENTIFICATION: 1100

DESCRIPTION: Boundary layer in diverging channel; 12 profiles

STATUS: MANDATORY RUN with match at second profile

REFERENCE: Ludwieg, H. and Tillmann, W., Ing.-Arch. 17, p. 288-299 (1949); translated as "Investigations of the Wall Shearing Stress in Turbulent Boundary Layers," NACA TM 1285 (1950). Tabulated mean-velocity profiles were supplied by W. Tillmann.

EDITORS' COMMENTS: These are the experiments with a heated element which originally suggested the idea of a universal law of the wall. The profiles were measured with a rake rather than with a single probe (for references and other remarks see Wieghardt's flow at constant pressure, run 1400). The free-stream velocity is known only at the profile stations, so that the streamwise pressure gradient is uncertain near the first and last stations. An average value of 0.155 cm^2/sec has been used for ν.

ORIGINATORS' COMMENTS:

FLOW PARAMETERS ACCORDING TO ORIGINATORS: For u_∞ and c_f by heated-element technique, see p. 1100-3.

x meters	ν cm^2/sec
0.782	0.1537
1.282	0.1555
1.782	0.1545
2.282	0.1559
2.782	0.1546
3.132	0.1530
3.332	0.1555
3.532	0.1525
3.732	0.1542
3.932	0.1559
4.132	0.1565
4.332	0.1563

LUDWIEG AND TILLMANN MILD ADVERSE PRESSURE GRADIENT IDENT = 1100 V = 0.155000

X	UI	DUI	THETA	H	HS	G	CF	CFLT	CFF	BETA
0.782	33.90	-2.300	0.276	1.381	1.778	7.307	0.00285	0.00276	0.00271	0.181
1.282	32.60	-3.350	0.413	1.394	1.760	8.014	0.00249	0.00246	0.00249	0.475
1.782	30.70	-4.320	0.606	1.402	1.753	8.633	0.00221	0.00222	0.00218	1.083
2.282	28.60	-3.580	0.811	1.427	1.734	9.353	0.00205	0.00202	0.00202	1.415
2.782	27.10	-3.000	1.074	1.457	1.720	10.445	0.00190	0.00181	0.00186	1.919
3.132	26.05	-2.740	1.276	1.485	1.706	11.280	0.00168	0.00167	0.00171	2.379
3.332	25.75	-2.600	1.432	1.492	1.703	11.607	0.00162	0.00161	0.00160	2.672
3.532	24.85	-2.500	1.614	1.519	1.693	12.461	0.00150	0.00151	0.00153	3.282
3.732	24.50	-2.400	1.773	1.542	1.684	13.253	0.00141	0.00142	0.00152	3.806
3.932	24.05	-2.300	2.005	1.566	1.675	14.037	0.00133	0.00133	0.00134	4.530
4.132	23.60	-2.250	2.246	1.594	1.664	14.960	0.00124	0.00124	0.00126	5.499
4.332	23.10	-2.180	2.528	1.618	1.656	15.811	0.00117	0.00117	0.00117	6.615

Appendix E

Time and Spatial Discretisation Methods

This Appendix gives a short explanation about the space and time discretisations which are used in the computational model. The first section describes the third-order spatial discretisation method. Section E.2 discusses the time integration and dual-time stepping technique.

E.1 Third-order Spatial Discretisation

The centred, third-order accurate scheme used in the RANS solver is constructed by correcting the second-order dispersive error resulting from the spatial discretisation of the classical Jameson scheme for the Euler equations[3]. A third-order scheme for the classical one-dimensional Euler equation is given by:

$$w_t + f_x(w) = 0 \tag{E.1}$$

For a regular mesh, in which $x_j = j\delta x$, the classical centred approximation of equation (E.1) can be written as:

$$w_t|_j + \frac{1}{\delta x}\delta\mu f|_j = 0, \tag{E.2}$$

where $(\delta\phi)_{j+\frac{1}{2}} = \phi_{j+1} - \phi_j$ and $(\mu\phi)_{j+\frac{1}{2}} = \frac{1}{2}(\phi_{j+1} + \phi_j)$.

Equation (E.2) is a fourth-order approximation to:

$$w_t + f(w)_x + \frac{\delta x^2}{6} f(w)_{xxx} = 0, \tag{E.3}$$

in which the additional last term represents a dispersive error. When this term is cancelled, we are left with a fourth-order accurate non-dissipative approximation. In order to avoid

numerical oscillations, numerical dissipation is introduced into the spatial approximation. This is done by adding the Jameson's artificial dissipation $\mathcal{D}$ to the scheme.

$$\begin{aligned}
\mathcal{D}w &= \frac{1}{\delta x}\left[\delta(\epsilon_2\rho(\bar{A})\delta w)\right] - \frac{1}{\delta x}\left[\delta(\epsilon_4\rho(\bar{A})\delta^3 w)\right], \\
\epsilon_2|_{j+\frac{1}{2}} &= k_2 \max\left\{\nu_j, \nu_{j+1}\right\}, \\
\epsilon_4|_{j+\frac{1}{2}} &= \max\left\{0, k_4 - \epsilon_2|_{j+\frac{1}{2}}\right\}, \\
\nu_j &= \left|\frac{p_{j+1} - 2p_j + p_{j-1}}{p_{j+1} + 2p_j + p_{j-1}}\right|,
\end{aligned} \tag{E.4}$$

in which A is the flux Jacobian, ρ represents the spectral radius of a matrix, p is the fluid pressure and $k1$, k_4 are constant parameters. Finally, the scheme for the one-dimensional Euler equations becomes:

$$w_t|_j + \mathcal{L}w|_j = \mathcal{D}w|_j, \tag{E.5}$$

with

$$\mathcal{L}w = \frac{1}{\delta x}\delta(\mu f - \frac{1}{6}\delta^2\mu f). \tag{E.6}$$

For a region where w is smooth, $\epsilon_2 = O(\delta x^2)$ and $\epsilon_4 = O(1)$. Hence, $\mathcal{D}w = O(\delta x^3)$ and scheme (E.4), (E.5) and (E.6) are third-order accurate. Using a classical second-order discretisation for the viscous terms, the numerical method has been extended to the Navier-Stokes equations.

E.2 Time Integration and the Dual Time Stepping Technique

For steady problems, a time-stepping technique base on a classical four stage Runge-Kutta method with implicit residual smoothing is applied. The Runge-Kutta scheme reads:

$$\begin{cases}
w^{(0)} & = w^n, \\
\mathcal{J}(w^{(k)} - w^{(0)}) & = -a_k\Delta t(\mathcal{L} - \mathcal{D})w^{(k-1)}, \qquad k = 1, ..., 4, \\
w^{n+1} & = w^{(4)},
\end{cases} \tag{E.7}$$

where w^n is the numerical solution at time $n\Delta t$, $\mathcal{L}$ denotes the approximation of the spatial derivatives, $\mathcal{D}$ the numerical viscosity and $a_1 = 1/4$, $a_2 = 1/3$, $a_3 = 1/2$ and $a_4 = 1$[3]. The implicit operator $\mathcal{J}$ for a one-dimensional problem, taking into account the contribution of the Euler and viscous terms, is given by equation (E.8).

$$\mathcal{J} = 1 - \beta^e\left(\frac{\Delta t}{\delta x}\right)^2\delta(\lambda^{e2}\delta) - \beta^v\frac{\Delta t}{\delta x^2}\delta(\lambda^v\delta), \tag{E.8}$$

in which λ^e and λ^v are respectively the spectral radii of the convective and diffusive terms, and β^e and β^v are tunable parameters. When the Runge-Kutta method given by (E.7) is

coupled to the third-order approximation given by (E.6) and numerical dissipation is assumed zero ($\mathcal{D} = 0$), then (E.7) is unconditionally stable for

$$\beta^e \geq \frac{1}{8}.$$

In case of a pure diffusion problem, the Runge-Kutta scheme (E.7) coupled to a second-order centred discretisation of the viscous terms is unconditionally stable when

$$\beta^v \geq \frac{2}{\Omega^v} \quad \text{with } \Omega^v \approx 2.785.$$

Note that the second term of equation (E.8) is of the order $O(\Delta t^2)$, while the viscous term is of the order $O(\Delta t)$. Hence, for time-dependent Navier-Stokes calculations, second-order time accuracy can be obtained by neglecting the viscous distribution, i.e. $\beta^v = 0$. However, as a result the unconditional stability will be lost. In practice, CFL numbers of about 100 can be used in the wall region[3].

Appendix F

The Turbulent Boundary Layer

When simulating turbulent flows, we are usually interested in the ones which are bounded by walls. Therefore, most closure models have been developed with this fact in mind. This section discusses how, after Reynolds-averaging the Navier-Stokes equations, wall-bounded flows can be divided into several regions.

Wall-bounded turbulent flows are characterized by a boundary layer structure which can be divided into several layers. A first distinction is made between the inner layer, the overlap region and the outer layer. A second division is made within the inner layer, between the viscous sublayer and the buffer layer. As its name suggests, the viscous sublayer is dominated by viscous effects. Within the buffer layer, both viscous and Reynolds stresses are significant. The overlap region is dominated by inviscid turbulent phenomena, i.e. viscous stress becomes negligible. Finally, the outer layer's behaviour depends on the type of boundary layer examined. When dealing with an external boundary layer, the outer layer is a region with high intermittency, while for internal flow, they have more regular perturbations.

Each of the regions is described by a set of scaling parameters. For the inner region these are the friction velocity, u_τ, and viscosity, ν.

$$u_\tau = \sqrt{\frac{\tau_w}{\rho}}, \tag{F.1}$$

in which τ_w is the average wall shear stress. The average velocity profile for the inner region is defined by equation (F.2). This relation is referred to as the law of the wall.

$$\frac{U}{u_\tau} = f\left(\frac{y u_\tau}{\nu}\right) \qquad \text{for} \qquad \frac{y}{\delta} \ll 1, \tag{F.2}$$

in which y represents the distance to the wall, and δ is the characteristic length of the problem (e.g. boundary layer thickness).

The outer layer is characterized by the friction velocity, u_τ, and the characteristic length of the problem, δ. Its average velocity profile is described by the so-called defect law, which is

given by equation (F.3).

$$\frac{U - U_\infty}{u_\tau} = F\left(\frac{y}{\delta}\right) \qquad \text{for} \qquad \frac{y u_\tau}{\nu} \gg 1, \tag{F.3}$$

in which U_{inf} is a characteristic velocity of the problem, such as the free-stream velocity.

Within the overlap region, equations (F.2) and (F.3) are expected to match. This result into the log-law of the wall, represented by equation (F.4).

$$u^+ = \frac{1}{\kappa} \ln\left(y^+\right) + C, \tag{F.4}$$

where $u^+ \equiv U/u_\tau$ and $y^+ \equiv y u_\tau/\nu$. Furthermore, as the viscous sublayer is completely dominated by viscous forces, and velocity fluctuations are negligible, equation (F.2) reduces to $u^+ = y^+$ for $y^+ \lesssim 5$. In Table F.1 the ranges and average velocity profiles related to these different layers are summarized.

Table F.1: Summary of the average velocity profiles for wall-bounded flows

Layers	Range	Average velocity profile
Inner layer: Viscous sublayer	$y^+ \lesssim 5$	$u^+ = y^+$
Inner layer: Buffer layer	$5 \lesssim y^+ \lesssim 40$	$u^+ = f\left(y^+\right)$
Overlap region	$y^+ \gtrsim 40$ and $y/\delta \lesssim 0.2$	$u^+ = \frac{1}{\kappa} \ln\left(y^+\right) + C$
Outer layer	$y/\delta \gtrsim 0.2$	$\frac{U - U_\infty}{u_\tau} = F\left(y/\delta\right)$